TECHNISCHE UNIVERSITÄT WIEN

DISSERTATION

Preparation of anions as a coolant for antimatter gravity experiments

Ausgeführt zum Zwecke der Erlangung des akademischen Grades eines
Doktors der technischen Wissenschaften unter Leitung von

Priv.-Doz. Dr. Johann Marton
Stefan-Meyer-Institut für subatomare Physik
Österreichsiche Akademie der Wissenschaften
E141 Atominstitut der Technischen Universität Wien

Eingereicht an der Technischen Universität Wien
am Atominstitut

von

Alexander Hinterberger
Matrikelnummer: e00525954
Adresse: Brunellengasse 17, 1220 Wien, Österreich

Wien, am:

Die Dissertation wurde begutachtet von:
Dr. Kai-Thomas Brinkmann   Dr. Peter Krizan

1

Abstracts

German

Diese Thesis fokusiert sich auf einige Schritte die für das Durchführen einer Gravitationsmessung mit einem gepulsten Antiwasserstoffstrahl [10] notwendig sind. Im Besonderen konzentriert Sie sich dabei auf die Schaffung eines magnetfeldfreien Bereichs in dem mit Hilfe eines Interferometers eine Gravitationsmessung durchgeführt werden kann. Darüberhinaus beinhaltet die Arbeit den Aufbau eines Apparats zur Demonstration einer Laserkühlung für C_2^- das genutzt werden soll um Antiprotonen zu kühlen.

Nach der Einleitung, der Motivation und den Zielen dieser Thesis werden in Kapitel Drei die Messungen und Simulationen eines supraleitenden Rohres beschrieben das Magnetfelder reflektiert und daher in seinem Inneren die Gravitationsmessung von Antiwasserstoff möglich machen würde. Dieses Kapitel beinhaltet eine Publikation, die im Rahmen dieser Arbeit verfasst wurde, über die supraleitenden Eigenschaften von Blei und Niob und den Einfluss der Geometrie von verschiedenen Rohrgrößen. Darüberhinaus behandelt die Publikation auch das Reflektieren und das Einfangen von Magnetfeldern durch Supraleiter sowie, wie das vermieden werden kann.

Kapitel Vier beinhaltet den Hauptteil dieser Arbeit, den Borealis Apparat, jedoch ohne den Laser Aufbau. Bei dem Apparat liegt der Fokus auf den, im Rahmen dieser Arbeit erstellten Bauteilen, mit denen die Arbeit von Julian Fesel[14] fortgeführt wird. Dazu gehört ein Quadrupol Beam Bender, eine Abbremsstufe und das Design, der Bau und die Komissionierung einer digitalen linearen Paul Falle, inklusive der notwendigen Elektronik und Software.

Kapitel fünf beinhaltet die Simulationen und Messungen die notwendig waren um die Paul Falle und die Abbremsstufe komplett zu Charakterisieren und um eventuelle Schwächen zu erkennen. Dazu gehört das komplette Vermessen des a-q-Parameter-Raums [1] und auch ein Massenspektrum um die Existenz von C_2^- in der Paulfalle nachzuweisen. Eine Publikation über den Borealis Aufbau mit Fokus auf der Paulfalle wurde ebenfalls veröffentlicht [18].

Kapitel sechs behandelt den Bau einer Penningfalle die ursprünglich statt der Paulfalle verwendet werden sollte um C_2^- zu fangen. Die Penning Falle hat zwei Möglichkeiten eines radialen Laserzuganges und einen Axialen. Zusätzlich ist die Falle teilweise kryogen um ein Vorkühlen mit Elektronen zu ermöglichen und um ein besseres Vakuum zu schaffen. Der Permanentmagnet für die Penningfalle ist jedoch immer noch im Bau und es ist unklar ob er homogen genug wird um eine Laserkühlung zu ermöglichen wenn er fertig ist. Eine zweite Variante der Penningfalle die nur geringen Umbau benötigt und mit einem ungenaueren Magneten zurecht kommen würde, wurde konstruiert um

Antiprotonen in einer transportablen Falle zu fangen.

Zuletzt wird die Zusammenfassung und die Aussicht in Kapitel sieben behandelt, sowie die Schritte die als nächstes unternommen werden sollten um das Borealisexperiment seinem Ziel, einer Laserkühlung von C_2^-, näher zu bringen.

English

This thesis focuses on several steps that are necessary to reach the final goal of performing a gravity measurement on a pulsed antihydrogen beam as described in [10]. Specifically this thesis covers the creation of a field free area where an interferometer could perform an accurate gravity measurement, as well as several steps that were made towards an apparatus to demonstrate the production of laser cooled C_2^- for the sympathetic cooling of antiprotons. After the introduction, the motivation for this thesis and the specific goals, chapter three describes the simulations and measurements that were made on superconducting lead and niobium tubes to find specifications for a superconducting shield that could repel the strong magnetic fields of the AEGIS Penning traps to create a field free area where the gravity measurement could be performed with a moiré deflectometer. The chapter contains a publication [17] that contains both the different behavior of lead and niobium as a material and the influence of the tubes geometry. Further it discusses not only the deflection of the magnetic field but also the effect of a field trapping and the streamlining of the magnetic field lines.

Chapter four contains the main topic of this thesis, the Borealis setup that was designed to demonstrate the laser cooling of C_2^-. The chapter includes the complete Borealis experiment, except for the Laser setup but focuses on the extensions that were made on [14]. The extensions are a quadrupole beam bender, a deceleration stage and the design, construction and commissioning of a digital linear Paul trap, including electronics and the used software.

Chapter five includes all measurements and simulations that were made with the Paul trap and the deceleration stage to find weaknesses. This includes a complete characterization of the a-q-parameter space of the Paul trap [1], and a mass spectrum that was made for all masses that are expected to be in the Paul trap. A publication containing said characterizations has been published [18].

Chapter six contains the design and build of a Penning trap that was designed to be used for laser cooling before the idea of a Paul trap was deemed more useful. At first the Borealis Penning trap was designed that would work under partially cryogenic conditions and has two radial accesses for laser cooling and one axial access. However the designed permanent magnet for the penning trap is still not fabricated to this date. Further a second variant of the Penning trap was designed that should be able to trap antiprotons from the AD and is portable. This design would require the same permanent magnet, but would work with lower homogeneities.

Finally chapter seven contains the conclusion and the outlook of this thesis that summarizes the thesis and the steps that should be done in the near

future to complete the Borealis experiment.

Contents

Chapter 1

Introduction and motivation

When the Big Bang created the universe 13.8 billion years ago, an equal amount of matter and antimatter should have been created via pair production in the process[7]. However neither on earth nor in space, significant amounts of antimatter have been discovered yet so there has to be some kind of imbalance between them. This imbalance is of significant interest for several fields of research, including the standard model, where CERN, one of the largest particle research centers in the world, plays a leading role.

The CERN facilities not only house the famous LHC[12] but is also the host of several smaller experiments and among them several antimatter experiments. These experiments share the common goal of discovering the origins of the imbalance between matter and antimatter in the universe. To find possible reasons for the imbalance one has to look for asymmetries in the laws of nature, like the already discovered Parity and Charge-Parity violation. However these already known asymmetries do not explain the lack of antimatter in the universe. So there has to be a further asymmetry in the laws of nature. The Charge-Parity-Time-theorem predicts that a particle and its antiparticle have the same mass and lifetime but an inverse charge and magnetic moment of the same absolute value. So to test the CPT-theorem it is necessary to measure all these values with the highest possible precision to find discrepancies, which is the goal of the antimatter experiments at CERN. The antimatter for said experiments is produced by the Antiproton-Decelerator (AD) in the Antimatter Factory. The production of antimatter begins in the Proton Synchrotron (PS), a pre-accelerator at CERN that directs a proton beam of 26 GeV on an iridium target near the AD area. Here antiprotons are produced via pair production:

$$p_{26GeV} + p_{Iridium} \rightarrow p + p + p + \bar{p}$$
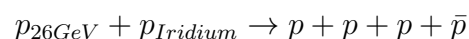
The emerging antiprotons have an energy of 3.57 GeV when they enter the

CERN's Accelerator Complex
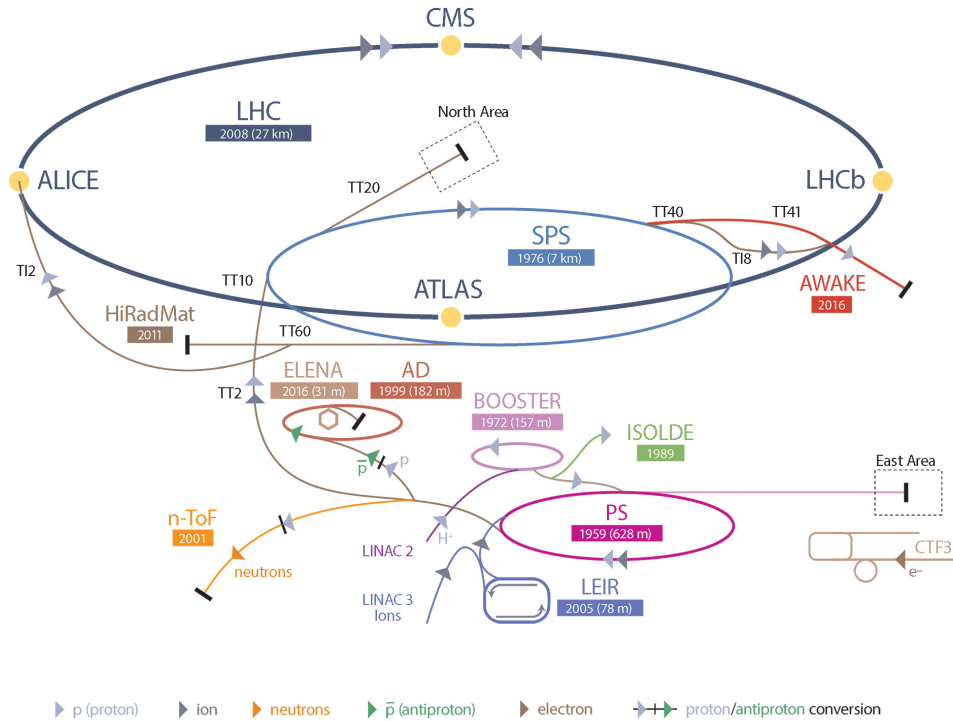
Figure 1.1: The CERN accelerator facility is host to various experiments and among them the Antimatter-Factory (AF) with the Antimatter-Decelerator (AD) in the middle of the picture. In the picture one can see that the different accelerators are connected to each other and can increase the kinetic energy of the particles step-wise as each accelerator adds an amount of energy to the accelerated particles.

AD. Over several cycles of stochastic cooling and electron cooling the energy of the antiprotons in the AD is reduced to $5.3\,\text{MeV}$. This process takes around $100\,\text{s}$ and provides the active experiment with around 3×10^7 antiprotons. Degrader foils made of aluminium further reduce the kinetic energy to under $10\,\text{keV}$ but also decrease the number of antiprotons to around 3×10^5. Now the antiprotons are trapped in penning traps by the experiments for further research. Several experiments at the AD have already delivered interesting results in the field of antimatter. For example the first formation of low-energy antihydrogen was done by the Athena [2] and the Atrap[15] collaboration. A further interesting topic is research on the weak equivalence principle (WEP). The WEP depicts that inertial and gravitational mass are
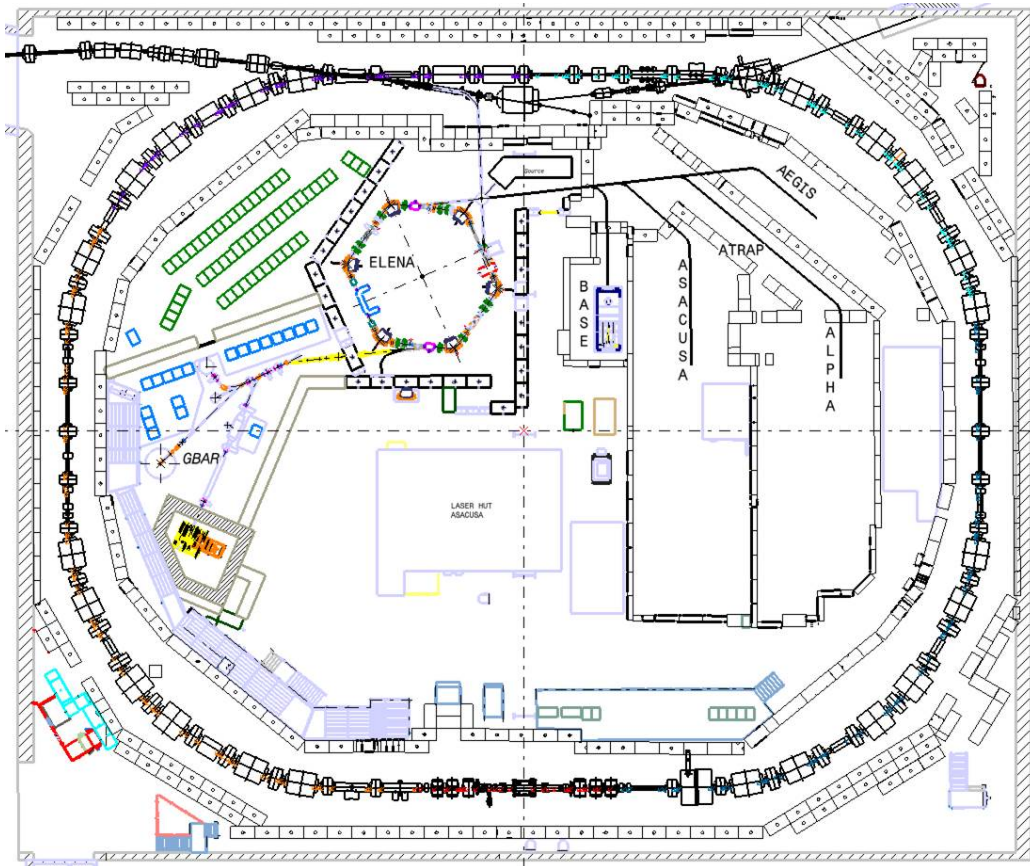
Figure 1.2: The Antimatter Factory: The Antiproton-Decelerator, here shown as black ring that encloses the experiments gets the antiprotons from the iridium target in the upper left corner of the picture. Over several cycles with electron- and stochastic cooling the energy of the antiprotons is reduced from 3.57 GeV to 5.3 MeV and the antiproton bunches are then sent to the experiments, where they are further decelerated by aluminium degrader foils to under 10 keV. The Aegis experiment, where this thesis was written is in the upper right corner of the picture

equal. Neutral antihydrogen would allow a direct gravity measurement to observe, if the gravitational acceleration of antimatter is the same as of matter. At CERN three experiments are currently working on this topic: The Aegis[10] experiment, the G-Bar[24] experiment and the Alpha experiment with its new Alpha-g[5] apparatus. As gravitation is the weakest of all forces these high precision gravity measurements require very cold Antihydrogen and a highly background free environment. So far the so called Three Body Recombination or mixing seems to be the most effective way to form cold

antihydrogen:

$$\bar{p} + e^+ + e^+ = \bar{H} + e^+$$

The antiprotons and positrons are brought in close distance to each other and the antihydrogen is formed by three body collisions. The excess energy of the bound state is carried away by the additional positron. This process was also used for the first antihydrogen formation[2]. The Aegis experiment however uses a process called resonant charge exchange[25] where laser excited Rydberg positrionium is brought into contact with antiprotons:

$$Ps^* + \bar{p} = \bar{H}^* + e^-$$
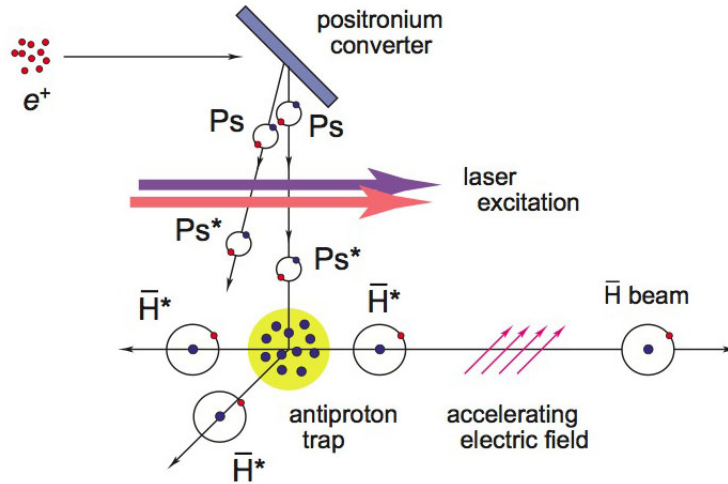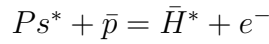
Figure 1.3: Resonant charge exchange at the Aegis experiment: Positrons from a ^{22}Na source hit the positronium converter and form positronium. The positronium is excited by lasers while it drifts towards the antiprotons. In the antiproton trap (Yellow circle) the antihydrogen is created. The produced antihydrogen is then accelerated to the right via AC-Stark forces to be detected by a moiré deflectometer [11].

Here the excess energy of the bound state is carried away by the electron. The advantage of resonant charge exchange over three body recombination is that that plasma manipulation of oppositely charged plasmas is of no concern. Further in resonant charge exchange the temperature of the produced antihydrogen is determined mostly by the temperature of the used antiprotons. So the antiprotons could be cooled before the antihydrogen is formed

11
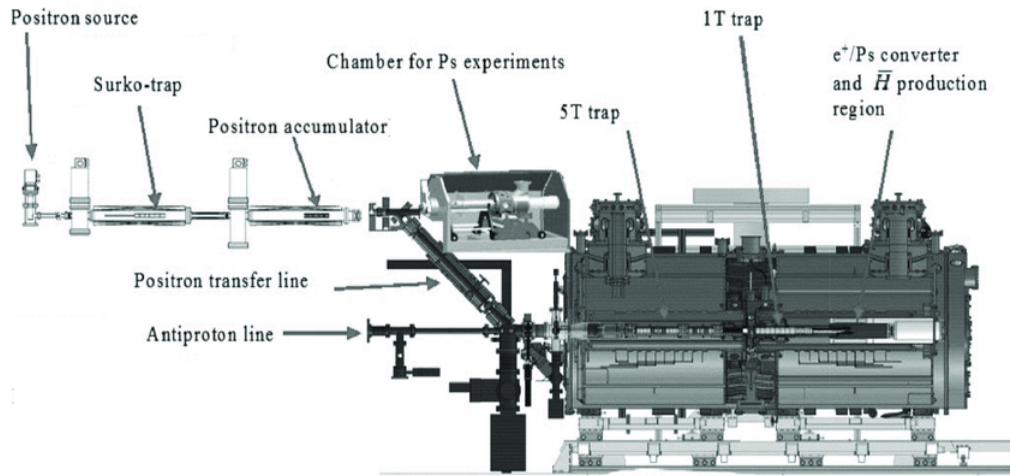
Figure 1.4: The complete Aegis Experiment at this state of development. The antiprotons come from the antiproton line, are trapped and electron cooled in the 5 T Penning trap, then transferred to the 1 T Penning trap where they are electron cooled again. After that the positrons from the positron source are injected and antihydrogen is formed as shown in Figure 1.3. Here the moiré deflectometer is not build in yet.

and therefore the resonant charge exchange could in principle reach far lower temperatures than three body recombination.

At the moment the antiproton cooling is done via electron cooling. The electrons thermalise with the cryogenic penning trap around them and so far antiproton-temperatures in the range of 400 K have been reached in the Aegis experiment. Further improvements both in temperature and in the amount of antihydrogen will be made when the ELENA ring[3], that is already fully commissioned and connected to the AD, goes into operation. ELENA is an additional deceleration step between the AD and the connected experiments to reduce the energy of the antiprotons from 5.3 MeV to 100 keV. Despite the progress that will arise from the ELENA implementation the mK range necessary for antihydrogen gravity experiments is still out of reach. In [19] it was suggested to use laser cooling on anionic particle species for sympathetic cooling of antiprotons. Despite the successful cooling of ions[22] for anions only evaporative cooling[8] has been achieved so far.

This is the main motivation for this thesis and to accomplish laser cooling on C_2^- the Aegis subgroup Borealis was founded. Borealis has chosen C_2^- as anionic particle species for its approach of laser cooling as it was singled out by [26] as a suitable candidate. C_2^- is produced here by a supersonic expansion valve, to trap it in a charged particle trap and then use laser cooling to

create super cold anions($\sim 100\,\mathrm{mK}$).

Aside from very cold antiprotons the gravity measurement in the Aegis apparatus itself requires also an environment without any magnetic gradients. In the Aegis experiment the measurement will be done by a pulsed antihydrogen beam that goes through a moiré deflectometer[11] and is measured by a position sensitive detector.

When the antihydrogen is formed via resonant charge exchange it is in an excited Rydberg state and has a strong dipole moment. That makes it highly influencable by electrical fields (AC-Stark-effect) that can be used to accelerate the beam towards the moiré deflectometer and magnetic fields (Zeeman effect) that would bring them off course along their gradients. As the antihydrogen production is done in a Penning trap, strong magnetic fields in the range of 1-5 T exist close to the moiré deflectometer and would ruin every position sensitive measurement. To overcome this problem was the second motivation for this thesis.

Chapter 2

Goals of this thesis

This chapter gives a short overview over the tasks that lead to this thesis. The tasks are then described in detail at the beginning of the specific chapters that handle said tasks.

2.0.1 Meissner-tube experiment

The first motivation is to find a way to reduce the fringe fields of the Penning traps used by the Aegis experiment. The field gradient of the magnetic field lines exerts a force $F_B = \nabla B \mu_B m_j$ on the created antihydrogen depending on the field gradient ∇B, the Bohr Magneton μ_B and the magnetic moment m_j of the antihydrogen atom.
To overcome this force it was suggested to use the field-repelling abilities of a superconducting tube and place the moiré deflectometer within the tube. The first goal of this thesis was to simulate the magnetic fields in the Aegis apparatus that are necessary to insert a superconducting tube of a certain size. Furthermore it was necessary to use small superconducting tubes of various dimensions and materials to measure the absence and reflection of a magnetic field close to a permanent magnet for the Aegis collaboration. The so called Meissner Tube experiment is discussed in chapter three.

2.0.2 Borealis experiment

The second and main motivation for this thesis was to build a particle trap that will be used for the laser cooling of anions.
The goal of the Borealis experiment is to create the molecular anion species C_2^-, trap it in a particle trap and use various ways of laser cooling to cool it down to the mK range. If this is successful the lasercooled anions shall then be used for the sympathetic cooling of antiprotons in the Aegis experiment.

14

A detailed overview over the Borealis experiment is given in Chapter four to help understand why some of the tasks done in this thesis were necessary.

Borealis Penning trap

At first the goal was to create a Penning trap with laser access that should be used in the Borealis setup to trap C_2^-. The specifications for this Penning trap included that all electrodes had to be cool-able by liquid nitrogen down to under $100\,\mathrm{K}$ while the vacuum vessel for the penning trap is at room temperature. Further the Penning trap had to have three laser access points, and the diameter of the vacuum vessel had to be smaller than $45\,\mathrm{mm}$ to fit into the borehole of the permanent magnet that was designed as a solenoid. A permanent magnet was necessary because the Borealis Laboratory lacked the possibility of a superconducting solenoid.

Borealis Paul trap

After it turned out that the Penning trap would cause too many Problems to be used in the Borealis setup a Paul trap was suggested. The goal here was to create a so called Digital Linear Paul Trap that should be held on a negative potential hill to slow down the particles coming from the production valve. The Paul Trap should have two multiple laser access points from the side, and have an ejection mode that was called the "kickout mode". The ejection mode accelerates the plasma in the trap radially towards a micro channel plate detector.

The goal of creating a working Paul trap includes all used electronics, a beam bender to deflect the particles towards the trap, a so called deceleration stage to minimize the particle loss during the kinetic energy reduction in front of the trap and the software to calibrate and run all said systems.

2.0.3 A Train Penning trap

A third goal was found when it turned out that the magnetic field in the center of the solenoid that should be used for the Borealis Penning trap was not homogeneous enough to allow simple laser cooling but would still be enough to trap antiprotons. The A Train (**A**ntiproton **Tra**nsporta**t**ion) project uses a slightly modified Borealis Penning trap to create a portable antiproton trap.

The idea here is to implement two $8\,\mathrm{kV}$ electrodes into the trap with the necessary distances to all other conducting parts to stop antiprotons directly from the AD. two titanium foils that are between the vacuum of the AD and

the trap will be used to reduce the kinetic energy into the under 8 keV range. Together with portable batteries and the solenoidal field generated by the permanent magnet of the Borealis Penning trap, a portable antiproton trap of around 190 kg was designed.

Chapter 3

Superconducting shielding for antimatter gravity measurements

The coulomb force is almost 10^{39} times stronger than the gravitational force, what makes gravity measurements with charged particles in the atomic range nearly impossible, as even the smallest stray fields would ruin an accurate measurement. To overcome this, gravity measurements are usually performed on neutral particles, which means for antimatter experiments that antihydrogen ($\bar{H}$) is formed and used.

But even on neutral particles, magnetic and electric fields have an influence if the particles have a dipole moment. For magnetic fields it is the Zeeman effect and for electric fields it is the AC Stark effect, that deflects the particles along magnetic or electric field gradients [17]. In the AEGIS apparatus the antihydrogen is produced by resonant charge exchange and is in a highly excited Rydberg state which provides an even higher dipole moment. The planned precise gravity measurement with a moiré deflectometer as described in the next section is therefore not possible without additional measures.

3.1 Gravity measurement in a moiré deflectometer

The moiré deflectometer [10],[23] uses the moiré effect: The classical overlap of several fine gratings creates a beat with a much larger spatial period. It magnifies one grating with respect to a reference grating. The moiré deflectometer would be mounted at the downstream opening of a Penning trap. At the end of the deflectometer a single particle detector with a high

spatial resolution will be installed.

3.2   Superconducting shielding

While the plan of the Aegis experiment is to use the AC Stark force to accelerate the antihydrogen towards the deflectometer, the magnetic deflection caused by the Zeeman force is a great disturbance and so this chapter will focus on the influence of the magnetic fields from the Penning trap and how to get rid of them.

The superconducting magnets of a common Penning trap produce high fringe fields with strong magnetic gradients especially at the open ends of the solenoids, that deflect all particles with a dipole moment except the ones that fly exactly on the center axis of the magnet to the side and would make them useless for an accurate gravity measurement. Depending on the alignment of the magnetic moment with the magnetic field lines an $\bar{H}$ atom can be classified as a high or a low field seeker. This classification depends only on the alignment of magnetic moment of the atom compared to the magnetic field lines and not on any property of the atom itself. If the magnetic moment is aligned with the field lines in an in-homogeneous field the atom is pulled towards the higher field and a so called high field seeker. If it is aligned against the field lines it is drawn towards the lowest field and so called a low field seeker.

While the high field seekers are deflected towards the center of the Penning trap along the highest field gradient, the low field seekers are deflected to the sides and are lost for a measurement. Both high and low seekers have advantages and disadvantages concerning their flight path. The high field seekers tend to stay inside of the penning trap where the field has the highest strength and if ejected, for example with a pulsed electrode that generates an AC Stark force, they tend to return to the center of the penning trap.

The low field seekers tend to leave the penning trap but also to move away from the center axis. As part of this thesis a publication was created to analyze a possible way of keeping the low field seekers on track by creating a field free area near the antihydrogen production region, to avoid a high loss of antihydrogen particles and to enable a precise measurement. This publication is presented below.

3.3 Publication: Superconducting shielding with Pb and Nb tubes for momentum sensitive measurements of neutral antimatter

TECHNICAL REPORT

Superconducting shielding with Pb and Nb tubes for momentum sensitive measurements of neutral antimatter

A. Hinterberger,[1] S. Gerber and M. Doser

CERN, European Laboratory for Particle Physics,
1211 Geneva, Switzerland

E-mail: alexander.hinterberger@cern.ch

ABSTRACT: In this paper we report on measurements and simulations of superconducting tubes in the presence of inhomogeneous externally applied magnetic fields in a cryogenic environment. The shielding effect is studied for two different tube materials, Pb and Nb, employing Hall sensors in a tabletop experiment. The measured internal and external fields of the tubes agree with the theory of the Meissner-Ochsenfeld effect [1], field trapping of type 2 superconductors, phase transitions and tube geometries. The obtained measurements are compared to a finite element simulation. Next, the simulation model is applied to estimate the shielding effect in the vicinity of a cryogenic Penning trap experiment. The controlled suppression of external magnetic fields is important for future precision experiments in atomic and antimatter physics in cryogenic environments.

KEYWORDS: Superconductive detection materials; Superconductive detectors (bolometers, tunnel junctions etc)

Contents

1 Superconductive shielding

In this paper, the effects of an externally applied magnetic field on superconductor (SC) tubes are studied. The SC tubes are investigated experimentally and via simulations on their property of shielding external magnetic fields. Shielding magnetic fields with SC have been studied for SC Pb cans in [2] and investigated for the application of SC linear accelerators as a Nb can in [3–5] and for bulk and thin layers of Pb, Cu and In in [6]. High-Tc SC shields have been studied in [7] and for the application of SQUID sensors in [8]. NbTi SC magnetic shields and their soldering joints to build various geometries have been studied in [9]. A Meissner shield was further proposed for the ALICE detector in [10].

In the present work, SC tubes made from bulk Pb and Nb at different geometrical aspect ratios of 1.2, 4.4 and 5.1 were studied at 300 K and 4.2 K. The SC field trapping during the phase transitions was investigated along with the Meissner-Ochsenfeld shielding effect at 4.2 K. The magnetic field was provided by a SmCo permanent magnet, which could be oriented along the radial and axial positions relative to the SC tubes.

Theoretically, superconductive shielding is described by the Meissner-Ochsenfeld effect. Here certain solid-state materials are approximated as an ideal SC that behaves as a diamagnet with relative permeability $\mu_r = 0$, reflecting all applied magnetic fields. For an area surrounded by a SC the condition of a quantization of the flux, described in [1], is

$$n\frac{h}{q} = \mu_0\lambda_L^2 \oint j_s dr + \phi. \tag{1.1}$$

For this equation the solutions are a null field or the channeling of the field lines parallel to the SC. Field lines with a perpendicular component to the SC wall are canceled by formation of a counter circular current. Those fields are exponentially suppressed and described by the London equation applied to Ampere's law [11] as

$$\lambda_L = \sqrt{\frac{m}{\mu_0 n q^2}} \qquad (1.2)$$

with the mass of the charge carriers m and the number density n. In the studied case of a SC tube geometry with a wall thickness $D \gg \lambda_L$, the contribution

$$\mu_0 \lambda_L^2 \oint j_s dr \qquad (1.3)$$

becomes negligible and results in a flux

$$n \frac{h}{q} \sim \phi \qquad (1.4)$$

with

$$|q| = 2e, \qquad (1.5)$$

as discussed in BCS-theory [12]. Experiments have confirmed the relation

$$\phi = \phi_0 n = \frac{h}{2|e|n}. \qquad (1.6)$$

in [13]. The magnetic field lines cannot permeate through the present SC geometries, as indicated in figure 5a. Thus depending on the strength of the magnetic field and the diameter of the superconducting tube, the field lines can be displaced out of the open tube ends. A magnetic field that is already present during the process of cooldown can be repelled from the superconducting body or trapped depending on material properties and field conditions.

2 Field trapping

In non-ideal type 1, as well as in type 2 SC, field trapping may occur. During the process of cooldown in the temperature vicinity of the superconducting phase transition, flux lines can get pinned to normal conducting (NC) impurities [14] or grain boundaries [15]. This process of flux pinning [14] occurs normally only in the Shubnikov phase [16] $H_{c1} < H < H_{c2}$, where the critical current flows within a depth necessary to reduce the field inside the SC to H_{c1} At field strengths $H_{c1} < H < H_p$ below a penetration field H_p, fluxlines will not penetrate through the Bean-Livingston barrier, which is caused by the attraction of the Abrikosov vortices to their 'mirror images' near the surface. For a plain type 2 SC with ideal homogeneous surfaces, H_p can be assumed as the thermodynamic critical field H_c as

$$H_p \approx H_c \simeq \frac{\kappa H_{c1}}{ln(\kappa)} \approx \sqrt{H_{c1} H_{c2}} \qquad (2.1)$$

with $\kappa = \frac{\lambda}{\xi}$ [17]. Here λ is the penetration depth and ξ is the coherence length. For the typical values of Nb $H_{c1} \approx 130 \, mT$ and $H_{c2} \approx 280 \, mT$ this would result in $H_p \approx 190 \, mT$. The number of pinned flux lines can be reduced by applying a temperature gradient ΔT to the SC during cooldown. This

can cause an effect of driving the field out of the bulk material through the not-yet superconducting part [18]. Further in practice, field trapping can also be reduced by special preparations such as annealing the superconductor and surface polishing [19].

In the case of a SC tube geometry, most field trapping is expected in the longitudinal direction parallel to the z-axis of the tube.

3 Experimental setup

The following experimental setup was used to study the behavior of SC tubes in externally applied magnetic fields. Two different lenght SC tubes made of Pb (99.95%) and Nb (300 R.R.R.) respectively were studied in the presence of various external magnetic fields. A permanent magnet mounted on a manipulator allowed us to apply the fields from different positions, orientations and field strengths. The employed SmCo permanent magnet consisted of a cylinder of dimensions $r = 5$ mm and $l = 20$ mm and exhibited an axial magnetic field strength of 40 mT at a distance of 10 mm at 300 K. Two magnetic Hall sensors, one mounted at the center position inside the SC tubes and one adjacent to the permanent magnet, measured the inner magnetic field strengths B_i and outer B_o. A temperature range of 300 K down to 4.2 K was investigated. The Hall sensors were made from an AlGaAs/GaAs chip (MagCam CHS-6 [20]) and could be operated at room temperature and at a LHe environment. Figure 1, left side, depicts the liquid helium bath cryostat with a viewport, showing the Pb-tube at boiling helium temperature and atmospheric pressure. The sensor chip was fabricated with six Hall sensors of various sensitivities. The sensor with the highest sensitivity range was used (see figure 1 right picture). The sensor chips were Al wirebonded and glued to a PCB board (ENEPIG on FR4). The Hall sensors were mounted (G10 structures) with tilts of 45° in the three Cartesian angles relative to the SC tube to determine the present radial and axial magnetic field components. As the electron population in the conducting band of the sensor depletes at cryogenic temperatures within seconds the sensors were activated (conducting band repopulated) with light at 890 nm (LED TSHF5210, 70 mA) over a duration of 1 min which guaranteed a stable measurement time of several hours. The readout was performed with two multimeters (Keithley 2000) connected to a LabView program. The constant Hall current to the sensors was provided via two source-meters (Keithley 2410) at 0.2 mA. The temperature of the SC tube was monitored during the entire measurement (TVO 205 sensor connected to a Keithley 2000). To set the temperature of the tubes, two resistive heaters were attached to the outside of the SC ($R = 10\,\Omega$ and $100\,\Omega$).

Due to the fact that the offset and the sensitivity of the Hall sensors are temperature dependent [20] and the exact field strength of the permanent magnet was modeled from [21], all values of the magnetic fields are obtained with only relative precision. Here, we deduce the measured magnetic flux of the Hall sensors to be about a factor of 3.4 weaker at liquid helium temperatures than at room temperature, which is considered in the results.

4 Results

In the following the behaviour of SC tubes of various aspect ratios are discussed for materials of Pb and Nb. For each measurement the magnetic field flux density is plotted versus the relative magnet-tube distance. The data is compared to a finite element simulation of the SC described in section 5 for the different tube geometries. In a first measurement, the magnet-tube distance is

Figure 1. Experimental setup build up at the Cryogenic Laboratory at CERN. *Left side:* picture of the LHe bath cryostat with a viewport showing one of the Pb tubes and the adjacent magnet holder. *Right side:* picture of the outer Hall sensor and LED mounted on a PCB board. The SmCo magnet is seen in dark gray mounted next to the PCB. The magnetic field produced by coiled cables is below 10^{-8} mT. The lower picture shows the Hall sensor and the Chip inside the long lead tube.

varied in the on-axis direction with h_1 the distance measured from the magnet to the tube middle position $L/2$ of length L. In a second measurement, the off-axis dependence of the magnet distance was recorded. Here h_2 is the distance to the tube middle position $L/2$ and the movement direction of the magnet has a fixed off-axis displacement in comparison to the tube axis of 47 mm. In a third measurement, the radial distance magnet-tube r is varied with the magnet initially positioned at the middle of the tube. The three sets of measurements are plotted for each tube geometry in figure 2a, e for Pb and in figure 3a, e for Nb. The magnet was moved in steps of 10 mm for the axial and 3 mm for the radial measurements but a continuous data readout was taken. To avoid errors from vibrations, each data point was taken after at least 10 seconds of waiting time. The size of the steps was measured with a ruler and by using several marks on the aperture.

The results of the on-axis measurement are plotted in figure 2b, f for Pb and in figure 3b, f for Nb. Here the magnet was initially at an axial position of $h_1 = 220$ mm and $r = 0$ mm. Figure 2c, g and figure 3c, g show the results from the off-axis measurements. From an initial position of $h_2 = 220$ mm and $r = 47$ mm, the magnet was moved parallel to the tube axis. The radial measurement is plotted in figure 2d, h for Pb and figure 3d, h for Nb starting at an initial magnet position in the tube middle and at a radius of $r = 47$ mm. The magnet was then moved closer to the tube. Once the magnet reached the closest of $h_{1\,min} = 5$ mm, $r_{min} = 7$ mm constraint by the magnet mount and the outer tube diameter, the magnet was again moved to the initial position using the same step sizes.

The used Hall sensors were not calibrated to a null-field at 300 K and 4 K and exhibited a temperature dependent sensitivity and offset.

Due to this, all data are expressed in relative values. To compare the individual measurements, an offset was added in each plot to bring the initial data points of 300 K and 4.2 K closer to each other. This was performed for both the outer and inner sensor data. An offset was added to the simulation graph to have a common starting value with the data points of the inner sensor. The error on all measurements depended on the distance from the sensor to the magnet and even more on the angle of the field lines of the magnet and the reflected field penetrating the Hall sensors. In the case of the axial measurements on short tubes, the Gaussian $\frac{1}{\Sigma}$ error ranges from $\pm 8 \, \mu T$ for distances of $\sim 100 \, mm$ to $\pm 3 \, mT$ for the closest distance. Thus, for the plots the following notations were made:

- Black squares: measurements at 300 K.

- Red triangles: measurements at 4.2 K.

- Blue star: simulation at 4.2 K

- Green circle: second recording at 4.2 K for the on-axis measurement for the short Pb tube.

- Full symbols: data recorded by the Hall sensor inside the tube.

- Empty symbols: data recorded by the outer Hall sensor mounted on the magnet holder.

- h_1: distance of the magnet from the tube middle (L/2) with the cylinder axis of the magnet and the tube aligned.

- h_2: distance of the magnet from the tube middle (L/2) with the cylinder axis of the magnet parallel to the tube axis with a radial distance of $r = 47 \, mm$.

- r: distance of the magnets surface (10 mm diameter) to the center of the tube axis.

4.1 Long lead tube

Figure 2a) depicts the measurement for the case of a Pb tube of length $L = 200 \, mm$ and diameter $D = 45 \, mm$. The inner sensor measured no change of the magnetic field during the movements at a temperature of 4.2 K. The tube created a diamagnetic field that increased the field measured by the outer sensor. This can be seen both axially (in figure 2b, c) and radially (in figure 2d). Further, at a distance below $h_1 = 100 \, mm$, the magnet induced a field at 4.2 K in the Pb tube that can be seen in figure 2b at 105 mm and in c during the movement. This hysteresis is typical for type 2 SC. In the Shubnikov phase [16] flux lines can enter the superconductor, get caught by pinning centers [14] and thus do not exit the superconductor when the magnet gets moved away. From the figures a shielding effect can be observed at 4.2 K. Here all measurements of the inner sensor stay below a field change of 0.05 mT compared to a change of 0.3 mT for the equivalent 300 K measurement. The shielding effect is also seen in the simulation To explain the strong hysteresis in figure 2b, c, one must know that the long lead tube measurement was performed in another way than the other three measurements. As it was originally planned to display the recordings at six different magnet positions only the measurement points on these known positions could be taken. This also means
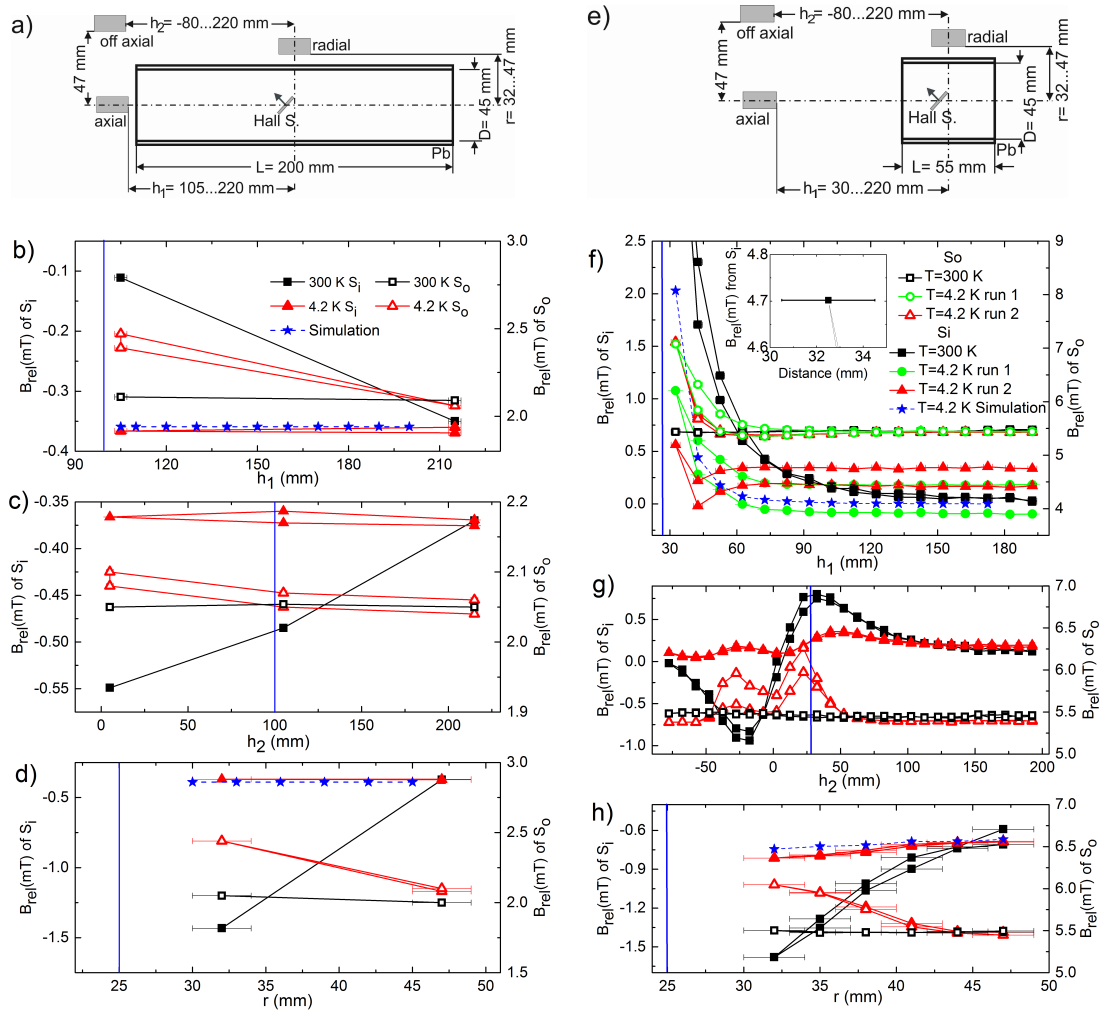
Figure 2. Measured relative magnetic field changes inside and outside of **Pb** tubes of two different lengths. The empty symbols depict the outer Hall sensor and the solid symbols the inner Hall sensor. Black squares: magnetic field at 300 K. Red triangles: magnetic field at 4.2 K. The blue solid stars indicate the simulated field at 4.2 K at the position of the inner sensor. The blue vertical line indicates the top end of the tube. In figure 2a, e the tube geometry and the three measurement sets are sketched: in figure 2b, f the magnet was moved relative to the tubes in the on-axis direction; in figure 2c, g in the off-axis direction and in figure 2d, h in the radial direction. An offset was added to the relative values in each measurement and in the simulation to compare the values at the same starting points $h_1 = h_2 = 220$ mm and $r = 47$ mm.

that the magnet was moved to different positions in a certain order which explains why in figure 2b the magnet passed the position $h_1 = 105$ mm two times and was able to build up a hysteresis in between. This also implies the hysteresis effect in figure 2c. Here the magnet was moved to different positions closer to the tube as well in between the two measurement points at $h_2 = 5$ mm.

4.2 Short lead tube

Figure 2e displays the measurement on a Pb tube with dimension of $L = 55$ mm and $D = 45$ mm. Here, in figure 2f the inner sensor observed an increase in the magnetic field at 300 K and also in

the SC phase at 4.2 K. This is caused by two factors: the magnetic field leaking into the tube as seen in figure 5b and the diamagnetic field built up by the SC to shield against the B-field of the magnet. In figure 2f the measurement at 4.2 K was performed twice to verify the observed hysteresis effect. It can be seen that the second on-axis measurement (run 2) starts at the same field as the end of run 1. Due to the limited number of pinning centres in the tube, the hysteresis in run 2 is smaller than in run 1. The simulation reproduces the increase in field for smaller distances, however shows a factor two higher value for the closest point. This is most likely due to high sensitivity to unintended movements in radial direction, which manifest a larger error at close distances. Compared to the measurement at 300 K, the shielding effect is still visible but not as strong as in the case of the longer Pb tube. The measured higher field values in figure 2f, h are because in the short lead tube, the magnet could be moved 75 mm closer in h_1 to the inner Hall sensor. Thus at $h_1 = 105$ mm the inner sensor at 300 K shows about 0.2 mT difference in figure 2f compared to the long lead tube in figure 2b.

Figure 2g pictures the off-axial measurement. Here at 300 K a clear change of the direction of the magnetic field is visible as the inner sensor recorded the magnetic south and north part of the vector field. When the tube is in the SC phase, the inner sensor observed a field increase in the same direction on both end positions of the tube when the magnet passed by. Leakage of the field at the ends of the tubes were recorded, with the primary magnet's field being mostly blocked by the SC.

For the measurement the inner sensor had a small axial displacement of order of mm from the tube center position. Together with the tilt of the sensor chip of $45/^o$ and the magnetic pattern of the SmCo this led to the observed asymmetry of the heights of the two maxima at $h_2 = -25$ mm and $h_2 = 50$ mm in the 4.2 K curve. Further, the local minima is not at $h_2 = 0$ mm but at a distance of $h_2 \sim 10$ mm. Similarly, the measurement at 300 K showed the turnover point in the field shifted in h_2 by the same amount. Similar to the inner sensor at 4.2 K, the outer sensor measured a stronger field at the ends of the tube compared to in the middle position. The outer sensor also recorded a hysteresis between the movement closer and away from the tube.

In figure 2h the radial measurement shows a slight field change in the SC-phase. Because of the small aspect ratio of the tube, the magnetic field leaked into the open ends. As expected, the outer sensor saw an increase in the magnetic field close to the tube with also a small hysteresis effect visible. At 300 K, the slight hysteresis of the inner sensor most likely derives from a small inaccuracy of r.

4.3 Long niobium tube

Figure 3a depicts the used Nb tube with dimensions $L = 179$ mm and $D = 35$ mm. For the on-axis measurement with the tube in the SC-phase, seen in figure 3b, the inner sensor recorded an almost complete shielding against the magnet compared to the measurement at 300 K. Plotted in the same graph, the outer sensor measured an increase in the field strength with smaller h_1 as a result of the diamagnetic field from the SC.

Figure 3c shows the off-axial measurement. At 300 K, the inner sensor measured the direction change of the magnetic field, similarly to figure 2c, g. For this measurement the inner sensor was mounted intentionally 20 mm closer to the top of the tube to yield more sensitivity to the shielding effect. At 4.2 K the inner sensor recorded no changes in the field strength for various distances. Thus, with the tube in the SC-phase, the magnetic field is shielded completely. The accompanying
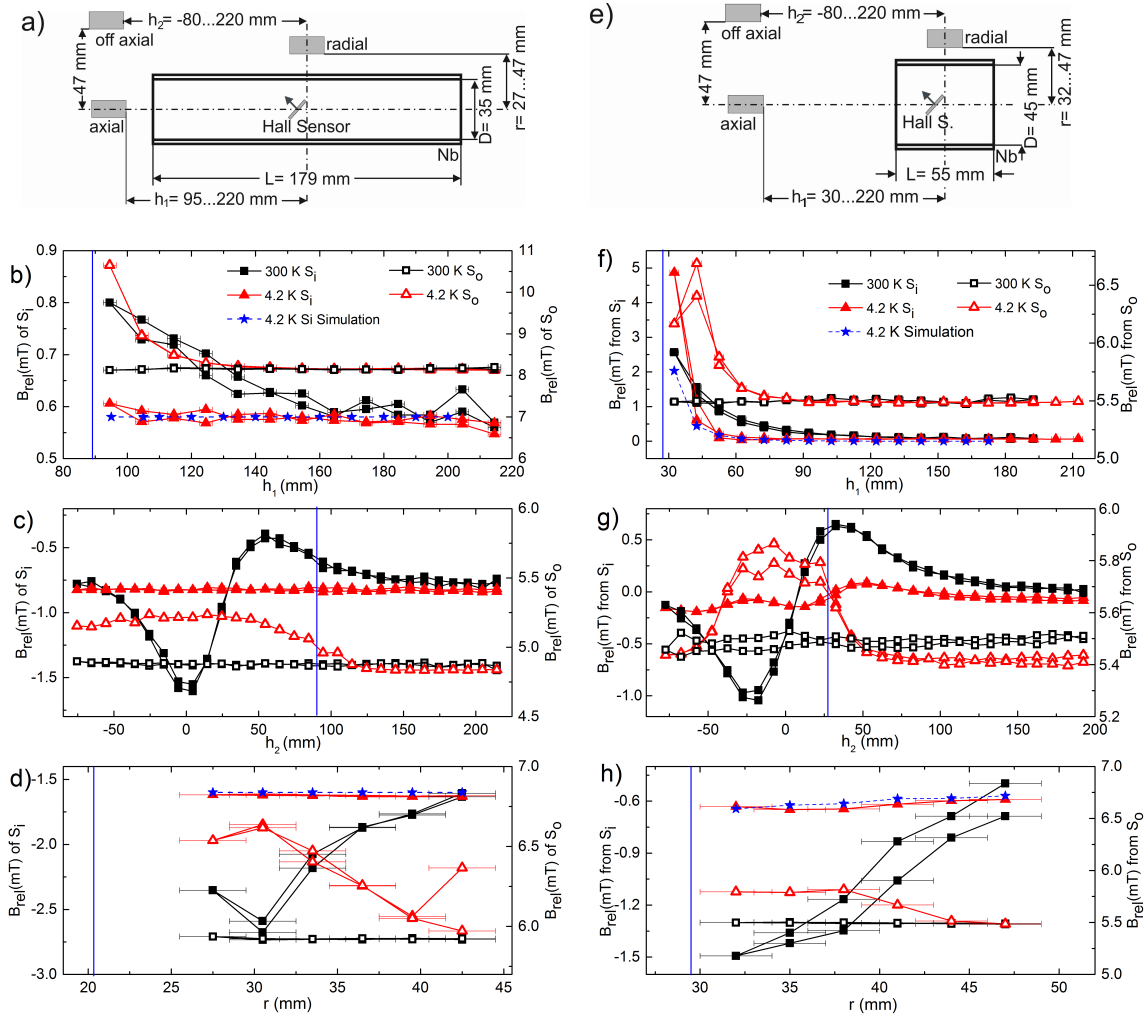
Figure 3. Measured magnetic field inside and outside of **Nb** tubes of two different lengths. The empty symbols depict the outer Hall sensor and the solid symbols the inner Hall sensor. Black squares: magnetic field at 300 K. Red triangles: magnetic field at 4.2 K. The blue solid stars indicate the simulated field at 4.2 K at the position of the inner sensor. The blue vertical line indicates the top end of the tube. As sketched in the figure 3a, e the magnet was moved relative to the tubes: figure 3b, f shows on-axis direction; figure 3c, g shows off-axis direction and figure 3d, h indicates the radial direction. An offset was added to the relative values in each measurement and in the simulation to compare the values at the same starting points at $h_1 = h_2 = 220$ mm and $r = 47$ mm.

increase of the magnetic field alongside the tube is recorded by the outer sensor. Due to the tube diameter of $D = 35$ mm, the r position of the outer sensor was 10 mm further away from the magnet compared to the Pb tubes. Therefore, the measured diamagnetic field on the tube edges was recorded to be smaller for Nb.

Figure 3d shows that the tube also shields the radial influence of the field completely. The changes of the closest point to the tube in the opposite direction of the inner sensor at 300 K and at 4.2 K are caused by the magnet slightly touching the tube and therefore changing its angle. As

mentioned before the sensor has shown to be very sensitive to the angle of the magnetic field. Further, in this measurements no definite signs of a hysteresis loop could be found.

4.4 Short niobium tube

Figure 3e sketches the used Nb tube with dimensions of $L = 55$ mm and $D = 45$ mm. As described for the case of the short Pb tube for figure 2e, only a partially shielding effect was observed.

In figure 3f a residual shielding effect is visible in the SC-phase. For a large range of h_1 the simulation reproduced the measured values. The closest point of the inner sensor at 4.2 K at $h_1 = 30$ mm deviates about 3 mT from the simulated point. We attribute this to the afore mentioned sensor's high sensitivity to unintended movements in radial direction, which manifest a larger error at close distances. At the same time, the outer sensor at 4.2 K and $h_1 = 30$ mm is also out of order. We would expect the value to be higher than the point at $h_1 = 45$ mm, given the magnet in the correct position. Figure 3g shows a very similar graph as in figure 2g for Pb. For the case of Nb, at 4.2 K, the outer sensor measured a less pronounced diamagnetic field on the edges of the tube and a small hysteresis, which is due to the fact that Nb is a type 2 SC. In figure 3h the measurement of the radial movement of the magnet is plotted. Because of the small aspect ratio of the tube, the field could leak inside. The outer sensor also recorded a rising diamagnetic field with closer distances.

4.5 Field trapping

In the following section, the process of field trapping is studied in more detail. During cooldown the magnet was initially positioned at the side of the tube at $h_2 = 0$ and at the radial distance $r = 32$ mm. After reaching the SC-phase, the magnet was brought to the far distance of $h_2 = 220$ mm. After reaching the NC-phase again the magnet was brought back to the initial position. In the long Pb tube, figure 4a, the inner Hall sensor recorded a change of the magnetic field despite being in the SC-phase. This is explained as the flux lines in the Shubnikov phase [16] leaked into the tube.

For the long Nb tube, figure 4b, the plot on the left side of the blue line indicates the trapped field when the magnet was at the close-by position $h_2 = 0$ mm and $r = 27$ mm at the time when the tube became a SC. While the tube remained in its SC-phase, the magnet was moved to the farthest possible distance of $h_2 = 220$ mm and $r = 47$ mm. At the blue line sufficient helium has boiled away for the tube to become a NC. As expected, the trapped field then disappeared. At a temperature of 11.5 K, the red line indicates when the magnet was brought back to the close-by position of $h_2 = 0$ mm and $r = 27$ mm.

The height difference between the left side of the blue line and the area between blue and red line (trapped field disappearing) of this measurement shows that 92.5% of the field was trapped both due to the present geometry and material. Applying a temperature gradient of approximately 3 K over a tube length of $L = 179$ mm using two heaters (10 Ω and 100 Ω) did not significantly change the value of the trapped field.

5 Simulations

To show the shielding effect and the behavior of the magnetic field lines, several simulations were performed with COMSOL 5.2 with various tube geometries and are shown in figure 5a. As COMSOL does not implement a relative permeability of 0, a permeability of $\mu_r = 10^{-16}$ was used throughout this paper to calculate the magnetic fields close to the superconductor.
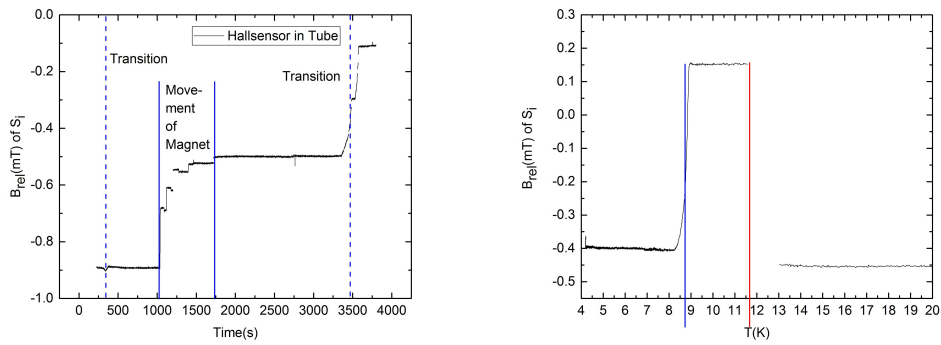
(a) Inner tube diameter D: 45 mm.
Tube length L: 200 mm.

(b) Inner tube diameter D: 35 mm.
Tube length L: 179 mm.

Figure 4. a) Pb tube. The left dashed line indicates the transition of NC- to SC-phase. In between the solid lines the magnet was moved. The right dashed line indicates the transition from the SC- back to the NC-phase. b) Nb tube. The solid (blue) line shows the phase transition at ~ 9 K. The solid line (red) shows the point, where the magnet was brought to same position as during the cooldown process.

Figure 5a depicts the case where the tube is in a Meissner phase without a field being present during the transition. Here, all field lines are shaped around the tube and can only enter through the open endings, where they are forced back out by the diamagnetism of the SC.
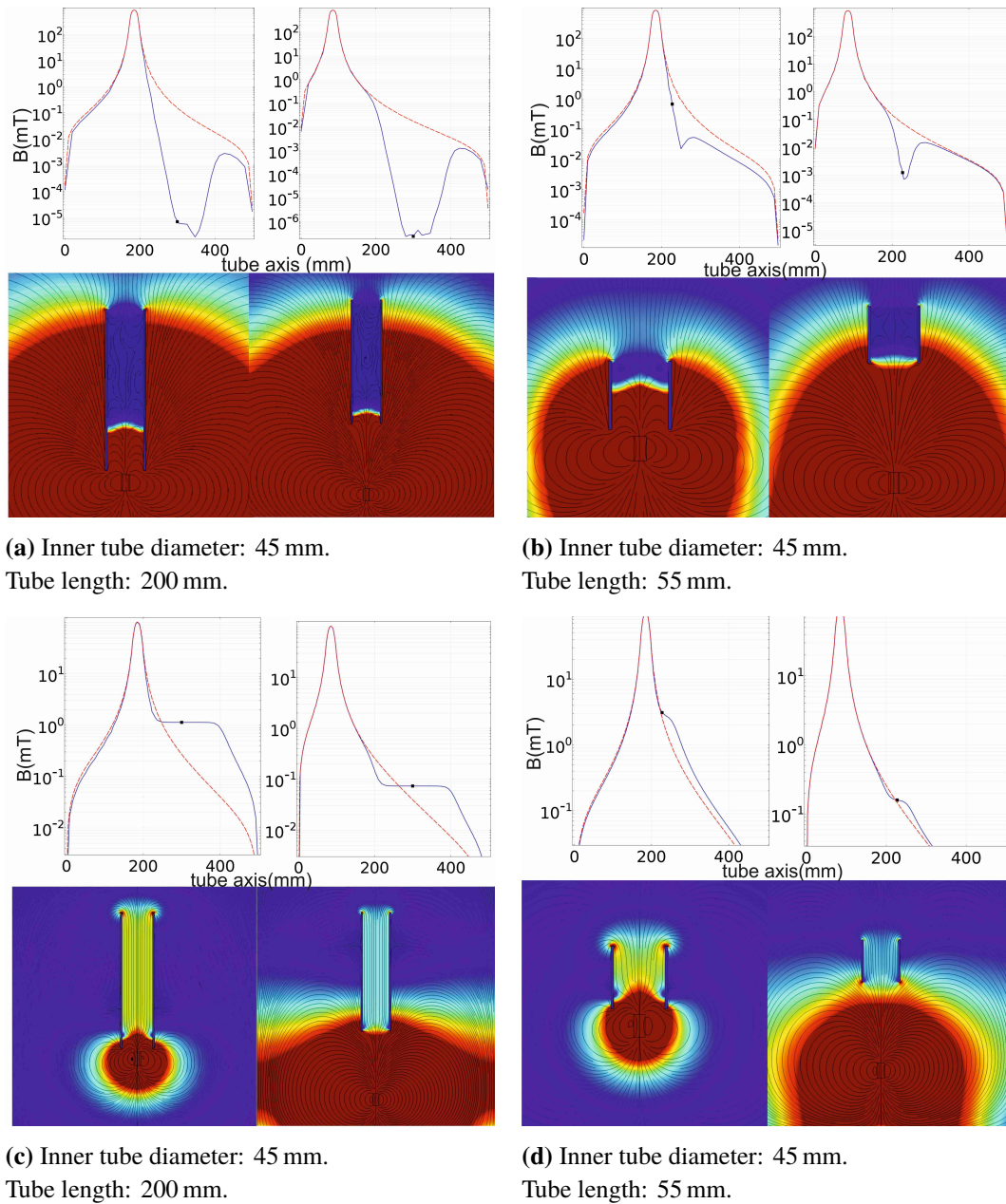
In figure 5b a tube with an aspect ratio of 1.1 was used as in the experiment. The line graphs show that the center of the tube has a much higher field compared to the center of figure 5a. Figure 5a and figure 5b indicate that the field lines of the magnet intrude from both sides into the tube. To show the field trapping effect of the tube geometry, two sketches, figure 5c and figure 5d were calculated. The plots show that the fields present during phase transition are pushed out of the SC and depending on their former position resided inside or outside the tube. The field lines that are moved inside of the tube are flux quantized [1] and repel each other and the tube body. Therefore they exist only in configurations of straight parallel lines. The line graphs indicate that the field stays constant when the field lines are trapped and parallel, in accordance with [1, 18]. In the case of the small aspect ratio tube from figure 5d the field lines were not sufficiently pressed together to be parallel, so the field strength does not stay constant over the tube length.

In the case of the high aspect ratio Nb tube of 4.44, the parallel field lines exhibit a negligible radial field gradient, (figure 6)

6   Magnetic shielding at the AEgIS experiment

In this section, the application of a Meissner-Ochsenfeld tube as a shield of residual magnetic field from a Penning trap magnet and environmental stray fields is discussed.

In the AEgIS experiment at the antiproton decelerator (AD) facility at CERN, an interferometer is proposed to measure the acceleration of antihydrogen ($\bar{\text{H}}$) due to Earth's gravity [22]. The scheme of using matter wave interferometry to resolve g of $\bar{\text{H}}$ has been proposed also as a suitable method in [25–27]. Amongst them, a promising design constitutes the Talbot-Lau interferometer (TLIF)

(a) Inner tube diameter: 45 mm.
Tube length: 200 mm.

(b) Inner tube diameter: 45 mm.
Tube length: 55 mm.

(c) Inner tube diameter: 45 mm.
Tube length: 200 mm.

(d) Inner tube diameter: 45 mm.
Tube length: 55 mm.

Figure 5. a), b) Simulations of SC tubes that express shielding of the inner part of the tube against the axial magnetic field. c), d) Sketch of SC tubes guiding a field trapped by the tube geometry through the SC. Red dashed lines show the dependencies for the NC-phase and the blue lines for the SC-phase.

first described by [28]. A TLIF operates by measuring the phase change that occurs when splitting and recombining atomic wave functions, typically using three periodic gratings, and can reach sensitivities of relative position changes on the order of the de Broglie wavelength of the examined particles [29].Using a TLIF the phase shift induced by gravity has been measured for neutron beams by rotating the IF grating plane to control the influencing effect of g during the measurement [30].In a similar scheme, the axially emitted fraction of H̄ could be allowed to traverse a TLIF attached to the downstream opening of the Penning trap.
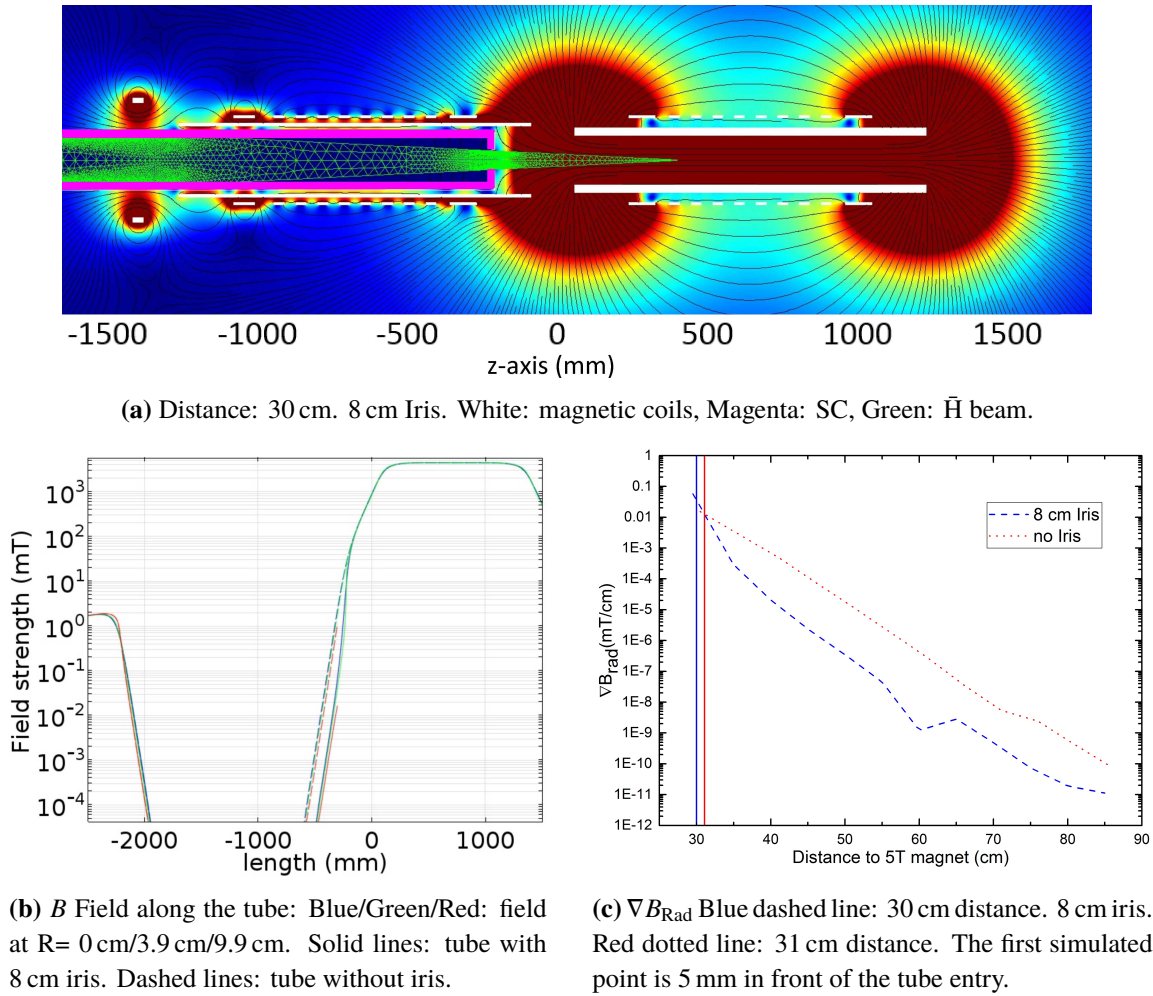
For such a setup in AEgIS, the antiatoms are proposed to be produced from resonant-charge-exchange of its constituents antiprotons and positrons [23] resulting in Rydberg states of $n \sim 30$ [22]. The total angular momentum J of the H̄ are then randomly projected on to the magnetic field axis of the Penning trap to a broad distribution of about $-30 < m_J < 30$. However, a magnetic field gradient of 1 µT/cm acting on a H̄ in the $m_J = 30$ state during its passage through the TLIF can mimic the effect of gravity due to the Zeeman force $F_b = \nabla B \, \mu_B \, m_J$. To have complete knowledge of magnetic fields, or suppress them, to such accuracies poses a critical challenge to AEgIS and similar experiments, which are proposed to be carried out at cryogenic temperatures. Considering the geometrical constrain of the AEgIS apparatus [32], a SC tube of material Nb with length of 2 m and 0.2 m diameter could be placed within the apparatus in the cryogenic bore hole approximately 0.31 m away from the 5 T coil of the Penning trap. For this experimental configuration a simulation was performed with the results shown in figure 6a. At the proposed SC position in the setup and with the assist of the installed correction coils, the magnetic fields strength around the SC tube can then be kept under H_{c1} 130 mT of Nb [32–34] with the calculated value of the residual field of 116 mT on axis at R=0. A SC tube then attenuates the field by a factor of 5.6 to 20.5 mT. According to the simulation from figure 6c a radial gradient of 5.6 mT/R at the SC tube entrance at R=0.1 m causes an acceleration due to the Zeeman force in vertical direction of $a = F_b/m_{\bar{H}} = 9538$ m/s^2. However, 40 cm inside the SC tube the acceleration due to the magnetic field gradient would have decreased to 9.08×10^{-4} m/s^2 for the same $m_J = 30$ state. In the center of the 2 m tube, the residual field is 5.4 mT, which would be reduced the field to below 3.6×10^{-7} mT.

To further suppress the magnetic fields inside the SC tube, a Nb iris of 80 mm can be electro-welded [35] onto the front open end of the SC tube without blocking the H̄ beam emitted from the Penning trap. This would enhance the performance of the SC tube by approximately a factor of 100 (as pictured in figure 6a). In this case, the tube could be mounted even closer, e.g. 30 cm distance to the 5 T magnet and the field would further decrease from 124 mT at the beginning of the tube by a factor of 13.5 to 9.2 mT. Additionally, the field of 5.4 mT in the center of the tube would be suppressed to under 2.4×10^{-9} mT as shown in figure 6b.

In figure 6c the radial gradient of a tube with 8 cm iris and a tube without iris is compared. Assuming complete field freezing at the phase transition, only the constant Earth's magnetic field of ~ 50 µT is considered in the simulation. Hence, a Meissner shield can greatly assist in a measurement of the gravitational acceleration g of H̄.

7   Conclusion

In this manuscript, the SC shielding effect of Pb and Nb tubes for tube aspect ratios of 1.2, 4.4 and 5.1 was studied. Nb tubes exhibit a significantly better performance in shielding. This is most

(a) Distance: 30 cm. 8 cm Iris. White: magnetic coils, Magenta: SC, Green: H̄ beam.

(b) *B* Field along the tube: Blue/Green/Red: field at R= 0 cm/3.9 cm/9.9 cm. Solid lines: tube with 8 cm iris. Dashed lines: tube without iris.

(c) ∇B_{Rad} Blue dashed line: 30 cm distance. 8 cm iris. Red dotted line: 31 cm distance. The first simulated point is 5 mm in front of the tube entry.

Figure 6. Tube length: 2 m. Inner tube diameter: 20 cm. Straight field lines in superconductor are due to $\mu_r = 10^{-16}$ and not 0.

likely explained due to higher impurities in the Pb material and the more pronounced presence of a Shubnikov phase [16]. This effect was also visible in the presence of a hysteresis in the lead tube measurements. To achieve high shielding, according to the simulations and the results, the SC tube should be made of a high RRR Nb ($RRR \geq 300$) rather than Pb and exhibit a large aspect ratio as this creates a larger area of low field. Here an aspect ratio of > 5 is found to be sufficient to suppress external present magnetic fields by a factor of at least 2×10^7 or with an 8 cm iris by a factor of at least 2×10^9.

Further, to reduce field trapping by impurities and grain boundaries, a resistive heater could be mounted on one end of the SC with the other end brought into thermal contact with liquid helium. As the power to the heater is gradually lowered, the tube is transferred adiabatically into Meissner phase. When ΔT is sufficiently large, the field trapped by impurities is predicted to be significantly reduced [18]. Furthermore, the tube should be annealed to increase the size of the grains and therefore reduce the number of grain boundaries.

The trapped field caused by the tube geometry can not be moved out. However, the trapped field will be free of a radial gradient, as seen in figure 5c. The presented results are particularly

interesting for any experiment faced with the challenge of carrying out momentum measurements sensitive to the Earth's gravitation acceleration on atoms.

Acknowledgments

References

[1] B.S. Deaver and W.M. Fairbank, *Experimental Evidence for Quantized Flux in Superconducting Cylinders*, *Phys. Rev. Lett.* **7** (1961) 43.

[2] P.V. Vorobev, *Detectors of Quasimagnetic Interactions*, *BUDKER-INP-2000-45* (2000).

[3] J. Popielarski et al., *RIA Superconducting Drift Tube Linac R&D*, *DE-FG02-06ER41412 Amendment A000*, (2009), https://www.osti.gov/scitech/biblio/952940.

[4] R.E. Laxdal *Review Of Magnetic Shielding Designs Of Low-Beta Cryomodules*, in *WEIOD01 Proceedings of SRF2013, Paris, France*, (2013), http://accelconf.web.cern.ch/AccelConf/SRF2013/papers/weiod01.pdf.

[5] W. Hartung et al., *Production cavities and cryomodules for a heavy ion re-accelerator at Michigan State University*, in *Proceedings of SRF2009, Berlin, Germany TUPPO011*, http://accelconf.web.cern.ch/Accelconf/SRF2009/papers/tuppo011.pdf.

[6] G. Fischer and R. Klein, *Microwave Study of Proximity Effects in Superconductivity*, *Physik Kondens. Materie* **7** (1968) 12.

[7] H. Kado and M. Ichikawa, *Performance of A High-Tc Superconducting Fault Current Limiter — Design of A 6.6 kV Magnetic Shielding Type Superconducting Fault Current Limiter*, *IEEE Trans. Appl. Superconduct.* **7** (1997) 993.

[8] H. Ohta et al., *Neuromagnetic SQUID Measurement in a Superconducting Magnetic Shield*, *IEEE Trans. Appl. Superconduct.* **9** (1999) 4073.

[9] K. Seo, S. Nishijima, K. Katagir and T. Okada, *Evaluation of solders for superconducting magnetic shield*, *IEEE Trans. Magn.* **27** (1991) 1877.

[10] P. Akishin et al., *Meissner Shield as Option of Open Geometry Beam Shielding for ALICE Muon Arm*, *ALICE-INT-1999-44* CERN-ALICE-INT-1999-44 (1999).

[11] C. Kittel, *Introduction to Solid State Physics*, John Wiley & Sons., pp. 273–278, ISBN 978-0-471-41526-8 http://tocs.ulb.tu-darmstadt.de/133176916.pdf.

[12] J. Bardeen, L.N. Cooper and J.R. Shrieffer, *Theory of Superconductivity*, *Phys. Rev.* 108 (1957) 1175.

[13] W. Buckel and R. Kleiner, *Superconductivity*, Wiley-VCH (2004).

[14] D. Dew-Hugh, *Flux pinning mechanisms in type II superconductors*, *Phil. Mag.* **30** (1974) 293.

[15] J. Viljamaa, L. Rostila, P. Kováč, T. Melíšek, A. Hinterberger and M. Reissner, *Comparison of Different Critical Current Density Models for Undoped Monofilamentary Ti-Sheathed MgB2 Tapes*, *J. Supercond. Nov. Magn.* **24** (2011) 287.

[16] L.V. Shubnikov, V.I. Khotkevich, Yu.D. Shepelev and Yu.N. Ryabinin, *Magnetic properties of superconducting metals and Alloys*, Translated and reprinted from *Zh. Eksper. Teor. Fiz.* **7** (1937) 221, http://ujp.bitp.kiev.ua/files/journals/53/si/53SI10p.pdf.

[17] L. Burlachkov, *Magnetic relaxation over the Bean-Livingston surface barrier*, *Phys. Rev.* **B 47** (1993) 8056.

[18] T. Kubo, *Flux trapping in superconducting accelerating cavities during cooling down with a spatial temperature gradient*, *PTEP* **2016** (2016) 053G01 [`arXiv:1601.02118`].

[19] F. Habbal and W.C.H. Joiner, *Correlation between changes in pinning strength and flux flow noise due to annealing in a Type II superconductor*, *Phys. Lett.* **A 60** (1977) 434.

[20] K. Vervaeke, *Microscopic Hall sensors for magnetometry and local magnetic imaging*, Ph.D. Thesis, Katholieke Universiteit Leuven Faculteit Wetenschappen Departement Natuurkunde En Sterrenkunde, https://lirias.kuleuven.be/handle/1979/822,

[21] ARNOLD The magnetic Products group of SPS, *Using permanent magnets at low temperatures*, http://spontaneousmaterials.com/Papers/TN_0302.pdf.

[22] AEGIS collaboration, *Exploring the WEP with a pulsed cold beam of antihydrogen*, *Class. Quant. Grav.* **29** (2012) 184009.

[23] W. Demtroeder, *Demtroeder Experimental Physics 3*, Springer, (2010), pp. 153–156, ISBN 978-3-642-03910-2.

[24] S. Aghion et al., *A moiré deflectometer for antimatter*, *Nature Commun.* **5** (2014) 4538.

[25] T.J. Phillips, *Antimatter gravity studies with interferometry*, *Hyperfine Interact.* **109** (1997) 357.

[26] M.K. Oberthaler, *Anti-matter wave interferometry with positronium*, *Nucl. Instrum. Meth.* **B 192** (2002) 129.

[27] P. Hamilton, A. Zhmoginov, F. Robicheaux, J. Fajans, J.S. Wurtele and H. Müller, *Antimatter Interferometry for Gravity Measurements*, *Phys. Rev. Lett.* **112** (2014) 121102.

[28] E. Lau, *Beugungserscheinungen an Doppelrastern*, *Annalen Phys.* **437** (1948) 417.

[29] H.F. Talbot Esq. F.R.S., *LXXVI. Facts relating to optical science. No. IV*, *Phil. Mag.* **9** (1836).

[30] R. Colella, A.W. Overhauser and S.A. Werner, *Observation of Gravitationally Induced Quantum Interference*, *Phys. Rev. Lett.* **34** (1975) 1472.

[31] M. Oberthaler, private communication.

[32] *AEgIS Proposal*, http://aegis.web.cern.ch/aegis/Proposal/Proposition.pdf.

[33] A. Dudarev et al., *Construction and Test of the Magnets for the AEgIS Experiment*, *IEEE Trans. Appl. Superconduct.* **23** (2012) 4500304.

[34] K. Saito, *Critical field limitation of the niobium superconducting rf cavity*, in *The 10th Workshop on RF Superconductivity, 2001, Tsukuba, Japan*, http://accelconf.web.cern.ch/AccelConf/SRF01/papers/ph003.pdf.

[35] J.L. Kirchgessner, *Forming and welding of Niobium for Superconducting Cavities*, in *The Third Workshop on RF Superconductivity, Argonne National Laboratory, Illinois, U.S.A.*, http://epaper.kek.jp/srf87/papers/srf87e05.pdf.

3.4 Further investigations on superconducting shielding

After the publication a few further improvements have been made to decrease the distance between the niobium tube and the Penning trap magnets, so that less particles would be lost due to a larger entrance angle.

One of these improvements is to make round frontal edges on the tube because sharp edges usually lead to field compression in a magnetic field which increases the local field around the edges and could bring the local field over the lower critical Field Bc1 and so bring the superconductor into the Shubnikov phase. Then fluxlines could penetrate the tube and influence the measurements. According to a simulation 3.1 a curve radius of 20 mm around the outer front part is the optimum for a tube with 200 mm diameter. Further an iris of 60 mm seems to be better than the 80 mm described in the publication. With curved edges the superconducting tube can move up to 29 cm to the five tesla magnet without loosing its superconductivity. Further the field gradient next to the 80 mm iris near the tube entrance is parallel to the tube axis and so the $\bar{H}$ atoms are accelerated towards the field free area and not to the side. Another improvement would be to anneal the tube. Annealing reduces the amount of phase boundaries where fluxlines could be caught and so increases the critical field Bc1 that is described in the publication above.

3.5 Future solutions and possible problems

It might be possible to use other superconductors with a higher critical field Bc1 than niobium, if it is a type 1 superconductor to get even closer to the penning trap. However one has to consider that the reflected magnetic field could influence the field in the area where the antihydrogen is formed and therefore disturb the antihydrogen production.

The antihydrogen particles have to get over the slightly compressed field in front of the Meissner tube. Here is a short range where the particles are deflected a bit to the side. Though in simulations the particle beam enters the meissner tube in an angle that is sufficient for a gravity measurement, there might be even a better way to solve this problem.

One could mount a meissner tube that is not in the meissner phase between the penning trap electrodes and the penning trap magnet. When the penning trap magnet produces its nominal field the meissner tube is brought into the meissner phase. If the critical field Bc1 of the meissner tube is large enough it will lock the magnetic field of the penning trap magnet, without loosing its superconductivity and streamline it as described in the publication. The
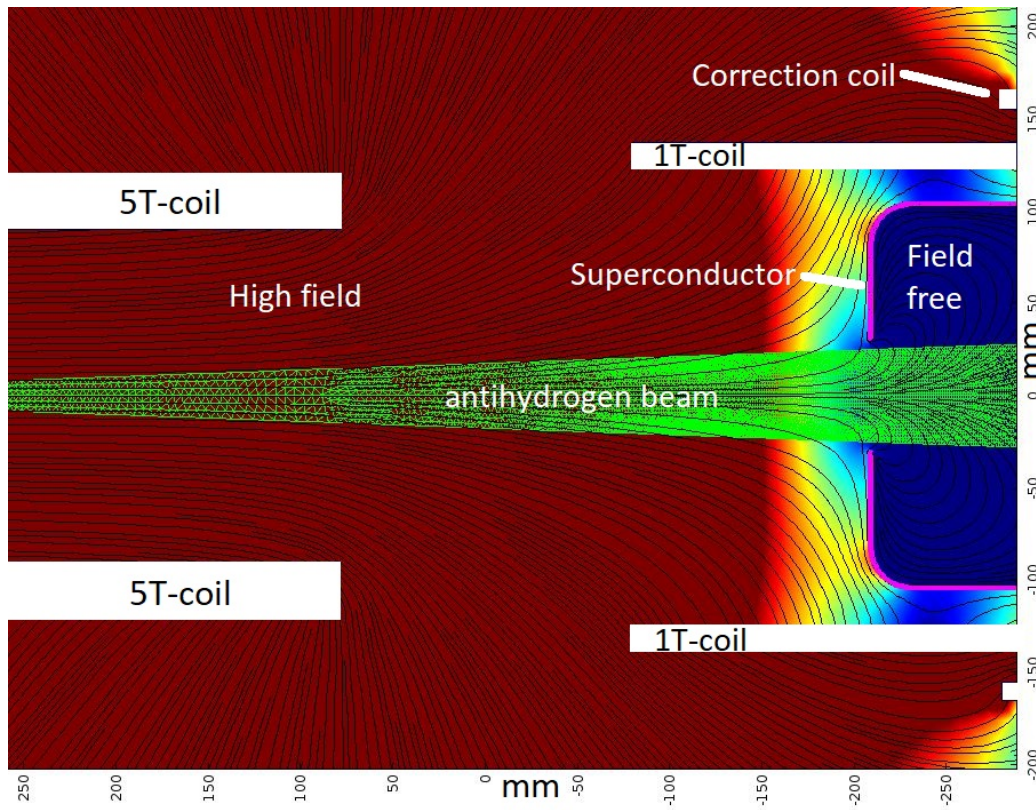
Figure 3.1: A close image of the central region of the aegis apparatus. White are the superconducting coils of the 1 T and 5 T magnets. The superconducting tube with a curved front edge is magenta. The green antihydrogen beam demonstrates the opening angle of the tube for antihydrogen to enter the meissner tube. The field strength goes from under 1 mT (dark Blue) to higher than 100 mT (dark red). As Bc1 of pure (R.R.R=300) niobium is around 130 mT, the other 30 mT are used as a safety margin.

perfectly streamlined field would not deflect anti hydrogen atoms in a radial direction. therefore the area between the penning trap and the Interferometer would no longer be of any concern. But to realize this it is necessary to have a superconducting material that has a critical field Bc1 that is high enough to trap particles in a penning trap, which is in the case of AEGIS at least 1 T.

Further the Meissner tube must not have any openings beside the front and rear opening. So all connection, including eventual laser access and cables to the electrodes and the interferometer stepper motors would need to work in a cryogenic environment which is especially for piezo stepper motors a problem.

37

Of course none of these devices should have a magnetic field otherwise the whole Meissner tube concept would be useless. And the cooling process would need to be done slowly from one side of the tube to the other side to have a slow moving T_c region so that all fluxlines in the material can be pushed out.

Chapter 4

Construction of a digital linear Paul trap for Laser cooling of C_2^-

The Borealis experiment, named after the Aurora Borealis, was founded to explore if laser cooling of the molecular anion species C_2^- is possible. The ultimate goal of the Borealis experiment is to use the laser cooled anions for sympathetic cooling of antiprotons as described in the introduction. This chapter will explain the technical details and the design process of the Borealis experiment in detail to help understand why every step of the development process in this thesis was necessary. The focus will be on the beam bender 4.6, the deceleration 4.7 of the anions and the particle trapping 4.8 that were part of this thesis. The particle production 4.2 and acceleration 4.3, as well as the mass filtering in the Wien filter 4.5, have already been handled in another thesis about the Borealis experiment[14], so they are only described shortly. The order of the description of the devices is according to their place in the beam path. The valve that is used for the anion production comes first and the digital Paul trap is the last step in the beam path.

4.1 Borealis setup overview

In this section an overview of the functionality of the Borealis setup is given, as well as several design processes to help guiding through the individual devices used in the setup. Figure 4.2 shows a CAD drawing of the complete Borealis setup. C_2^- is produced by the supersonic expansion valve 4.2 in the upper left corner of the picture among other particles. The anions move towards the acceleration chamber where they are accelerated to $1740\,\mathrm{eV}$.
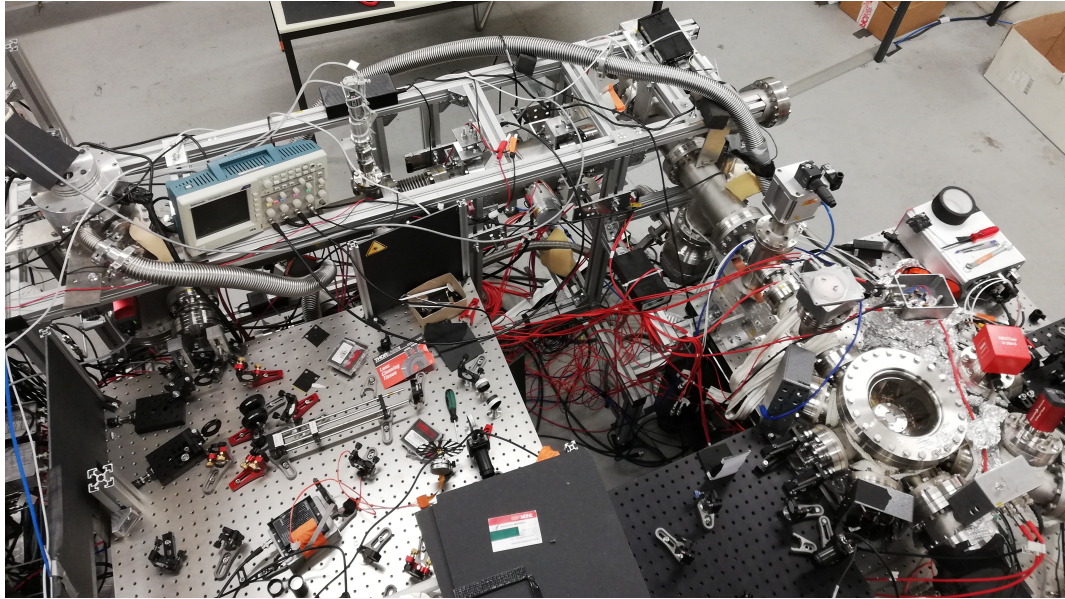
Figure 4.1: The complete Borealis setup with laser table. A detailed description of all parts is found in 4.1 and in figure 4.2.

Several einzellenses 4.4 (El-1 to El-5) help focusing and guiding the beam along the way. The next stage is the mass filter which is a conventional Wien filter 4.5 to get rid of most unwanted masses and all ions. Then the three remaining anion species C_2^-, C_2H^- and H_2CC^- pass a quadrupole beam bender 4.6 in the upper right corner of the drawing to separate the anions from the neutral particles that have passed the mass filter. Finally after another refocusing and resteering of the beam the three anion species pass a deceleration stage 4.7 to have their kinetic energy reduced to under 5 eV so that they can be trapped in the Paul trap in the lower right corner of the drawing. While they are trapped, cavity 2 and cavity 3 in the lower right corner of the drawing will be used to augment the laser cooling that has its origin in the laser setup. Cavity 1 in the upper left corner can be used for a photo detachment spectroscopy [14] if necessary. The first micro channel plate (MCP) detector that is in the beam path is shown here on 2 possible positions and is needed for beam steering and mass spectrums made with the mass filter. The second MCP is mounted on top of the Paul trap to detect the particles that are ejected radially out of the trap after the laser cooling procedure. To have a better overview electrical feedthroughs and cables, as well as optical feedthroughs have been removed from the CAD drawing.
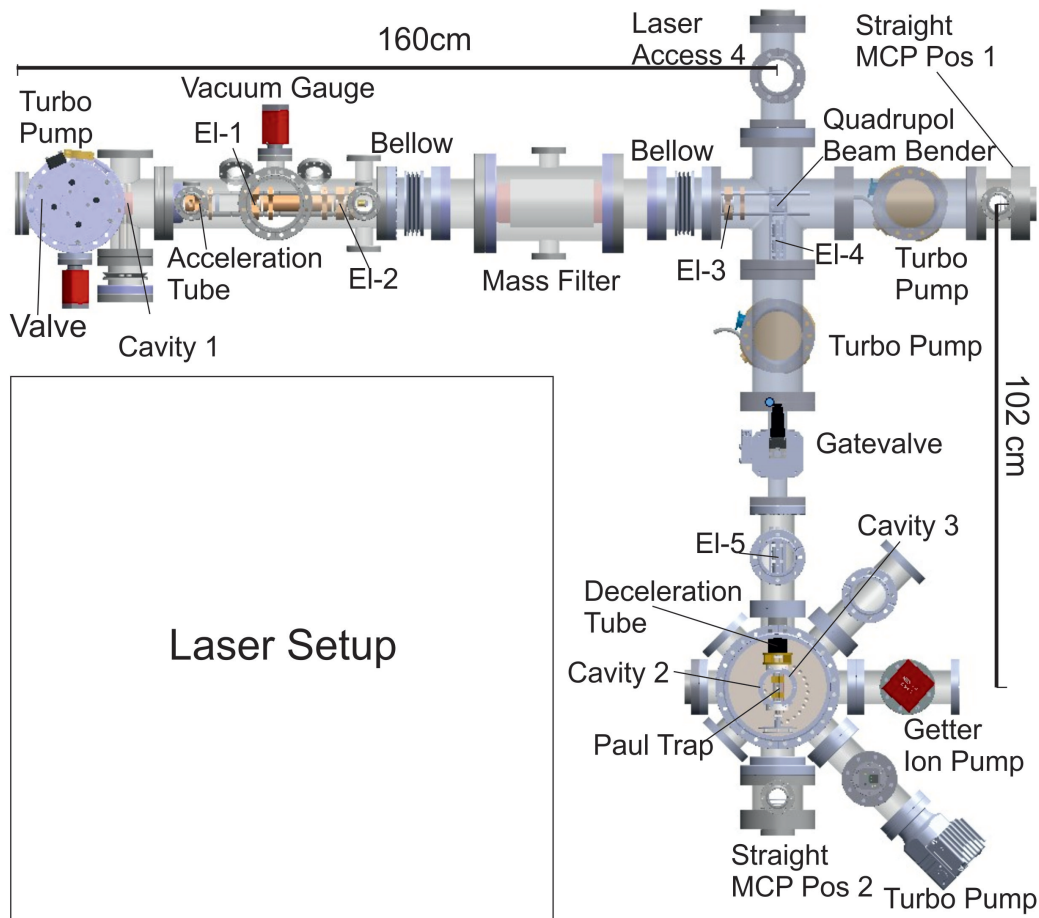
Figure 4.2: This figure shows a CAD drawing of the complete Borealis setup. The exact functions are described in the 4.1. The C_2^- anions are produced in the valve, accelerated, focused and guided by several einzellenses El-1 to El-5, mass filtered by a conventional Wien filter, bend by 90^0 refocused and decelerated. Then the anions are trapped in a digital Paul trap for laser cooling. The overall beam path from the valve to the trap is approximately 262 cm. The laser setup is left blank in this picture, because it was not part of this thesis and also not necessary to describe the goals of this thesis.

4.2 Supersonic expansion valve

The C_2^- pulses were created with a supersonic expansion valve of the type: **Even-Lavie pulsed valve EL-5-3-2011** with a dielectric barrier discharge (DBD) module of the type: **Even-Lavie DBD 12**. Both are operated together by a controller unit that starts and controls the pulse sequence. The complete valve is described in detail in [13].
At first Gas from a gas bottle bought ready to use from **Carbagas** at 40-

41

100 Bar with a combination of 5% C_2H_2 and 3% CO_2 in a He carrier gas goes through a pressure regulator from **Tescom series 44–1100**, that is set on 10 Bar for this gas mixture.

After that the gas mixture goes through a magnetic plunger that is pulled out of an opening by an electromagnet for about $\sim20\,\mu s$ and into the first chamber of the setup that is under a pressure of $\sim$3.3E-6 mBar where it is cooled down by the expansion into vacuum. According to the manufacturer the produced gas jet has a velocity of around $825\,m/s$ and an axial velocity spread of around 200 mK for Neon.

A conical nozzle sits on top of the valve to form the expanding molecules into a beam. The DBD module is described in [13] and provides 30 rapid cycles of high voltage pulses at a 700 kHz rate and with 700 V. Depending on the used gas-mixture up to 1500 V were necessary. These pulses accelerate electrons in the nozzle region that are confined by a magnetic field of a ring shaped permanent magnet made of SmCo.

An additional cathode that was build out of a common halogen light bulb of the type: **Osram halogen Starlight 90 W, 12 V** was used to neutralize the beam and stabilize the discharge of the DBD module. To accelerate the electrons from the cathode towards the valve the cathode is charged to -200 V by a **CAEN SY 2527** using a **CAEN A1821N** board and is heated with 3.5 A, using a **TTI PL303QMD-P** power supply. The CAEN is described more detailed in 4.9.

As for the pressure of the gas side of $\sim 10\,Bar$ there is continuously leaking gas through the magnetic plunger into the valve chamber which made it impossible to use the valve at a higher frequency than 10 Hz or the pressure in the first chamber would become too high. This would damage the DBD and pollute the valve. The used 400 l/s turbopump of the type **Oerlikon Leybold Turbovac TMP 361** could not reach lower pressures during operation.

4.3   Acceleration chamber

Though it would be easier to trap particles directly from the valve when they have a low kinetic energy direcly after the skimmer, there are some problems that were difficult to overcome as well as advantages that come from a particle acceleration.

First is the use of the Borealis experiment in the Aegis experiment. There are strong magnetic stray fields next to the Aegis apparatus which make it very difficult to operate with low energy particles.

Second is that the acceleration also separates the negative charges from the
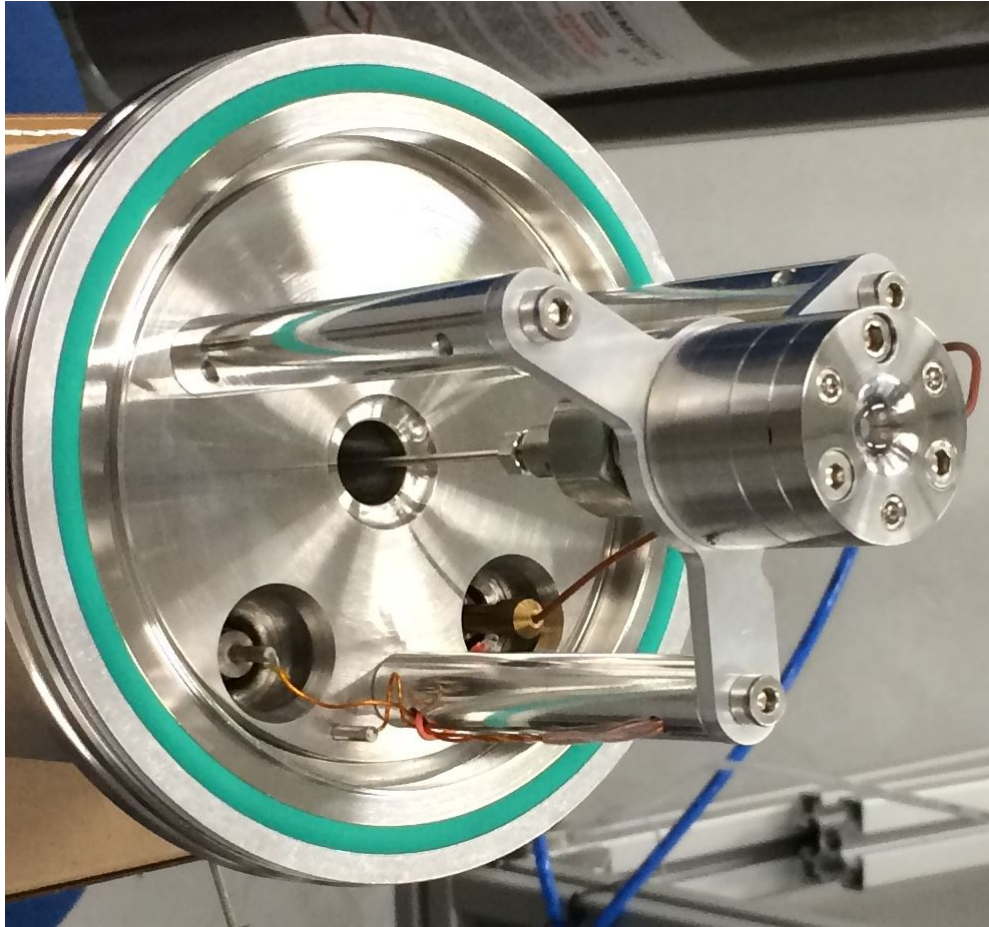
Figure 4.3: The used Even-Lavie valve [13] consists of an Even-Lavie pulsed valve EL-5-3-2011 on the left side of the image and a DBD Module of the Type Even-Lavie DBD 12 on the right side. A magnetic plunger is pulled back for $\sim 20\,\mu s$ by an electromagnet to create a gas pulse. The gas expands through the valve to a conical nozzle that forms the beam. Around the nozzle is a ring shaped electrode that provides the dielectric barrier discharge.

positive and the neutral ones. By doing this the measurements get easier. The third advantage is that the used MCP **F2223-21P379** from **Hamamatsu** detector is not specifically designed for anions and so is likely less efficient for them. To overcome this, for several measurements higher kinetic energies are preferable.

The forth advantage is that the used mass filter and the used beam bender both do not work very well with low energy particles. And without the mass

filter the Paul trap 4.8 would trap higher masses as well, and without the Beam bender the Paul trap would need to be mounted in front of the valve. That would lead to neutral particles flooding the Paul trap during the trapping operations.

The acceleration chamber houses the acceleration stack which has an overall length of 350 mm from the beginning of the acceleration electrode to the end of the second einzellens El-2.

The acceleration chamber itself starts 50 mm before the acceleration stack with a conical aperture called skimmer to establish a pressure drop between the first and second chamber and to collimate the beam coming from the valve. It is a device with sharp edges around a 3 mm hole to prevent a turbulence in the anion cloud from the valve.

After leaving the skimmer the anions reach an acceleration electrode which is 40 mm long and has a 30 mm inner diameter. On both ends of the acceleration electrode are Gold meshes with a line width of 19 μm and opening width of 344 μm, which means an opening fraction of 90 %. When the C_2^- anions are inside the acceleration tube, it is ramped up to -1740 V by a fast push-pull switch within several μs [14]. The anions, that are now surrounded by a closed faraday cage are not affected by fields outside of the acceleration tube. When they leave the acceleration electrode and see the grounded electrode directly after it, which also has a gold meshs inserted they are accelerated towards it. Through the meshes the field is homogenous enough to have a considerable amount of the anions accelerated parallel to the beam path towards it. Still an iris directly after the grounded mesh was necessary to have the sideways deflected particles removed from the beam as they might influence the measurements. After the iris the anions pass a shielded area that was necessary because of the high voltage cables to the einzellenses electrodes. After that the particles are collimated and steered by two einzellenses that are described more detailed in 4.4.

The push-pull switch is a **Behlke HTS 31-03-GSM** and is used in this experiment for voltage ramps up to -1800 V. As the acceleration is in the kV range the total particle energy can be aproximated by $E_{kin} \sim U_{acc}$.

Simulations of the field dynamics in the acceleration stacks and the einzellens systems can be found in [14].

4.4 Einzellenses

The Borealis setup uses 5 segmented einzellens systems on various areas to help focusing, collimating and steering the beam. An einzellens, or unipotential lens is an electrostatic lens to focus a charged particle beam without
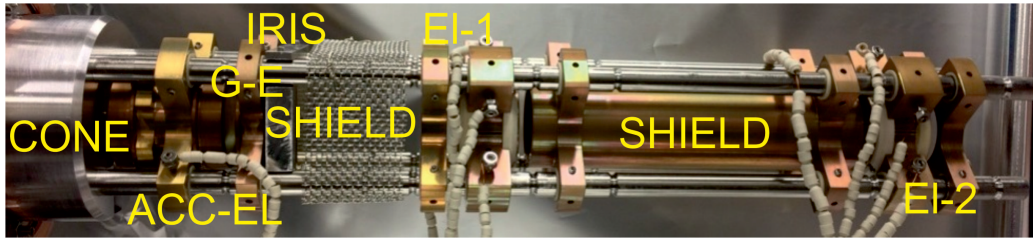
Figure 4.4: The acceleration stack consists, from left to right, of a conical aperture (CONE) to establish a pressure drop and to collimate the beam from the valve, an acceleration electrode (ACC-EL) on the left side of the image that is connected to a Belkhe switch. Then a grounded ring Electrode (G-E) with an iris directly after it. Then comes a grounded shield (SHIELD). After the first shield the anions pass 2 segmented einzellenses (El-1,El-2) and another shield in between, for focusing collimating and steering of the beam. The acceleration electrode and the first grounded ring electrode have gold meshes to create homogeneous fields. Not visible on this picture is a second iris after the second einzelleins that is build in now.

changing its energy. The positions of the einzellenses can be seen in 4.2. The first 2 einzellenses are directly after the acceleration stack to get a beam that is axially parallel to the center axis of the mass filter. After the mass filter is another einzellens to redirect the beam from the mass filter and send it to the beam bender. Directly after the beam bender is the forth einzellens to help refocusing the beam that's spread up by the beam bender. The last einzellens is directly in front of the deceleration stage to collimate the beam before sending it through the deceleration tube 4.7.

Because of machining errors it was necessary to use segmented einzellenses. The segmented einzellenses have the ability of not only collimating and focusing the beam but also bend it to the side to a certain degree. By doing this the collimation gets worse but good compromises between focus, collimation and direction could be found. The exact field dynamic of the used segmented einzellenses are discussed in [14]. In addition to the einzellenses, 4 deflection electrodes aranged in a square around the beam were tested between El-4 and El-5. But in the end they were found unnecessary as the used einzellenses were sufficient to direct the beam straight to the Paul trap.

4.5 Mass filter

A mass filter was necessary to get rid of other masses than C_2^- which makes only around 5 % of the produced anions according to the carried out mea-
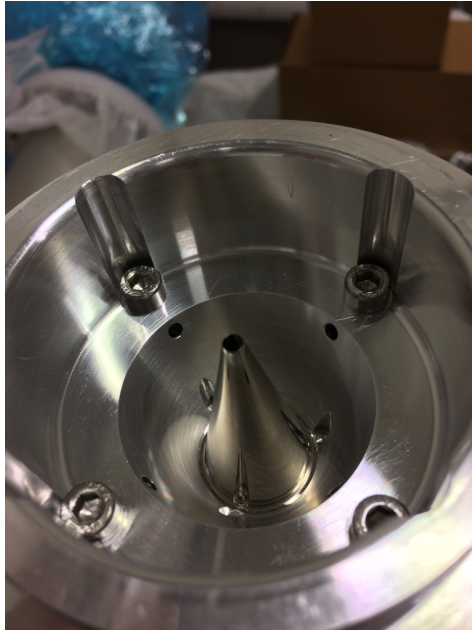
(a) Skimmer
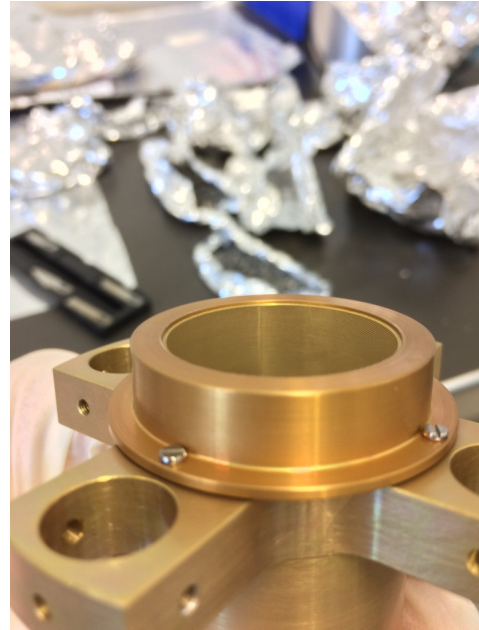
(b) Acceleration electrode

Figure 4.5: **a** The conical skimmer sits in the center of the image. The particle beam from above is split into a small but collimated part that goes through the hole and a large part that is deflected to the sides of the simmer. **b** The acceleration electrode with gold mesh and mesh holder on top. The electrode is $3\,\mathrm{cm}$ in diameter.

surements in [14]. This is necessary as Penning traps used in the Aegis experiment do not filter masses. Further it was necessary to see if the expected C_2^- is actually produced or not. And though Paul traps can be used as mass filters, they are able to hold a range of masses when they are used in their normal trapping operation mode 4.8.

It turned out that the super sonic expansion valve produces a wide range of masses, that were found with mass spectrum scans [14]4.8.

Originally a cheaper solution was planned that consisted of 2 magnetic plates that held a certain constant magnetic field in between them, and a curved vacuum tube to bend the correct mass 24 of C_2^- through the curved tube by the Lorenz force $\vec{F} = q(\vec{E} + \vec{v} \times \vec{B})$ and to get rid of all other masses. The Magnet was build for a kinetic particle energy of $100\,\mathrm{eV}$ because it was not possible to get a stronger permanent magnet for this purpose.

After many failed attempts a Wien-filter or "velocity filter" of the type **Beam Imaging Solutions Inc., model 600–H**, with a nominal resolution of $\frac{m}{\Delta m} = 400$ was ordered. The device consists of copper coils, that produce
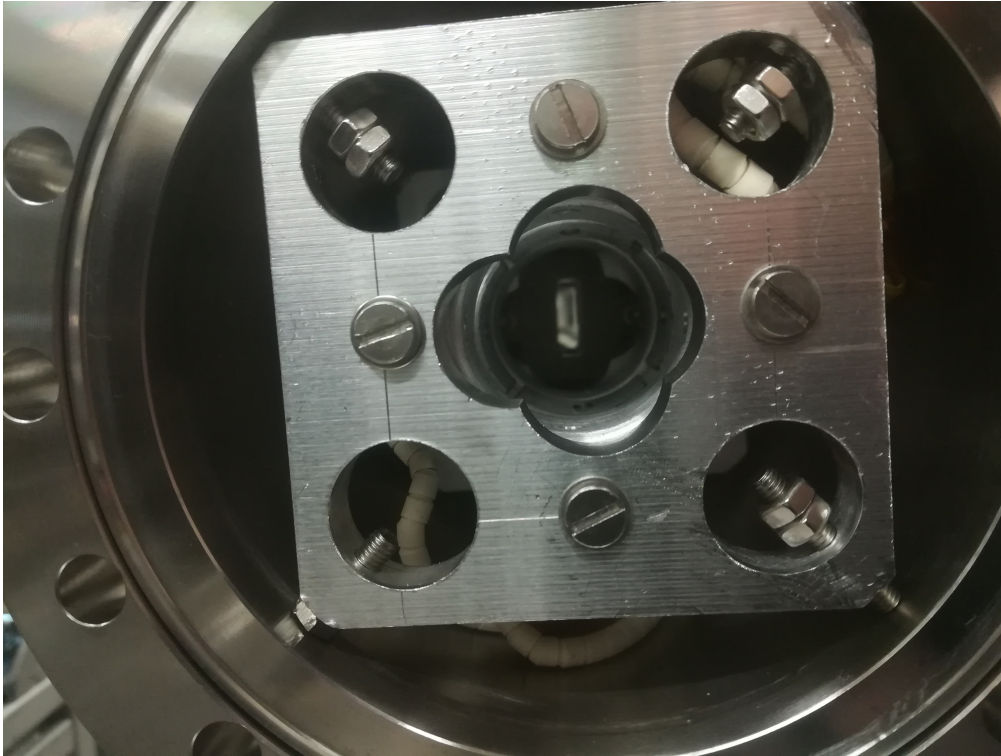
Figure 4.6: This figure shows einzellens 4 (El-4) directly after the beam bender. The small slit in the center is the outlet of the beam bender. El-4 as well as El-5 were self manufactured due to the long delivery periods and high costs of precision workshops.

a magnetic field on an axis normal to the particle beam and electrodes, to create an electric field normal to the particle beam and the magnetic field. By doing this one can separate the masses into different flight paths and so single out the correct mass as setting the device in a way that the wished mass is the only one that goes straight through it. Further the device has additional electrodes to reduce fringe fields and to correct a nonparallel beam. The used model however had the problem that the mass filter was not well aligned with the vacuum vessel it was mounted in by an angle of around $\sim 2^0$. First it was tried to overcome this problem by bending the beam with the first two einzellenses to guide it straight through the mass filter. This lead to a large particle loss. Later so called bellows were organized as shown in 4.2. Unfortunately this mass filter was not able to reach the wished 1 mu solution to separate the measured masses C_2^-, H_2CC^- and C_2H^- when staying within the safety parameters of the device. To use it out of the safety parameters, cooldown times for the magnet had to be implemented into the

47
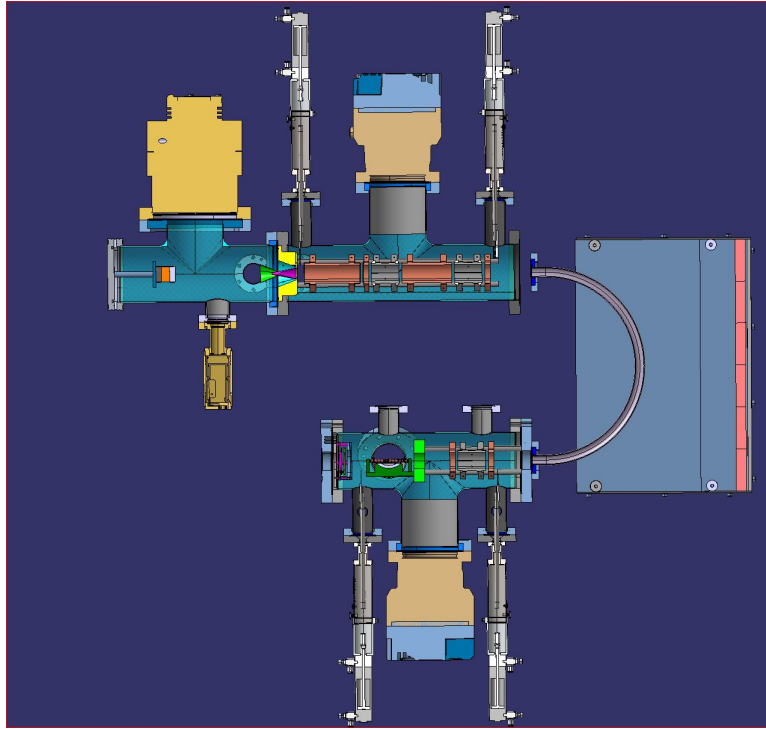
Figure 4.7: The original design for the Borealis setup used a permanent magnet on the right side of the picture to deflect the correct masses into the chamber in the lower part of the picture. The Borealis Penning and Paul traps were originally designed to be mounted after the vacuum chamber in the bottom-center part of the picture. The chambers in the upper left and upper center part of the picture are used in the actual Borealis setup as production chamber and acceleration chamber 4.2, 4.3.

software so that the magnet was only powered up during the measurement which takes around 1 second. After that cool down periods of up to $20\,\mathrm{s}$ were implemented to prevent any damage. By doing this C_2^- could be detected for the first time at the Borealis experiment [14].

However the trapping in the Paul trap and first laser cooling attempts can still be done with not only C_2^-,but H_2CC^- and C_2H^- still in the Paul trap. So the mass filter is now used within its safe parameter range and the following mass spectrum was measured directly in front of the Paul trap after bending the beam around with the beam bender, between einzellens 5 and the deceleration stage to make sure that only the expected masses are inside of the trap.

The following table holds the masses that could theoretically appear by using a gas mixture that contains C_2H_2,CO_2 and a He or Ne carrier gas:

48
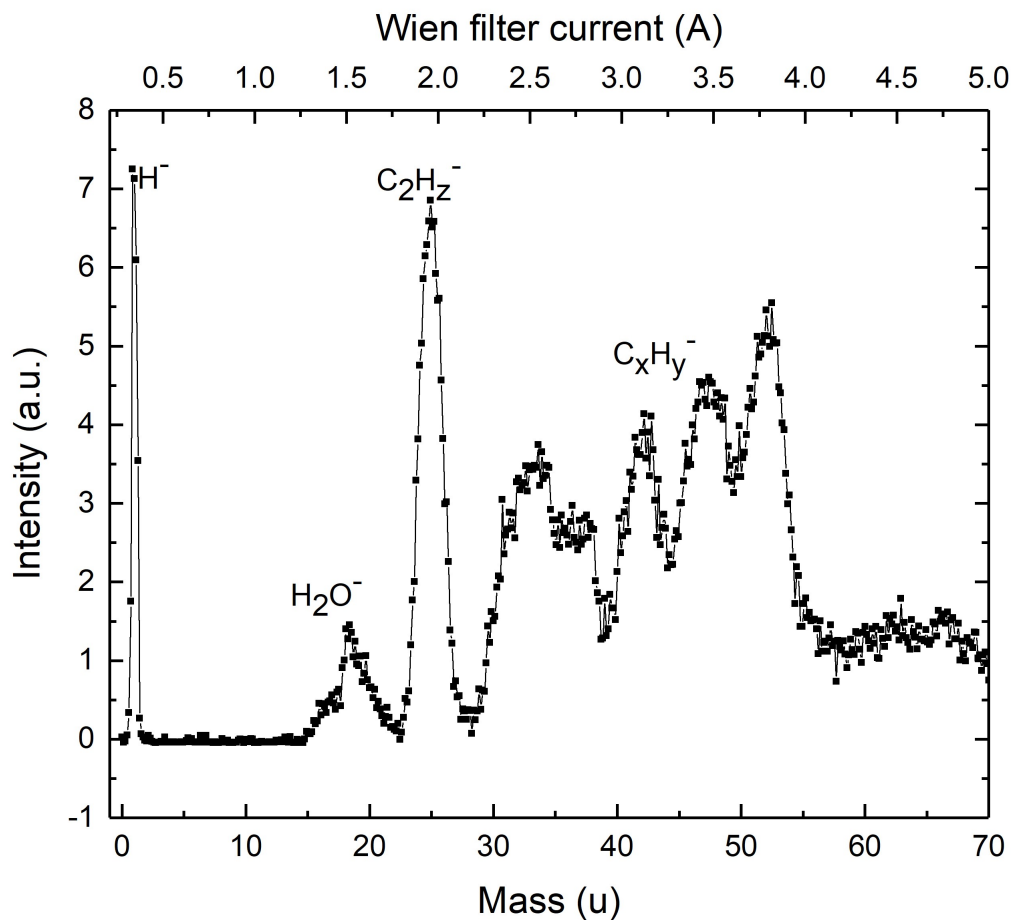
Figure 4.8: The Mass filter is calibrated on the peak at mass 24. So C_2H_z consists of C_2^-, H_2CC^- and C_2H^-. For the other peaks the masses cannot be identified unequivocally because it is not sure that the masses rise linear with the used current. The spectrum was measured at the position directly after El-5 4.2, and therefore directly before the deceleration stage 4.7.

4.6 Beam bender

The implementation of a system to give the beam an angle without loosing particles was necessary to separate the anion beam from the neutral particles. If the Paul-, or Penning trap would have been build in directly after the mass filter, the accelerated anions would reach the trap first and would get trapped. But after that an avalanche of neutral particles that have not been accelerated but would still travel at $825 \frac{m}{s}$ towards the trap 4.2. These particles would hit the trapped plasma and disturb a laser cooling process

49

Species	EA (eV)	Reference
CO_2^-	-0.6	(Knapp et al., 1986)
O_2^-	0.45	(K. M. Ervin et al., 2003)
CO^-	1.26	(Rafaey and Franklin, 1976)
$C_2H_2^-$	unstable	(Dressler and Allan, 1987)
H_2CC^-	0.484	(DeVine et al., 2018; Gerardi et al., 2010)
C_2H^-	2.97	(Zhou et al., 2007)
C_2^-	3.27	(M. K. Ervin and Lineberger, 1991)
Ne^-	-1.2	(Bratsch and Lagowski, 1986)
$F-$	3.40	(Blondel et al., 2001)
H_2O^-	$< 10^{-4}$	(Chipman, 1978)
HO^-	1.83	(Smith et al., 1997)
O^-	1.46	(Blondel et al., 2005)
CH_4^-	?	probably unstable
CH_3^-	0.08	(Ellison et al., 1978)
CH_2^-	0.65	(Leopold et al., 1985)
CH^-	1.24	(Kasdan et al., 1975)
C^-	1.26	(Bresteau et al., 2016)
He^-	-0.5	(Bratsch and Lagowski, 1986)
H_2^-	unstable	(Heber et al., 2006)
H^-	0.75	(Lykke et al., 1991)

Figure 4.9: A list of possibly produced anions based on combination of the gas mixture constituents. The stable anions have positive electron affinities. The table is taken from [14]

with particle collisions. A conventional quadrupol beam bender was designed to overcome this problem.

The tasks for the beam bender where to build it as small as possible because it had to fit onto the 4 rods in the acceleration chamber before the acceleration stack. The reason for this was that the Paul trap should have been used without a mass filter and without acceleration at first.

The beam bender consists of 4 main rods with a hyperbolic surface on the inner side designed after a NASA system [16]. The beam bender has 2 possible outlets on the sides with 4 correction electrodes each to steer the beam after the deflection as well as the possibility to go straight through. The Beam Bender was made of 316L stainless steel and the spacers were made of Macor.
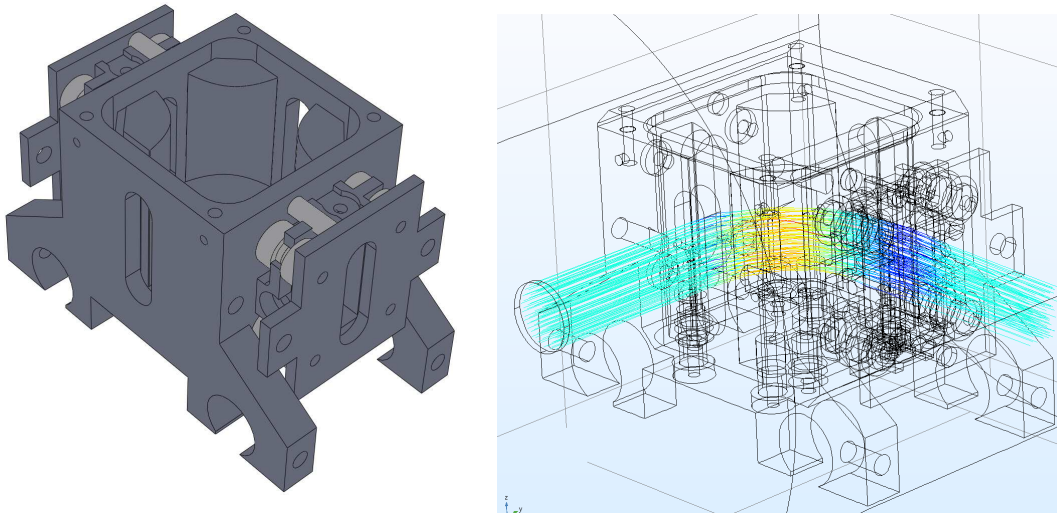
Figure 4.10: **On the left picture:** The beam bender has an overall length of 36 mm in length and the square inner chamber that contains the hyperbolic electrodes has a diameter of 30 mm. From side to side, including the four correction electrodes on each side the beam bender measures 56 mm.
On the right Picture: The beam bender with particle beam simulated in the simulation software Comsol 5.2. Because of machining errors on the electrodes, the space charge and the small size of the beam bender, the beam had to have at least 600 eV to get well focused and collimated after being bend.

4.6.1 Beam Bender as enhancement for the mass filter

When the Wien-filter deemed to have difficulties to separate the three masses 24,25 and 26 without going over the limitations from the manual, it was tried to use the spread of the outlet of the beam bender to increase the different angles between the flight paths of the different masses. This was partly successful when the four hyperbolic electrodes were not set on equal positive and negative voltages but, but only on a negative voltage while the electrodes that are usually positive were grounded. By doing this a potential hill was created in the center of the beam bender of the size $V_{neg}/2$. Then the horizontal correction electrodes Corr 2 on the Beam entrance side and Corr 4 on the opposite side were used to measure a mass spectrum out of the three masses remaining in the beam after the Wien filter. Due to time reasons this project was not continued and could therefore not be verified, but it would be certainly of interest for the Borealis group if it becomes necessary to have

only C_2^- with mass 24 in the Paul trap.

4.7 Deceleration stage

After it was necessary to accelerate the beam due to the reasons mentioned above 4.3, it is of course necessary to decelerate the anions again to trap them in a Paul trap that has a trap depth of $\sim 22\,\text{eV}$.

To reach this goal a deceleration stage was created based on an electric potential hill that reduces the kinetic energy of the arriving anions. The idea here is to insulate the whole Paul trap and all of the devices in the vacuum chamber from the grounded vacuum chamber and use a transformer with a separated ground to run all electronic devices that have connection to the Paul trap systems on the same separated ground as the trap 4.9.

4.7.1 Development and design process of the deceleration stage

The main problem of reducing the kinetic energy from $1740\,\text{eV}$ down to under $5\,\text{eV}$ was to do this without a massive particle loss, coming from the radial kinetic energy of the particles that has proven far more difficult than expected. The radial kinetic energy of the anions comes from a beam that is not well adjusted, a deceleration stage that is not perfectly aligned with the paul trap, the spacecharge that has a far higher impact on the anion bunch after the deceleration when all anions are bunched together and deflections coming from in-homogeneous electric fields.

So several iterations were necessary to fully understand the specific problems of this construction and the main reasons of the particle losses that led to the final design.

First Iteration of the deceleration stage

Due to cost reasons the first development was quite simple and consisted of 2 opposing gold meshes comparable to the acceleration stage 4.3 when it is ramped to -1740 V. The first iteration was not successful due to several reasons. At first it had a disadvantageous ratio of the distance between the two gold meshes and the surrounding ground and so the homogeneity of the field was reduced. Second were the steel holders that had a height of about a millimeter. Despite the chamfer around the beam path on both steel holders, this created an effect like an einzellens that strongly focused the beam. But
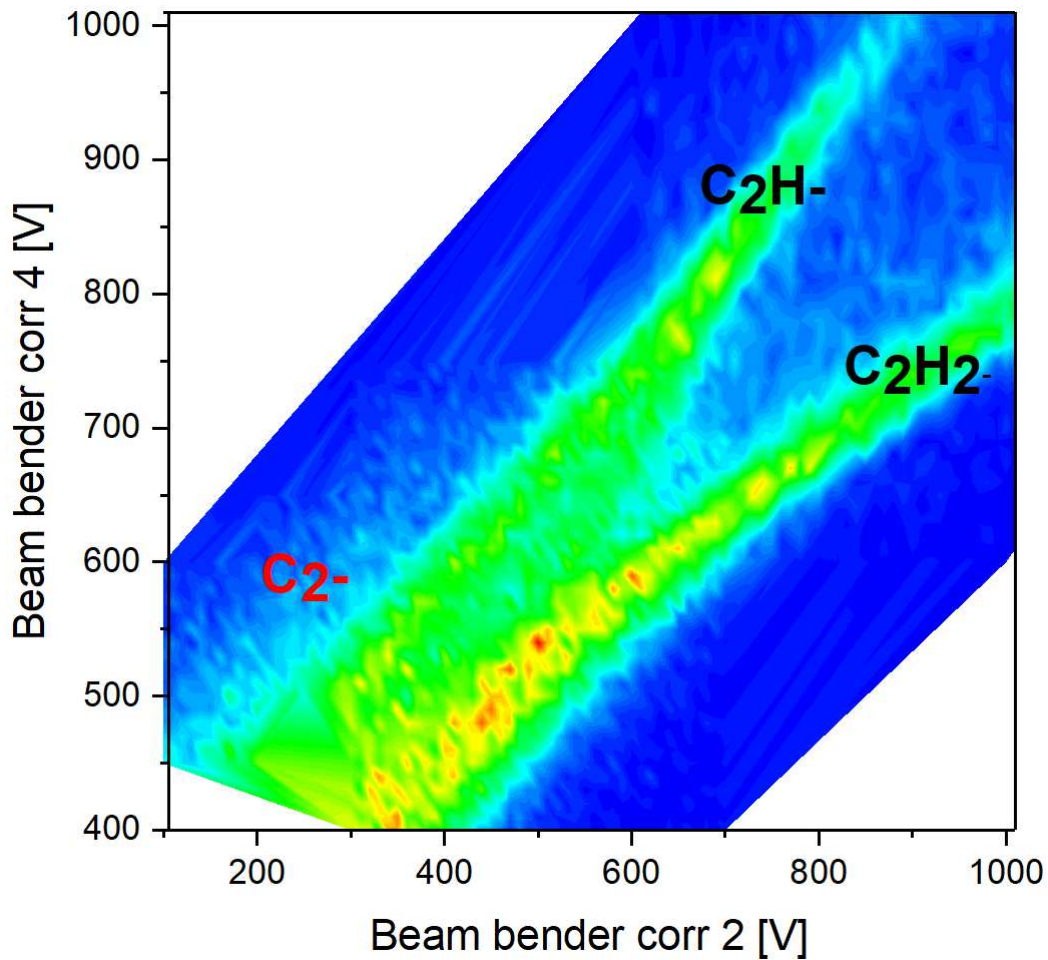
Figure 4.11: The beam bender was used in a configuration where the hyperbolic quadrupol electrodes were used with negative Voltage and ground instead of equal negative and positive voltages as usual. By doing this it was possible to do a measurement with the help of the horizontal correction electrodes corr 2 and corr 4 and see two strong signals that were likely $C_2H_2^-$ and C_2H^-. Further there is a weak signal on the C_2H^- side that could be C_2^- which is expected to to be weaker. The small amount of C_2^- is verified by [14]
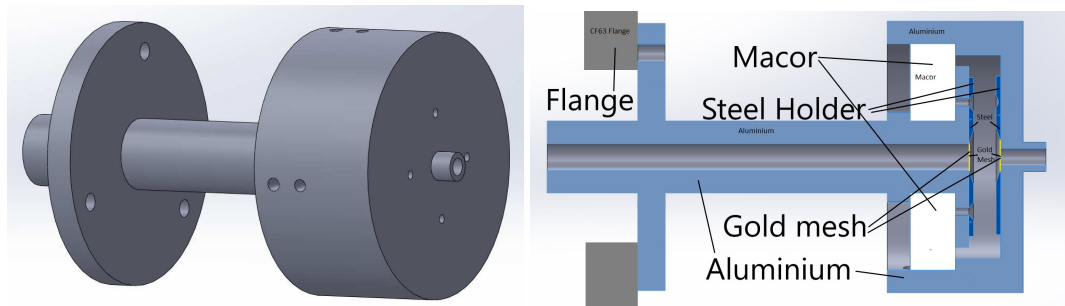
Figure 4.12: The first iteration of a resistive tube consisted of of an aluminum tube with an aluminum cap that is separated by two half macor rings. On the inside, over the openings of the beam path, two steel holders hold 2 goldmeshes to produce a homogenous field.

unlike an einzellens the beam was not refocused after focusing because after the gold mesh the anions were in a homogenous field. This lead to a particle loss on the walls of the endcap.

Second Iteration of the deceleration stage

The idea of the second iteration was to have a longer deceleration stage to reduce the impact of the spacecharge and to have electric conductors around the electric field with a field strength that matches the strength of the straight field from front end to back end of the deceleration stage. To have a homogeneous rise of the negative voltage towards the Paul trap the electrodes of the stack were connected by resistors with a high resistance to reduce the current to a minimum, without loosing the connection. Like iteration 1 this iteration was mounted on a CF"63 flange to have a certain stability.

For cost reasons the stack consisted of CF"16 copper gaskets that are held together by teflon discs. This design was inexpensive but it was not possible to align the electrodes straight and the inaccuracies deflected the anions to the side. Nevertheless it was better than the first iteration as it was possible to reduce the kinetic energy down to $600\,\mathrm{eV}$. The einzellens effect that was a problem in the first iteration was not solved with this iteration either.

Third Iteration of the deceleration stage

The third iteration is a copy of the second iteration but with parts that were manufactured in a professional workshop. With the accurately machined parts and with more electrodes it was possible to reach kinetic energies of
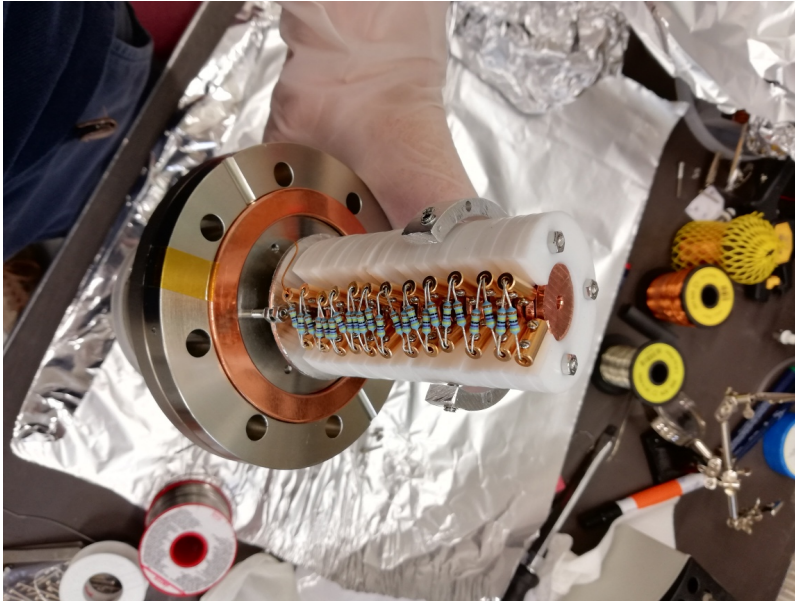
Figure 4.13: Iteration two of the deceleration stack consisted of a row of electrodes connected by resistors to create a more homogeneous electric field as it is not surrounded by ground but by charged electrodes that have about the same charge as the field within them.

under 200 eV. Through the developement of this design the problem of the focusing effect at the ends of the deceleration stacks became visible and enabled further improvements of the deceleration stage. In COMSOL simulations the first and third design seemed to work as in the simulations a perfectly aligned particle beam was simulated.

Fourth Iteration of the deceleration stage

The fourth iteration of the deceleration stage was developed to reduce the field inhomogeneity along the deceleration stage to almost zero. A glass tube **RGP T 41.4-30.7/90** from **Photonis** is used with a coating of $\sim 30 M\Omega$ to create a field gradient that goes along the beam axis but not in a radial direction. With the help of this tube the only disturbances inside the deceleration stage came from the endcaps. Several simulations were performed with Comsol to simulate the glass tube and the impact of the end caps mounted to it. Various Mesh holders were simulated and the simulation has shown that an end cap that is completely flat on the side towards the center of the glass tube is the only suitable solution.

The simulations were performed with a Voltage of -1800 V as the acceleration
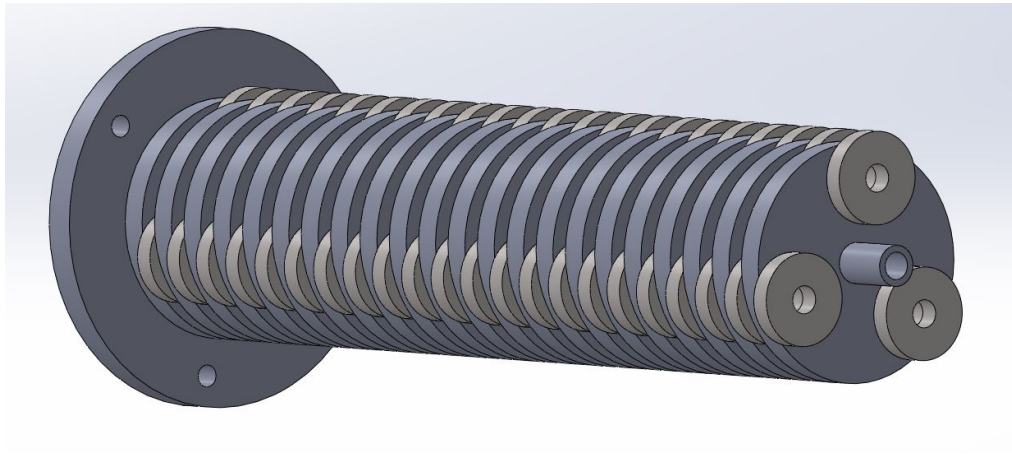
Figure 4.14: Iteration three of the deceleration stack is a development of the second iteration and build by a professional workshop.

stage 4.3 was set to -1800 V. It turned out later that the acceleration switch had an internal voltage drop of around 60 V and could therefore only create anion beams with ∼1740 eV. The first design with the glass tube still held
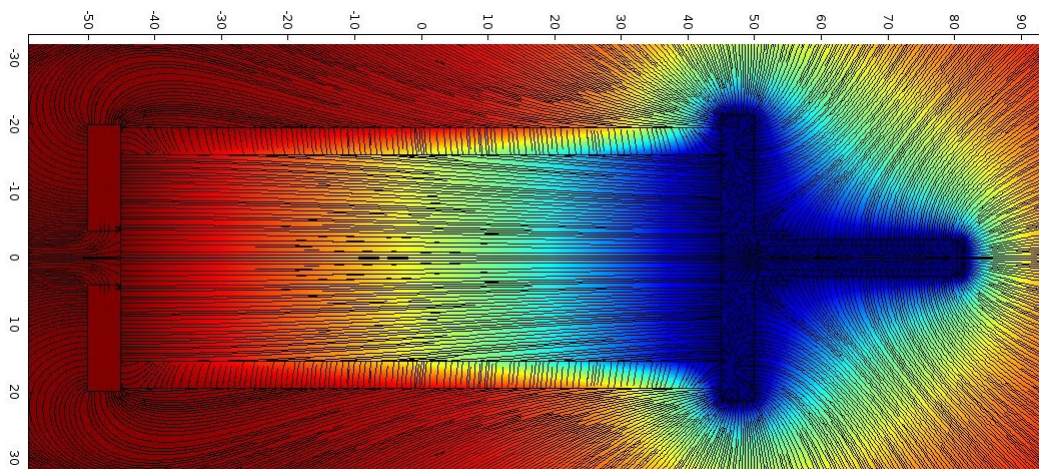
Figure 4.15: The electric field lines and strengths of the fourth iteration of the deceleration stage. The used glass tube has an overall length of 9 cm and an inner diameter is 3.7 cm. The part that is mounted on the CF"63 flange and therefore connected to ground is dark red and the HV part is Dark blue for -1800 V. The endcaps of the Paul Trap are set to -1800 V to show the floated Paul trap entrance. One can see the field lines in the center that are parallel to the center axis.

the same mesh holders that were used in the first iteration 4.12, to see if the

impact is really that disturbing. After the disturbance of the mesh holders where confirmed, the endcaps were redesigned.

Using this, energies of under 10 eV were possible, but it was not considered sufficient as it was not known that the particles actually had an energy of only 1740 eV instead of 1800 eV. So further design changes were made to improve the deceleration stage.
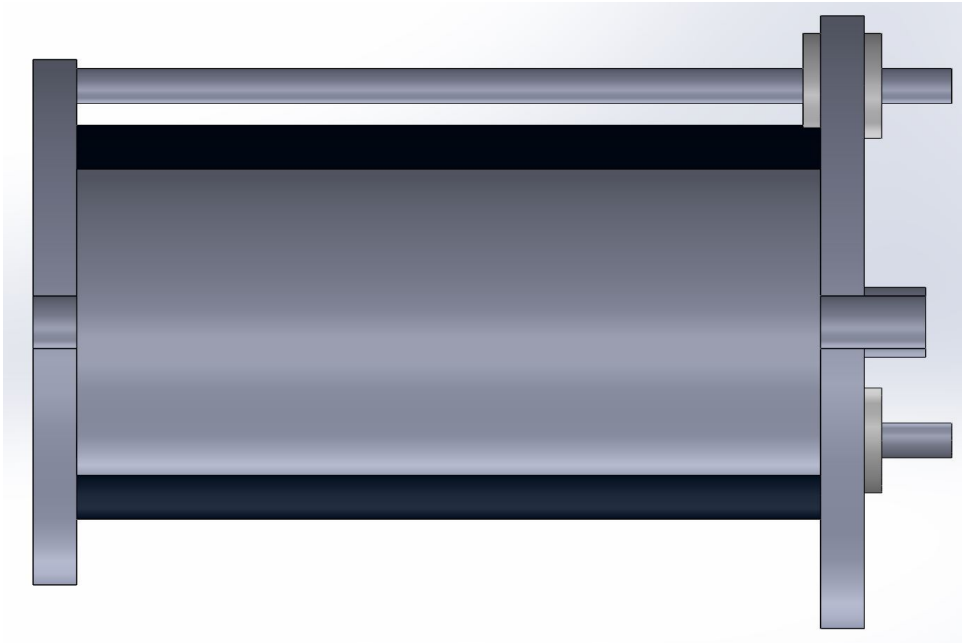
Figure 4.16: The forth iteration uses a glass tube **RGP T 41.4-30.7/90** from **Photonis** that is coated with a high resistive coating on the inside to create a homogeneous field. Not in the picture are the gold mesh and the gold mesh holders that looked like in the first iteration.

Final Iteration of the deceleration stage

The last iteration was made to improve the parallelism between the center axis of the Paul trap and the center axis of the deceleration stage.

To enable this the deceleration stage was now mounted directly onto the Paul trap. Therefore two new end caps were manufactured and implemented.

With this improvement it was not possible to reach higher kinetic energies as for the before mentioned reasons but it was possible to load more anions into the trap. The voltage drop in the acceleration stage was still not known at this time and so the Paul trap was further improved as is explained in

the next chapter 4.8. More detailed simulations concerning the deceleration stage can be found in the chapter 2.0.3.
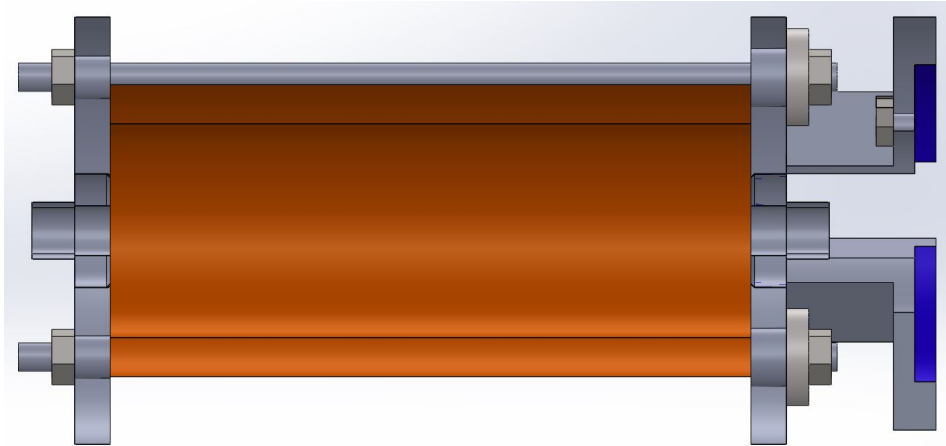
Figure 4.17: The fifth iteration uses the glass tube from iteration four but mounts it directly onto the Paul trap holders. On the inside the fifth iteration looks exactly like the forth.

4.8   Paul trap

The designing, building and commissioning of a particle trap for the Borealis laser cooling experiment was the main goal of this thesis. A digital linear Paul trap was chosen as it has several advantages over the originally suggested Penning trap.

Though the Aegis experiment uses Penning traps to trap antiprotons and a Penning trap would therefore be favorable in terms of results, it requires strong and homogeneous magnetic fields that are usually provided by superconducting solenoids. However the Borealis laboratory has no infrastructure to supply a superconductor and so this solution is not feasible. The original idea of creating a permanent magnet as a solenoid did not work out as it was not possible in a research and development project to design a magnet with the required specifications of $1\,T$ and a maximum field gradient of $>1\,mT$ in the center.

The next advantage over a Penning trap is that the magnetic field inside a Penning trap would lead to Zeeman splitting which would require more lasers for the cooling process [14]. The last advantage is that a Penning trap, if not very well aligned with its electrode stack can heat the plasma inside [14]. For all these Reasons the design of a Paul trap was deemed easier.

Die approbierte gedruckte Originalversion dieser Dissertation ist an der TU Wien Bibliothek verfügbar.
The approved original version of this doctoral thesis is available in print at TU Wien Bibliothek.

TU Bibliothek
Your knowledge hub
WIEN

4.8.1 Paul Trap theory

This paragraph shall give a short overview of the well known Paul trap theory [21],[1] and why several aspects of the Paul trap theory needed to be checked in detail for the full understanding of the trap mechanics and the measured results.

A common linear Paul trap creates a radial electric potential ϕ_{rf} and an axial electric potential ϕ_{end} of the form:

$$\phi_{rf}(x,y,t) = V_{rf}\frac{x^2+y^2}{r_0^2}cos(\Omega_{rf}t), \quad \phi_{end}(x,y,z) = \frac{\mu U_{end}}{z_0^2}[z^2 - \frac{1}{2}(x^2+y^2)] \tag{4.1}$$

with the total potential

$$\phi = \phi_{rf} + \phi_{end} \tag{4.2}$$

. Ω is the RF drive in 2πHz, V_{rf} is the peak to peak voltage of the RF electrodes and V_{end} is the Voltage, set on the end caps. r_0 is the radial distance from the center of the trap to the RF electrodes and z_0 is the axial distance from the center of the trap to the end-caps. The trap has therefore a diameter of $2r_0$ and a length of $2z_0$. The parameter μ is a geometry factor that is usually between 0.2 and 0.3. As it has only a small effect the trap depth a detailed analysis of the geometry was not made.

With the help of a special form of the Hill differential equations known as the Mathieu equations that are described in detail in the Handbook of Mathematical Functions by Abramowitz from 1972, and for the specific case of linear Paul traps in [21] and [1] one can obtain the a- and q- parameters that create the so called a-q-parameter space that is used to find stable parameters for the operation of a Paul trap.

$$a_x = -a_y = \frac{8QU_0}{m\Omega^2 r_0^2}, \quad q_x = -q_y = \frac{2QV_{rf}}{m\Omega^2 r_0^2}, \tag{4.3}$$

These parameters consist of the particle charge Q, the angular frequency $\Omega = F*2*\pi$, the Frequency F, the trap radius r_0, the particle mass m and a possible diagonal offset Voltage U_0, that can be used for mass filtering. In a linear Paul trap they describe the stable radial confinement of charged particles in the trap. In addition to the a-parameter comes the effect of the End caps of the Paul trap that are used for axial confinement described by [20].

$$a_{x-end} = a_{y-end} = -\frac{4\mu U_{end}}{m\Omega^2 z_0^2} \tag{4.4}$$

In the Borealis experiment the electronic setup does not allow a diagonal offset voltage so U_0 is always zero and a_{x-end} would be the only contribution
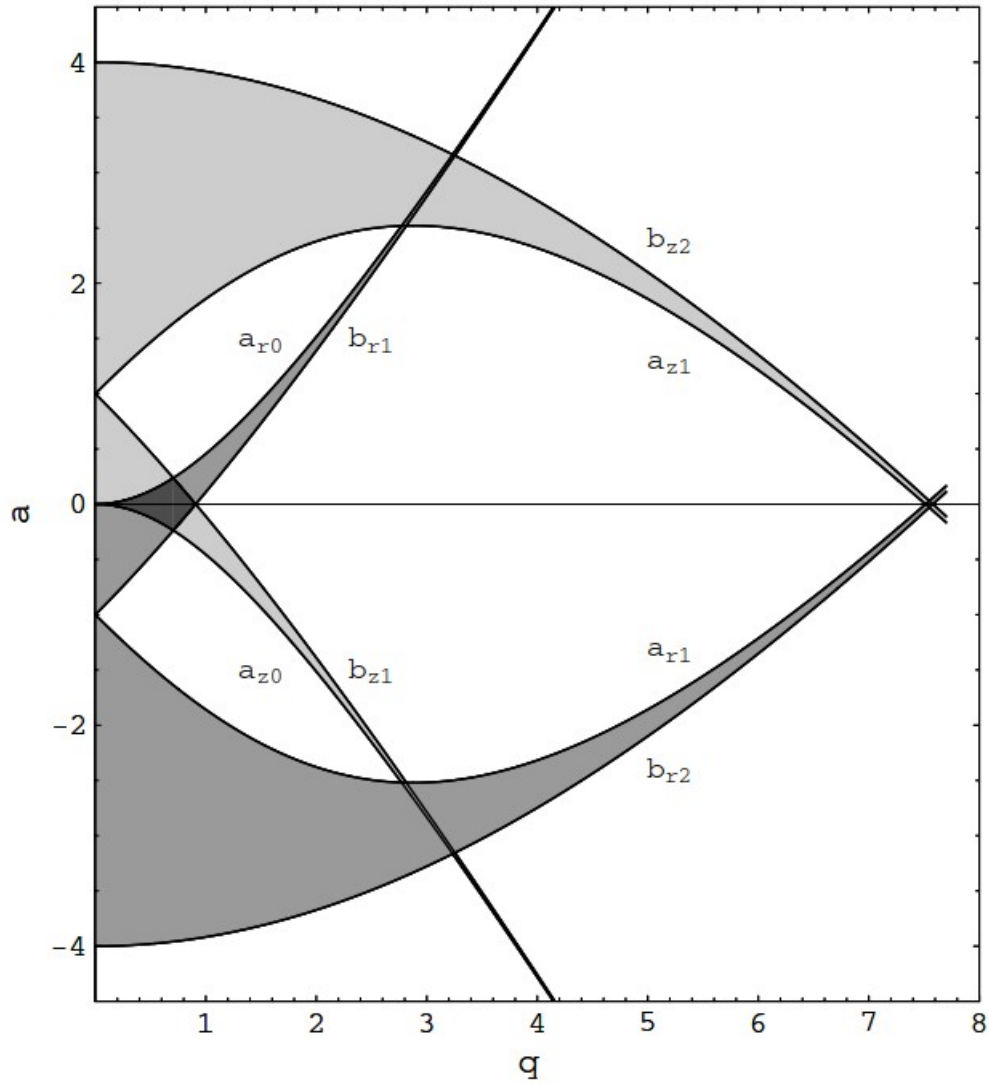
Figure 4.18: The radial stability parameter space of a linear Paul trap: The horizontal axis describes the q-parameter and the vertical axis the a-parameter. dark grey and light grey shaded areas are stable in x and y direction. An overlap of dark and light shaded areas means that the Paul trap runs stable in x and y direction and can therefore confine charged particles radially.
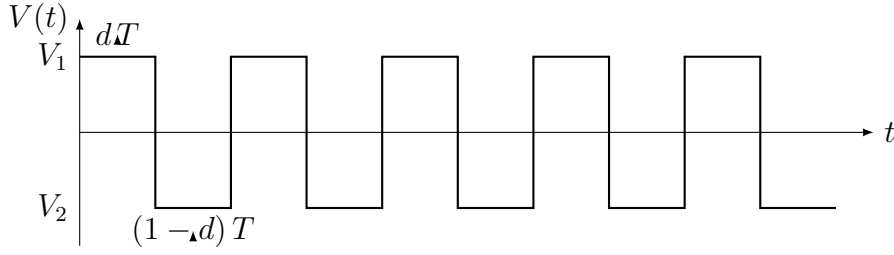
Figure 4.19: The square wave as it is used by the Borealis Paul Trap. The RF Voltages $V_1 = -V_2$ are used as well as a dutycycle of $d = 0.5$

to the a-parameter.

However this is not the case for a digital linear Paul trap. To describe a digital linear Paul trap as the one used by the Borealis experiment there are some small changes necessary to describe a square function of the form:

The most obvious change is to replace $cos(\Omega_{rf}t)$ in the equation 4.3 with $P_t(\tau)$

$$P_t(\tau) = \left\{ \begin{array}{lll} 1 & if & 0 \leq \tau \leq dT \\ -1 & if & dT < \tau < (1-d)T \end{array} \right\} \tag{4.5}$$

A detailed explanation of digital Paul traps in [21] helps understanding the creation of parameters for the a-q-parameter space that are useful for a digital Paul trap. The substitution

$$U_0 = dV_1 + (1-d)V_2, \quad V_{rf} = 2(V_1 - V_2)(1-d)d \tag{4.6}$$

from [21] leads to the parameters that are needed to fully describe the stable regions of a digital linear Paul trap as the used one.

$$a_x = -a_y = \frac{8Qd(V_1 + (1-d)V_2)}{m\Omega^2 r_0^2}, \quad q_x = -q_y = \frac{4Q2(V_1 - V_2)(1-d)d)}{m\Omega^2 r_0^2}, \tag{4.7}$$

V_1 is the upper Voltage of the RF and V_2 is the lower Voltage of the RF. Here the new parameter d is implemented which is the duty cycle of the square RF-wave. With these parameters one can obtain the secular potential depth of a digital linear Paul trap that is described in [9].

$$\phi_{sec}(r_0) = c * \frac{Q^2}{2m\omega_{rf}^2} \frac{V_{rf}^2}{r_0^2} - \frac{\mu Q U_{end} r_0^2}{2z_0^2} \tag{4.8}$$

The parameter c depends on the duty cycle d and is also described in [9]. The Borealis Paul trap has a secular potential depth of around $21.2\,\text{eV}$.

61

As the Borealis setup does not have the possibility of a diagonal dc-voltage as described in equation 4.3, a variation of the duty cycle has been used to fully characterize the parameter space of the Paul trap and to scan for a mass spectrum as described in [4].

4.8.2 Development and design process of the Paul trap

The Paul trap has to fulfill the following tasks to be fit for laser cooling:
First: The Paul trap has to be able to hold C_2^- that has a mass of 24 u and a charge of 1 e.
Second: The Paul trap has to be able to eject anions radially to have them detected on an MCP mounted on top of it.
Third: The whole structure that holds the Paul trap has to be insulated from the vacuum chamber so that the trap itself can be set on a negative voltage close to the acceleration voltage.
Forth: The Paul trap needs laser access on the side to enable the laser cooling processes and places that can be used for cavity mirrors [14].
Fifth: The setup needs the possibility to re accelerate the particles after the Paul trap to make beam steering, with the trap in place, possible.
In addition all devices, parts and cables need to have enough space without creating electrical contacts that could be, in the worst case, up to 8 kV between the RF voltage of the trap and the MCP-screen.
Two trap iterations were necessary to create a fully functional Paul trap:

The first Paul trap iteration

At first it seemed important to build the whole Paul trap as simple as possible so that machining errors from the manufacturing companies would not be so serious.
The problems with the deceleration stage were not yet known and so the first iteration consisted of a trap tower that had an option build in for cavity mirrors on the side to increase the stability and accuracy of said mirrors [14]. The trap consisted of 4 long electrodes with M3 threads on both ends. These threads were used to screw the macor holders, the electric conductors and, with the help of smaller macor holders outside, the endcaps onto the trap stack as seen in 4.20a. The cables used to connect the RF electrodes to their electric feed-throughs in the flanges had to have exactly the same length to have all electrodes running synchronized. Therefore the cables had to be measured before assembly and they had to be stiff to prevent them from sinking to the ground of the chamber or onto other cables.
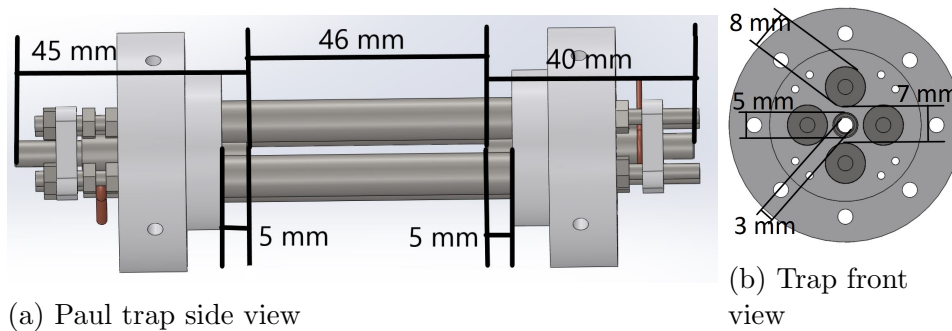The high voltage part of the deceleration stack was connected by stainless

(a) Paul trap side view

(b) Trap front view

Figure 4.20: **a** shows the first iteration of the Paul trap from the side. The trap had an overall length of $2z_0 = 46\,\text{mm}$ and all Rf rods as well as the end caps were made from 316L stainless steel. All parts are mounted in two large macor holders with $46\,\text{mm}$ in diameter that connect the trap parts to the trap tower. The two end caps (front: $40\,\text{mm}$ and rear: $45\,\text{mm}$) are held in place by 2 smaller macor parts that are used to press them against the large macor holders. The copper cable on the lower RF electrode on the left side of the picture and the copper cable mounted onto the end cap on the right side demonstrate how the electrodes are connected to their push-pull switches.
b shows the first iteration in axial direction. The trap has an overall diameter of $2r_0 = 7\,\text{mm}$. Both end caps are almost as long as the trap and have an axial hole with a diameter of $3\,\text{mm}$ that is used for particle access.

steel screws to the electric insulated Paul trap. Between the front end-cap of the Paul trap end the high voltage end cap of the deceleration stage was a small tube in between to shield the area between the two end caps from stray fields.

The trap tower, in the center of figure 4.21 was build out of aluminum. Not included in figure 4.21 is the galvanic separation of the trap tower from the CF"200 flange that is provided by several thick macor parts. The CF"200 flange has several M 10 threaded holes because in the original design it was planned to mount the trap tower on multiple positions to see what position has the best distance to use. Now there is not enough space to move the trap tower to another position as the one in the center.

On the rear end of the Paul trap a broad aluminum shield protects the re-acceleration area after the Paul trap from the stray fields from the cables that are mounted on the rear side of the trap. After the aluminium shield two meshes of $\sim 3\,\text{cm}$ diameter create a homogeneous field to re accelerate the anions again to $1740\,\text{eV}$ so that they can create a signal on the rear MCP. The MCP that is mounted on top of the trap tower has a gold mesh under-

neath as well just like the rear detector.
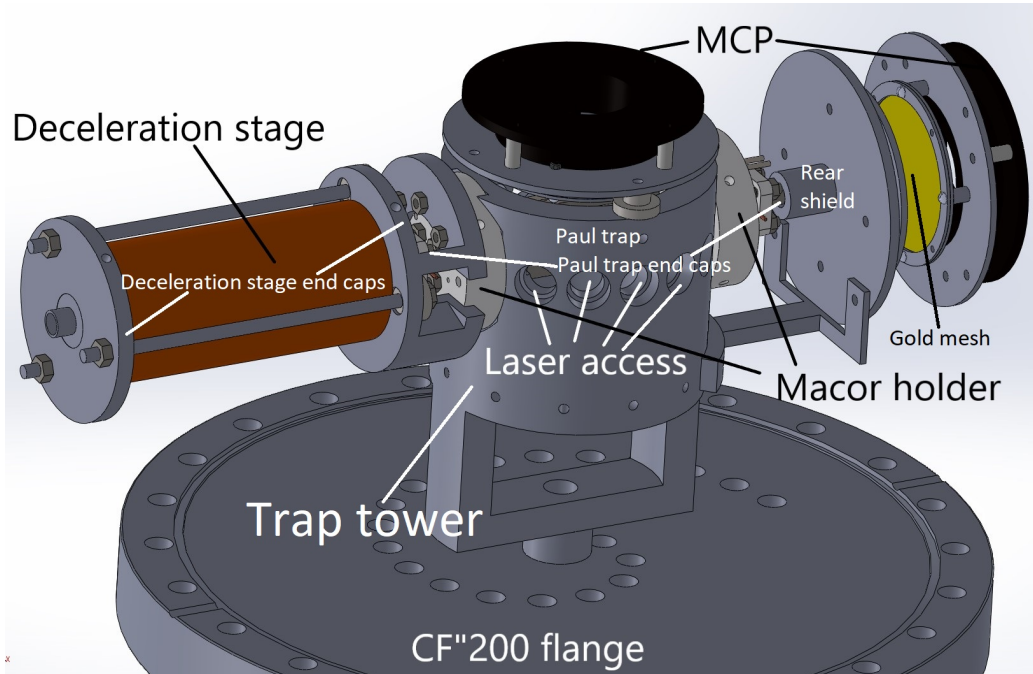
Figure 4.21: Complete Paul Trap setup with deceleration stage 4.7, trap tower with laser access points and radial (central upper part of picture) and axial (right upper part of picture) MCP. The Paul trap itself is mounted inside the trap tower so that only the two macor holders are visible on this picture. The rear shield is part of the re acceleration to get a good signal on the rear MCP.

Operation of the first Paul trap iteration

The Paul trap was designed as a digital linear Paul trap to have easy laser access and to have the RF run by fast Push Pull switches. The four-channel switch used for the RF-drive of the Paul trap was a **19"-AMX250-4E** build by **CGC-instruments** and is explained in detail in 4.9. The Paul trap had, including switch, RF rods, wires and double insulated 93Ω cables an overall capacity of about $50\,\mathrm{pF}$. The switch has the ability to switch from its normal RF-drive mode into an ejection mode, called kickout, within one RF cycle. Hereby the trap, that has normally the diagonally trap rods charged with the same voltage, now changes to charging two neighboring RF rods with the same voltage. In the case of the Borealis Paul trap that means that the trap changes from the RF mode to a DC mode where the two lower trap rods are

64

charged with the negative voltage $-V_{rf}/2$ and the two upper rods are charged with a positive voltage $+V_{rf}/2$ and they stay in this configuration until the end of the measurement. By doing this an electric potential is created that pushes the anions in the trap upwards towards the detector. The trap is held on a potential of $V_{float} \sim -1730\,\text{V}$ while the MCP is held on ground to accelerate the anions enough towards it so that they create a signal. To have a clean acceleration and an area for the anion cloud to expand between the kickout and the acceleration towards the MCP, the upper MCP has a gold mesh in front of it, that is set on the voltage $V_{up} = V_{float} + (+V_{rf}/2)$. By setting the mesh and the upper electrodes on the same voltage, a field gradient between the upper trap rods and the mesh is avoided.

The axial end cap electrodes of the Paul trap are charged up by a **Behlke HTS 11-07-HB-C** switch for negative voltages and are so brought from V_{float} to $V_{float} + V_{end}$.

However several problems prevented the Paul trap from trapping that made an iteration necessary and are described in the next chapter.

The second Paul trap iteration

After numerous electronic tests and upgrades that are described in 4.9, the Paul trap build itself was upgraded. The main reason for the update was that the deceleration stage deflected too many particles slightly to the side, that nearly none reached the Paul trap. The problem was that the end-caps of the Paul trap had a bad diameter to length ratio. So every particle that does not leave the deceleration stage in the center of it and has a maximum angle of under $arcsin(d_{endcap}/(\sqrt{d_{endcap}^2 + (l_{endcap} + l_{distance})^2}) = 3.43^0$ to the trap axis is lost on the end cap walls. Simulations had shown that the mesh at the end of the deceleration stage itself also slightly deflects particles to the side if they pass the mesh to close to one of the gold wires. With the mass filter implemented their would be too many bottlenecks to have enough particles for successful measurements.

To overcome this problem a complete redesign was done and the whole frontal end cap of the Paul trap was removed. The center hole of the macor holder on the front side of the Paul trap was opened up from 5 mm diameter to 15 mm to allow a greater particle access. The RF electrodes of the Paul trap were elongated towards the deceleration stage so that particles with an angle of $arcsin(d_{outlet}/(\sqrt{d_{outlet}^2 + l_{outlet})^2} = 24.45^0$ can still leave the deceleration stage and be lead towards the trapping region by the RF rods in a so called guiding mode, which is nothing else than the trapping mode without activated end-caps.

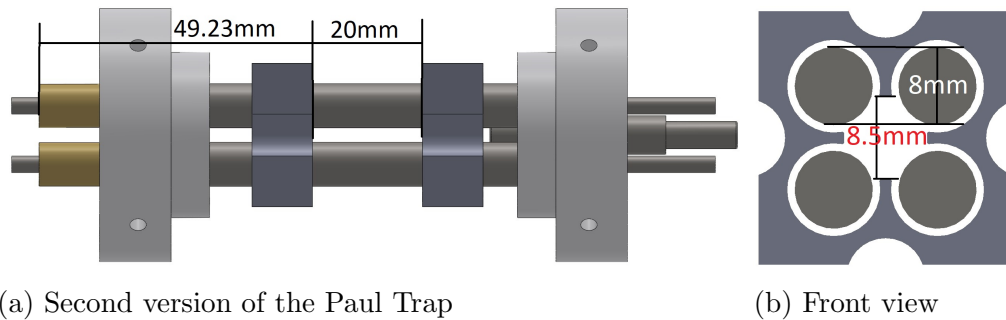(a) Second version of the Paul Trap   (b) Front view

Figure 4.22: **a**The second iteration of the Paul trap has a beam guide mounted onto the front of the Paul trap made of brass, as seen on the left side of the picture. The beam guide guides the particle beam along the RF electrodes into the new Paul trap with its outlying end cap electrodes. To enable this beam guide and also a bigger entrance hole to the trap center the trap had to be shortened to 20 mm.
b shows the new Paul trap from the front without the macor holders. The new endcaps are 1 cm long and protrude into the trap with a radial distance of 4.25 mm towards the trap center to create a stable axial potential. The round indentations on the sides of the end caps are for two correction electrodes, one horizontal, one vertical to counter possible trap inhomogeneities.

Two new end-caps were designed and mounted around the four RF electrodes of the Paul trap. For time reasons they were manufactured by hand out of brass. The mechanical connection between the end caps and the RF electrodes is done by macor spacers. Each end cap is 1 cm long and reaches into the trap up to 4.25 mm towards the trap center. The indentations on the outer sides of the end caps are used for two correction electrodes, one vertical, one horizontal. Each correction electrode is made of 2 separate copper wires connected outside of the trap. Using two copper wires was necessary to have an influence on the trap plasma without blocking the laser access. After the widening of the frontal macor holder it was no longer suitable to separate the RF electrodes from each other and keep them parallel, and so the center hole of one of the small macor holders, as seen in 4.20a has been widened up to 8 mm to have enough space for the outlet of the rear deceleration stage end cap. The now longer Paul trap apparatus is connected directly with the deceleration stage and shielded by the large brass deceleration stage end-cap 4.23.
On the rear side of the Paul trap the large macor holder and the old rear end-cap have been left in place. The old end-cap tube was necessary to avoid
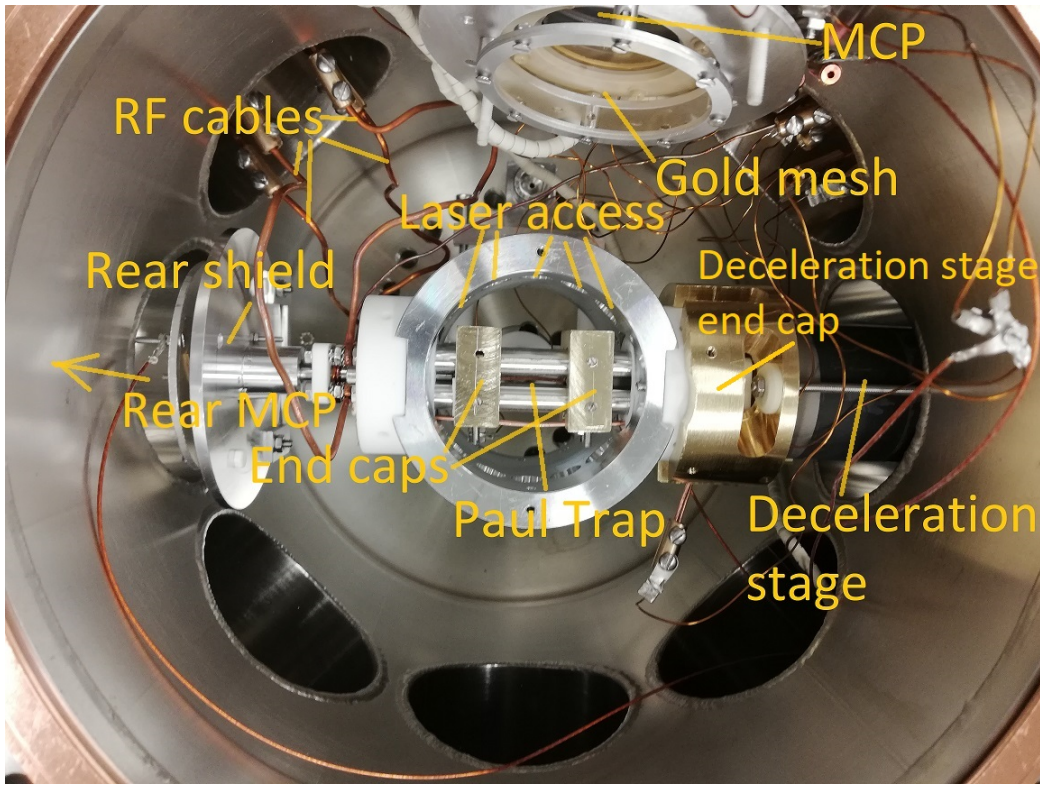
Figure 4.23: This picture shows the Paul trap chamber with the MCP moved to the side. Visible here is the deceleration stage 4.7, the second Paul trap version, the holes in the side of the trap tower for laser access, the rear shield for the re acceleration, and the MCP with a gold mesh mounted to it. Further one can see the RF cables and how they are bent to provide an equal length towards the Paul trap were they are mounted on. The rear MCP is in another vacuum chamber.

possible stray fields from the macor insulator when the anions pass through the trap to be detected on the rear MCP.

To implement the larger end-caps of the second iteration it was necessary to mount the upper MCP nearly 1 cm higher than before. Comsol 5.3 simulations have shown that this would not be a problem for the anion stream coming from the Paul trap during an ejection. The exact ejection process is explained in the simulations and measurements chapter, along with the simulations that show how two different kickout options work.

To get an ultra high vacuum two vacuum pumps are used in the Paul trap chamber. At first a **CF"63 nEXT85h** turbo pump from **Edwards** is used that can reach a theoretical vacuum of 10^{-10} mBar. Then a **NEXTorr D**
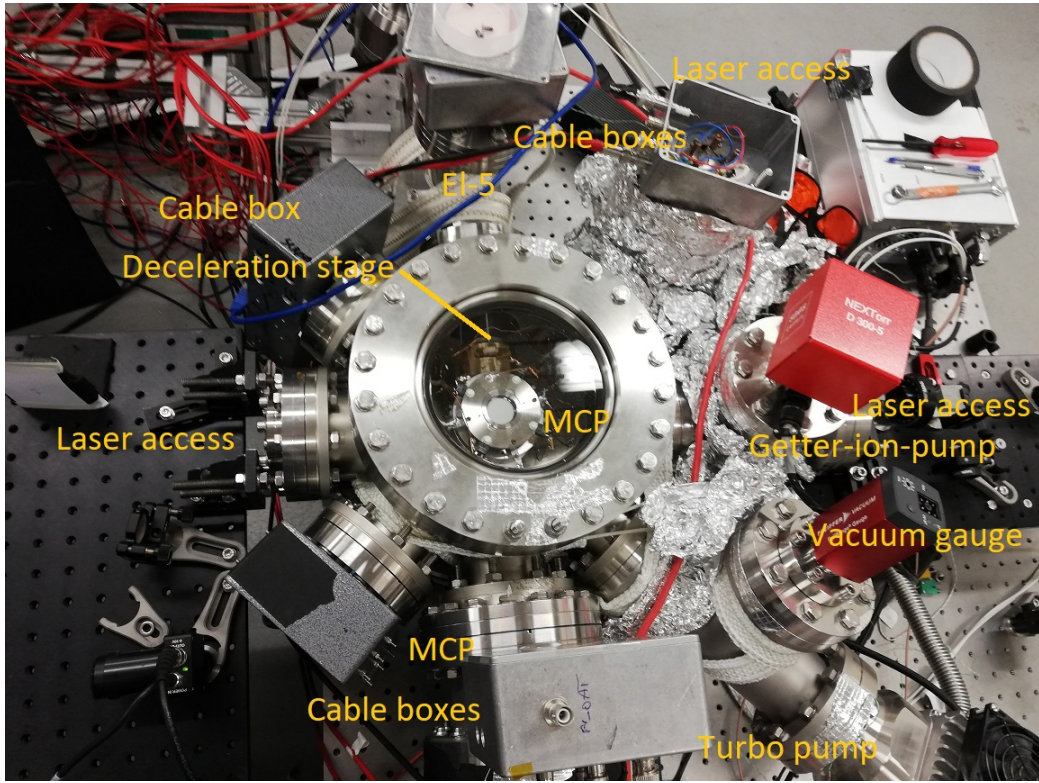
Figure 4.24: This picture shows the closed Paul trap chamber with the MCP on top of the Paul trap. Through the CF"200 view port on top of the Paul trap the MCP phosphor screen (white part of the MCP) is filmed by a high speed camera that is normally mounted on top of the vacuum chamber. In addition one can see here the vacuum chamber of El-5, five grounded cable boxes, a part of the deceleration stage, three options for laser access (one is behind the upper right cable box), the rear MCP chamber,both vacuum pumps and the vacuum gauge.

300-5 ion-getter-pump from **SAES** was used to reach even lower pressures. Unfortunately out gassing from kapton insulated cables and an UHV ready UV glue used for the cavity mirrors made it impossible to reach pressures under 4×10^{-9} mBar. And this pressure was only reachable after heating the trap for several days while the gate valve 4.2 between El-4 and El-5 was closed. Replacing the kapton insulated cables with bare ones and adding an additional gate valve in front of the turbopump to cut it off after reaching 10^{-10} mBar could help to reach even lower pressures. Further one could modify the T-chamber with the Turbo pump after El-4 4.2 and add small bushings to create a differential pump stage like the conical skimmer 4.3.

During the measurements for this thesis the radial MCP got damaged by a too high temperature during the heating process. This reduced the signal detected by it and explains the weak signals during the measurements. However a replacement was not possible during this thesis as for the long delivery times of the used MCPs **F2223-21P379** from **Hamamatsu**.

4.9 Electronics

This section gives an overview of all power supplies, measurement stations, and electronic controls, in case this information is needed for a reproduction of the experiment.

4.9.1 Borealis beam path electronics

CAEN

All electrodes along the beam path are supplied by a **CAEN SY2527** Crate with various boards:
Both MCPs, EL-1 and El-2 are supplied by a **A1832P** board.
The acceleration voltage, the beam bender correction electrodes, the negative hyperbolic beam bender electrodes, the Mesh in front of the radial MCP, the Paul trap float, and the correction electrodes of the Paul trap, as well as El-4 are supplied by two **A7030DN** boards.
El-3 and El-5 as well as the positive hyperbolic beam bender electrodes are supplied by a **A7030DP** board.
The float of the Kathode, and several correction electrodes for the mass filter have been supplied by a **A1B11** board.

Valve controller and FPGA

The Even-Lavie supersonic expansion valve is controlled by a specific controller that starts the valve and the dielectric barrier discharge [13] in a timed sequence after receiving a TTL pulse from the Field-programmable-gate-array (FPGA) **Arty FPGA**.

Vacuum gauges

Three **Pfeiffer vacuum fullrange gauges** were used to measure the pressure in the valve chamber, the acceleration chamber, and the Paul trap cham-
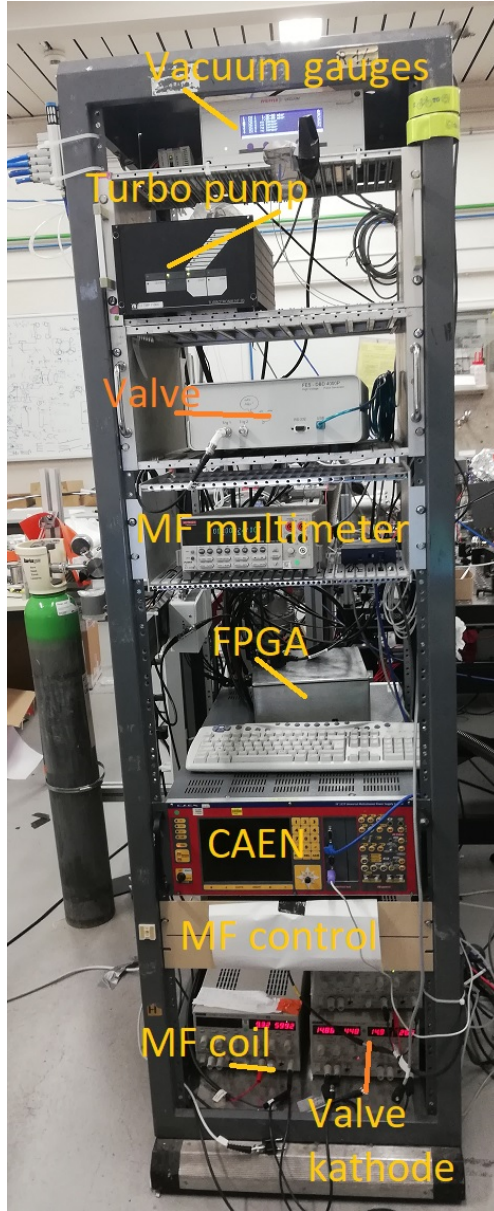
Figure 4.25: This figure shows the rack used for the Borealis setup that keeps most of the controllers and power supplies used, aside from the high voltage cage 4.27 of the Paul trap and the rack used for the Laser setup. From the top: The **Vacuum gauges box** controls the three vacuum gauges mounted onto the valve chamber 4.2, the acceleration chamber 4.3 and the Paul trap chamber. The **Turbo Pump controller** controls the pump mounted on the valve chamber. The **valve controller** controls the valve and the DBD pulse 4.2. The **Keithley 2000 multi meter** measures the actual voltage used by the mass filter for the deflection. The **FPGA box** contains the FPGA that controls and times the valve, the DBD, the Behlke switches, the RF switch, and the camera triggers. The **CAEN** supplies all electrodes, the acceleration switch and the floating of the Paul trap and the high voltage cage. The **mass filter control** consists of several manual switches that are used for the tuning of the mass filter. The three **TTI PL303QMD-P power supplies** supply the mass filter current, and the cathode in the valve chamber.

ber. The readout of the Gauges was done by a **Pfeiffer vacuum controller**.
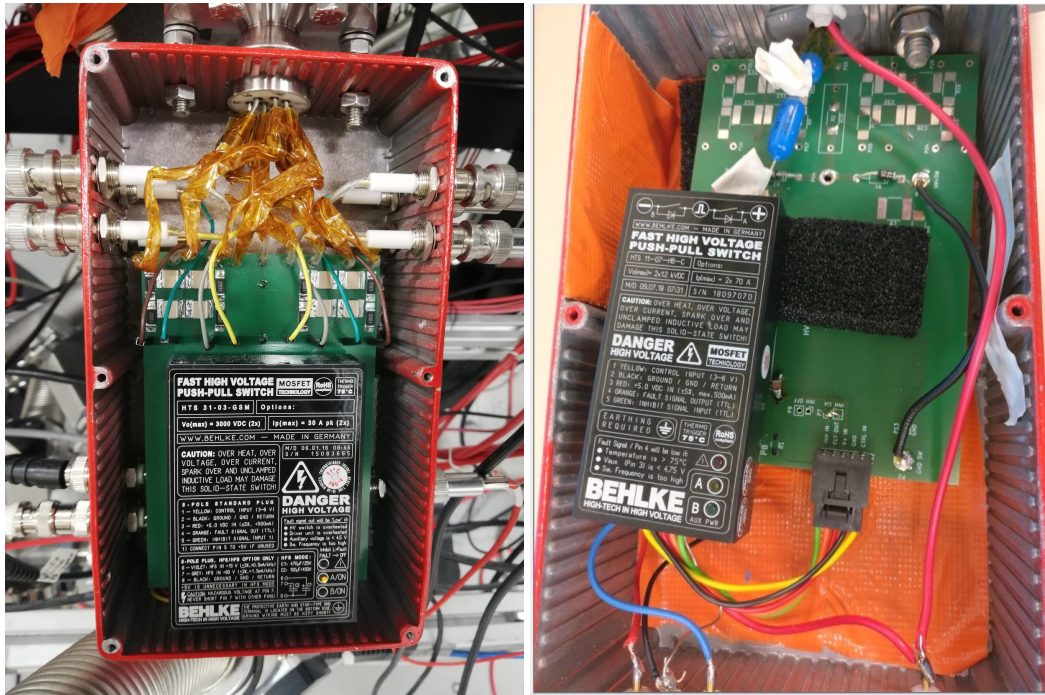
Figure 4.26:
Left picture: The high voltage box for the Behlke switch used for the beam acceleration and the cables of the first two einzellens systems El-1 and El-2.
Right picture: The high voltage box for the Behlke switch used for the end-caps of the Paul trap.

Power supplies

Two of three TTI PL303QMD-P power supplies have been used to reach the current necessary for the mass filter coils and to heat the cathode used to stabilize the C_2^- production in the supersonic expansion valve with electrons.

Oscilloscopes

An oscilloscope of the type **TDS 2024B** from **Tektronix** was used to check the signal from the fast push pull switches as well as the RF switches. In the future it is planned to connect the oscilloscope over a capacitor with the phosphor screen of the radial MCP to see the signal of the particles with a high time resolution in addition to the spatial resolution.

Mass filter controls for the electrodes

The mass filter is controlled by the CAEN A1B11 board and a row of several rotating resistances mounted on a board on the front of the electronics rack in figure 4.25

Turbo Pump controller

The four used turbo pumps are each controlled with their unique controllers.

Line trigger

An **Arduino micro** is used to scan the mains voltage to start every measurement at the same time in the frequency cycle to reduce possible errors.

High speed cameras

Two **AV MAKO G-234B POE** cameras from **STEMMER IMAGING AG** are used on both MCPs to detect the optical signal from the phosphor screens.

Cables

For the Paul trap mostly SHV cables were used for the high voltage supplies and normal BNC cables for the low voltage supply. The RF electrodes of the Paul trap were connected with $\sim$40 cm long double shielded 93Ω cables to grant an overall capacity of the Paul trap of $\sim$50 pF.

4.9.2 Paul trap electronics

To float the Paul trap and all its electrodes to a negative voltage close to the acceleration Voltage (-1740 V) of the acceleration switch 4.3, a high voltage cage 4.27 was build that includes all controls, power supplies and push-pull switches the Paul trap needs. A **Drehstrom-Trenntransformator 400 V / 400 V, 2,5 kVA** from **Taunus Transformatoren** is used to operate all devices in the cage with up to 400 V which is necessary to run the **Delta SM300-10D** Powersupplies from **Delta electronika** that require a 380 V three phase current. The cage is separated from the outside ground and is floated together with the Paul trap to an internal ground of -1730 V with one **CAEN-A7030DN** board. The cage consists of grounded aluminum plates and has only small openings for cable in- and out-lets. To reduce the risks of an accident the cage is placed under the optical table that holds the
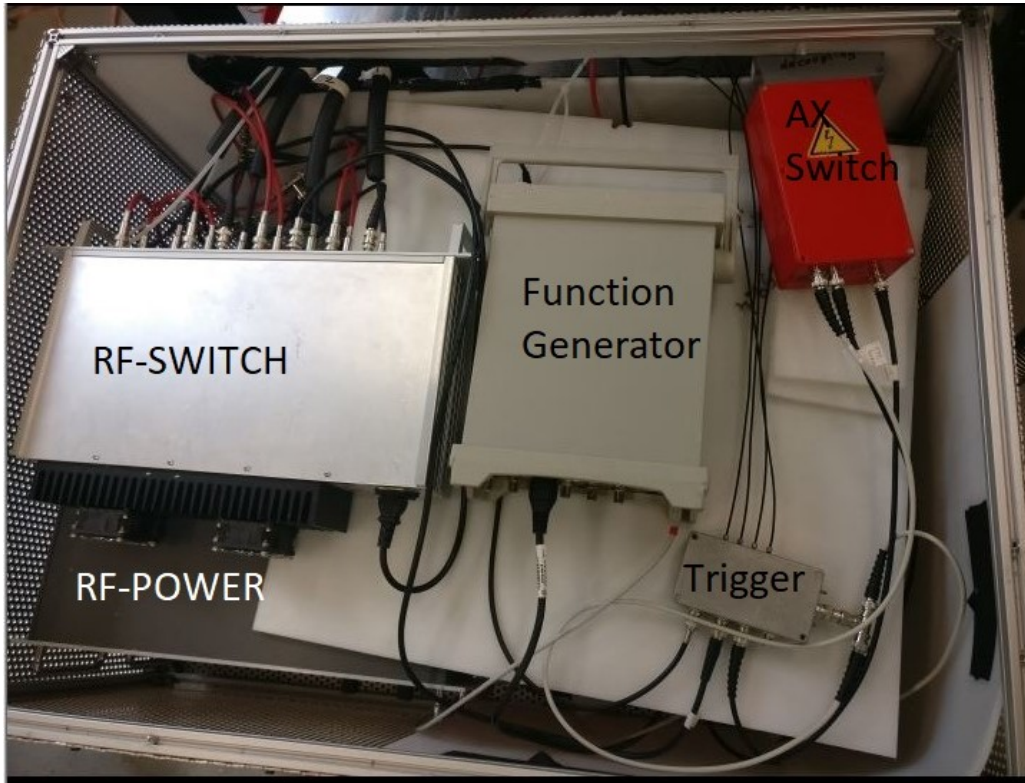
Figure 4.27: This picture shows the open high voltage cage. On the left side are two **Delta SM300-10D** Powersupplies from **Delta electronika** and on top of them the RF-switch **19"-AMX250-4E** from **CGC-instruments**, in the middle is a function generator **33210a** from **Agilent**, and on the right side is a box for a **Behlke HTS 11-07-HB-C, Vmax=1200V**, using a load resistor of 45 Ohm 4.26) switch to control the trap end-caps. In the lower right corner is the trigger box that transforms the optical signals from the FPGA into a TTL pulse of around 5 V.
Out of sight under the white plastic plate are the USB hub, two **TTI PL303QMD-P** Power suplies to supply all other devices, a **Keithley 2410E** for the negative end cap voltage, two **PSC 44M** power supply controls for the **Delta SM300-10D** also from **Delta electronics**, an isolation transformer **Drehstrom-Trenntransformator 400 V / 400 V, 2,5 kVA** from **Taunus Tranformatoren** and an optical USB cable to control all devices in the cage **USB Isolator STD 1.0 LWL** from **Baaske medical**.
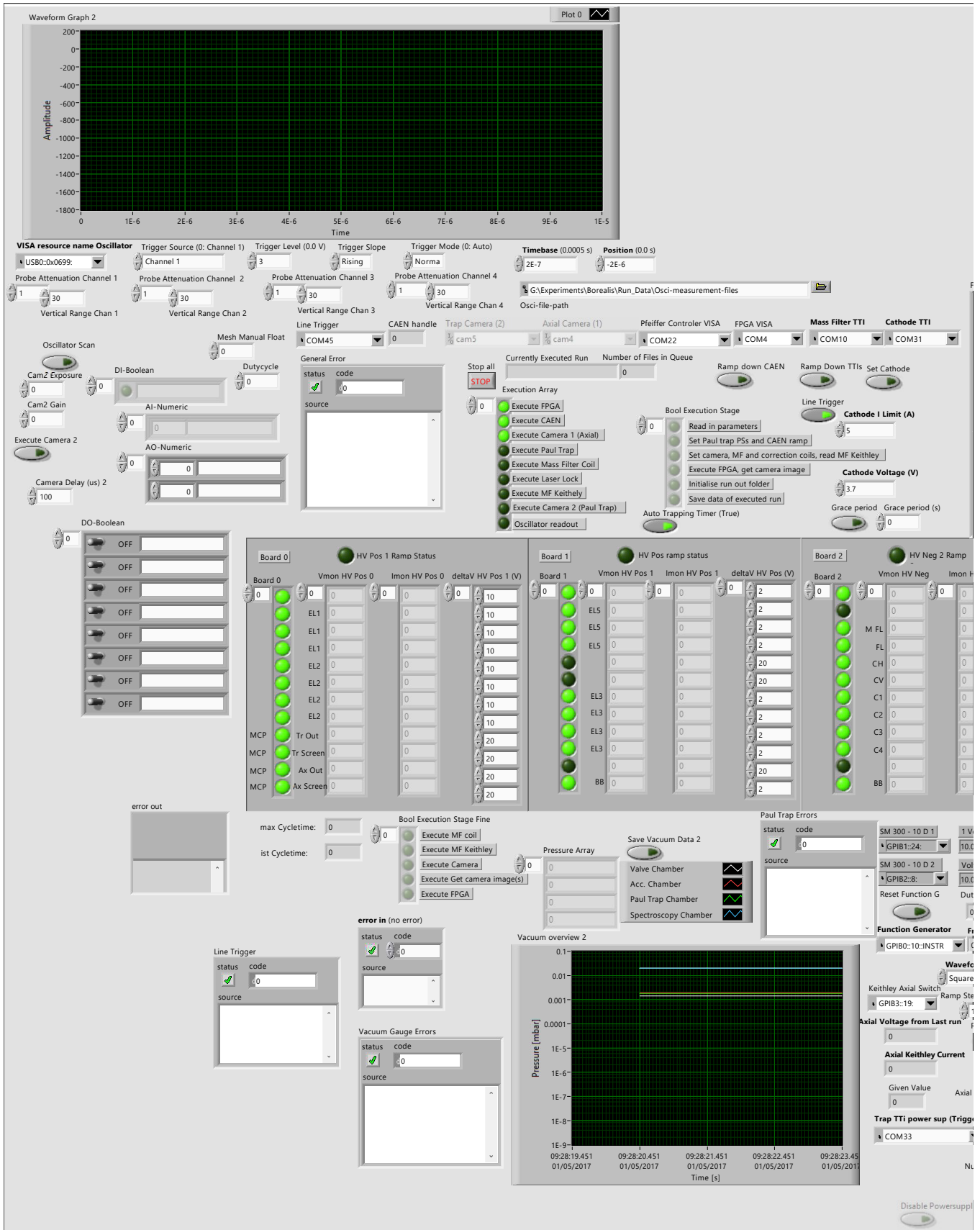
Paul trap. To open the the cage, it has to be extracted with a pallet lifter which requires the main power cable to be disconnected. As part of this

thesis all electronics concerning the Paul trap, as well as several others have been installed or improved.

4.10   Software

The software for the Borealis experiment was written in **Labview2015** from **National Instruments**. The front panel figures, down below, of the experiment control everything from the Valve trigger over all electrodes up to the trapping procedure in the Paul trap. A Labview program creates a so called run file that obtains all parameters necessary, which is then read in by another Labview program, the so called run sequence, that reads all parameters, operates all devices necessary and gathers the data from the two high speed cameras and the oscilloscope. As part of this thesis all VIs concerning the Paul trap have been written and most other VIs of the software have been improved. The next two pages show the graphical user interface of the Run-Sequence VI, that gives an overview over all systems of a measurements. The images taken (the two black squares in the right lower corner, are used for most measurements, that require particle count or distribution.

Waveform Graph 2

Plot 0

Amplitude

Time

VISA resource name Oscillator
USB0::0x0699:

Trigger Source (0: Channel 1)
Channel 1

Trigger Level (0.0 V)
3

Trigger Slope
Rising

Trigger Mode (0: Auto)
Norma

Timebase (0.0005 s)
2E-7

Position (0.0 s)
-2E-6

Probe Attenuation Channel 1
1   30

Probe Attenuation Channel 2
1   30

Probe Attenuation Channel 3
1   30

Probe Attenuation Channel 4
1   30

Vertical Range Chan 1

Vertical Range Chan 2

Vertical Range Chan 3

Vertical Range Chan 4

G:\Experiments\Borealis\Run_Data\Osci-measurement-files
Osci-file-path

Oscillator Scan

Mesh Manual Float
0

Line Trigger
COM45

CAEN handle
0

Trap Camera (2)
cam5

Axial Camera (1)
cam4

Pfeiffer Controler VISA
COM22

FPGA VISA
COM4

Mass Filter TTI
COM10

Cathode TTI
COM31

Cam2 Exposure
0

DI-Boolean
0

Dutycycle
0

General Error
status   code
0
source

Stop all
STOP

Currently Executed Run

Number of Files in Queue
0

Ramp down CAEN

Ramp Down TTIs

Set Cathode

Cam2 Gain
0

AI-Numeric
0

Execution Array
0

Execute FPGA
Execute CAEN
Execute Camera 1 (Axial)
Execute Paul Trap
Execute Mass Filter Coil
Execute Laser Lock
Execute MF Keithely
Execute Camera 2 (Paul Trap)
Oscillator readout

Bool Execution Stage
0
Read in parameters
Set Paul trap PSs and CAEN ramp
Set camera, MF and correction coils, read MF Keithley
Execute FPGA, get camera image
Initialise run out folder
Save data of executed run

Line Trigger
Cathode I Limit (A)
5

Cathode Voltage (V)
3.7

Execute Camera 2

AO-Numeric
0
0

Camera Delay (us) 2
100

Auto Trapping Timer (True)

Grace period   Grace period (s)
0

DO-Boolean
0
OFF
OFF
OFF
OFF
OFF
OFF
OFF
OFF

Board 0   HV Pos 1 Ramp Status

Board 1   HV Pos ramp status

Board 2   HV Neg 2 Ramp

Board 0
Vmon HV Pos 0   Imon HV Pos 0   deltaV HV Pos 1 (V)
0   0
EL1   0   0   10
EL1   0   0   10
EL1   0   0   10
EL2   0   0   10
EL2   0   0   10
EL2   0   0   10
EL2   0   0   10
MCP   Tr Out   0   0   20
MCP   Tr Screen   0   0   20
MCP   Ax Out   0   0   20
MCP   Ax Screen   0   0   20

Board 1
Vmon HV Pos 1   Imon HV Pos 1   deltaV HV Pos (V)
0   0
EL5   0   0   2
EL5   0   0   2
EL5   0   0   2
0   0   20
0   0   20
EL3   0   0   2
EL3   0   0   2
EL3   0   0   2
EL3   0   0   2
BB   0   0   20

Board 2
Vmon HV Neg   Imon H
0   0
M FL   0
FL   0
CH   0
CV   0
C1   0
C2   0
C3   0
C4   0
0
BB   0

error out

max Cycletime: 0

ist Cycletime: 0

Bool Execution Stage Fine
0
Execute MF coil
Execute MF Keithley
Execute Camera
Execute Get camera image(s)
Execute FPGA

Pressure Array
0
0
0
0
0

Save Vacuum Data 2

Valve Chamber
Acc. Chamber
Paul Trap Chamber
Spectroscopy Chamber

Paul Trap Errors
status   code
0
source

SM 300 - 10 D 1
GPIB1::24:

1 V
10.0

SM 300 - 10 D 2
GPIB2::8:

Vol
10.0

Reset Function G

Dut

Function Generator
GPIB0::10::INSTR

error in (no error)
status   code
0
source

Vacuum overview 2

Wavefo
Square

Keithley Axial Switch
GPIB3::19:

Ramp Ste

Axial Voltage from Last run
0

Axial Keithley Current
0

Given Value
0

Axial

Trap TTi power sup (Trigge
COM33

Line Trigger
status   code
0
source

Pressure [mbar]

09:28:19.451   09:28:20.451   09:28:21.451   09:28:22.451   09:28:23.45
01/05/2017   01/05/2017   01/05/2017   01/05/2017   01/05/2017
Time [s]

Vacuum Gauge Errors
status   code
0
source

Disable Powersuppl

FPGA Values

0
0
0
0
0
0
0
0
0
0

Laser + 15 V PS TTI
COM28

MF Keithley
COM26

FC in

Single FC in

Mass Filter Coil Current (A)
0

Mass Filter Coil Voltage (V)
0

MF Electrode Voltage
0

Select ADC Traces
0

Laser Error
status   code
0

Laser Shutter
0   CLOSED (0) /
OPEN (1)

0   LaserLockSP
0.00000   Current SP
0   SP Tolerance [%]

0   **Wavelength**   0   Working
Point (WP)

WP in SP-Range?

STOP

source

MF Ramp Down Error
status   code
0

source

ADC TT

Board 3

HV Neg 2 Ramp Status 2

Board 5

MF Ramp Status

Board 3

Vmon HV Neg 3   Imon HV Neg 3 DeltaV HV Neg 3 (V) 2

Board 5

Vmon MF Pos/Neg   Imon MF   deltaV Pos/Neg MF

HV Neg 2 DeltaV HV Neg2 (V)

0   20
20
10
10
10
3
3
3
3
5
3

0   0   0.88   0   3
EL 4   0.93   0   3
EL 4   0   0   3
EL 4   0.83   0   3
0.78   0   20
0.91   0   20
Def 1   0.94   0   3
Def 2   0.92   0   3
Def 3   0.63   0   3
Def 4   0.76   0   3
1.01   0   5
0.97   0   3

0   0   0   0   3
Cath Bias   0   0   0   3
0   0   0   3
0   0   0   3
0   0   0   3
0   0   0   3
0   0   0   3
0   0   0   3
0   0   0   3
0   0   0   3
0   0   0   3
0   0   0   3

TT Mean   TT Standard Deviation
0   0

ADC 1   0   0
ADC 2   0   0
ADC 3   0   0
ADC 4   0   0
ADC 5   0   0
ADC 6   0   0

Acquired image 2 Paul Trap MCP

Acquired image Axial MCP

Voltage   1 Current
0   0.00
Voltage   2 Current
0   0.00

ycycle(%)

requency [kHz]

orm
2

ep Size Axial Switch (V/s)
0

Reset Keithley

Axial Voltage readout
0

Switch Readout

Manual MCP Mesh (On)

umber of Files in Queue 2
0

ies in Cage

Currently Executed Run

Currently Executed Run

In addition another Labview VI was created and, as part of this thesis, improved to evaluate the pictures made by the cameras and to do an immediate analysis of the data.

4.11 A typical measurement

A typical measurement is performed as follows: At first all participating devices have to be online, connected to the control computer and operational. The gas bottle that is used by the valve 4.3 has to be open. Then all parameters for all electrodes have to be written in the "Run creator VI" as this file creates a text file that contains a table with all parameters for the measurement. The next step is that the Run sequence VI reads the text file and sets all power supplies on their correct values. This takes about 5 minutes if one starts from zero, as the MCPs need high voltages but should not be ramped up faster than $20\,\mathrm{V/s}$.

After reaching this voltage the FPGA sends trigger pulses in the correct order. First the valve 4.3, injects a gas stream and ionizes it with the DBD pulse. Then the produced C_2^- moves towards the acceleration electrode 4.3. The acceleration electrode is set on a time value that is best for the acceleration of C_2^- and, after a further trigger pulse from the FPGA the Behlke switch ramps up the acceleration electrode and accelerates the anions towards the mass filter 4.5. Here C_2^-, C_2^H- and H_2CC^- is separated from other anions and moves towards the beam bender 4.6 to be separated from the neutral particles. After re-focusing and re-steering in El-4 and El-5 4.4, the bunch of anions reaches the deceleration stage 4.7, where the kinetic energy of the anions is reduced to around $10\,\mathrm{eV}$ or lower if needed. After that the FPGA sends a trigger pulse towards the RF switch to start, with usually $F = \frac{\Omega}{2\pi} = 3\,\mathrm{MHz}$ and $V_{rf} = 248\,\mathrm{V}$. With an active RF switch the anions are guided towards the center of the Paul trap. Here the FPGA sends another pulse to activate the Paul trap end-caps that are required to finally trap the anions in the Paul trap. After the laser cooling procedure, a last pulse from the FPGA activates the radial kick out of the Paul trap and ejects the anions towards the Paul trap MCP. At the same time another trigger starts the recording of the camera that is used to detect the signal from the phosphor screen. The image is the saved by the run sequence VI and is ready for data evaluation. Several measurements and an image made by one of the cameras of a typical trapping run can be found in the simulations and measurements chapter 2.0.3.

77

Chapter 5

Simulations and measurements

This chapter will focus on the theoretical and experimental data that was simulated and measured to characterize all components of the Paul trap including the fully operational Paul trap itself. The chapter holds information about the deceleration stage, the ejection mode, the beam form, the stability regions of the Paul trap, and a mass spectrum measured in the Paul trap by varying the duty-cycle, as described in [4].

5.1 Simulations of the deceleration stage

To build a working deceleration stage several Comsol simulations, and work steps were necessary, from which the final ones are shown here. The simulations were calculated with COMSOL 5.2, COMSOL 5.3 and COMSOL 5.3a. The first simulation shows the deceleration stage of the first Paul trap iteration and was done to get an idea why the amount of anions detected in the Paul trap was so low, when it was tried to float it to high negative voltages. At first the space charge and a non parallel beam were looked into in the simulations to find out if these influences would explain the bad results. Both the space charge simulation and the offset simulation have shown, that the biggest particle loss was in the thin frontal end cap of the Paul trap. The expected problem, of the bunch lumping together, when the kinetic energy is reduced was less than expected, except when the kinetic energy is reduced to 1-2 eV. Further simulations have shown that the gold mesh had a negative influence as well. It has to be said that simulations 5.1 and 5.2 were performed with a $\sim 100 \mu s$ anion beam, which is only the case when no mass filter is used. Using the mass filter reduces the amount of anions therefore the space charge, which results in a bunch length of about $\sim 40 \mu s$.
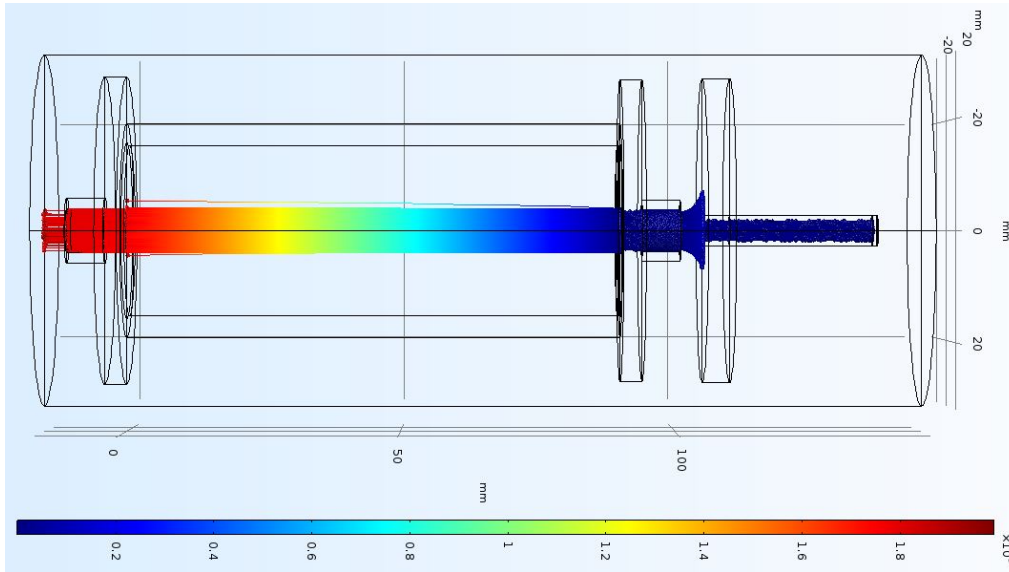
78

Figure 5.1: This beam simulation was created with COMSOL 5.3 and shows an anion beam of 10000 single C_2^- anions that come in packs of 10 in 100 ns steps with a kinetic energy of 1800 eV. The charge of each anion was raised to 100 e to raise the space charge artificially of the whole bunch. The charge of the deceleration stage was reduced from -1798 V to -17.89 V so the effect of the higher space charge would only be seen between the particles. The lengths are in mm and the color code goes from dark blue for 0 eV to dark red for 1800 eV

Simulation 5.3 shows how the particles are guided towards the trap center in the second iteration of the Paul trap build. The RF electrodes are active during this simulation which induces a slight reflection right at the beginning of the RF electrodes. This reflection appears as the front area of the RF electrodes is visible from inside the 11 mm long outlet of the deceleration stage. However experiments have shown that a later activation of the RF drive does not significantly improve the amount of trapped particles, so this does not seem to be a big problem.

The radial trapping directly after the deceleration stage enables now anions that have an angle of $\sim 24.45^0$ 2.0.3 towards the Paul trap center axis, to reach the trap center which increases the number of anions a lot.

The gold mesh itself has shown in the simulations that it has a higher impact on charged particles with a low kinetic energy than expected. In simulation 5.3 this can be seen as a slight kink at the position of the gold mesh between the 90 mm deceleration stage and the 11 mm outlet.
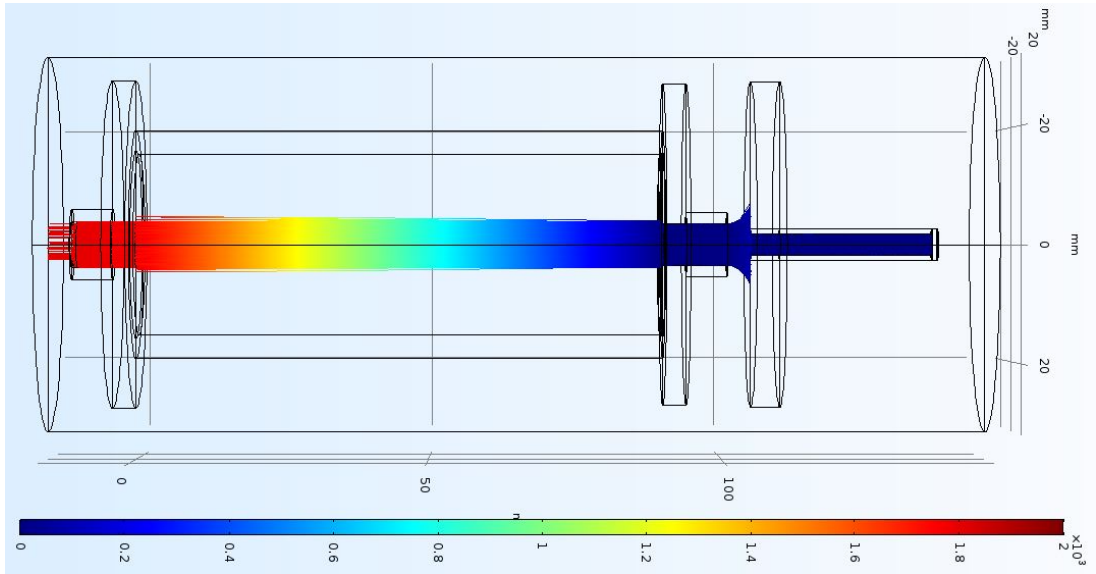
79

Figure 5.2: The same beam simulation as in 5.1 but here the 1800 eV beam also has a radial kinetic energy of 4 eV to simulate an offset by a voltage ripple in the electrodes. Though the maximum ripple should not be higher than 0.5 V, the 4 V have been chosen to see when the deflection was strong enough to have no anions in the trap at all. The lengths are in mm and the color code goes from dark blue for 0 eV to dark red for 1800 eV
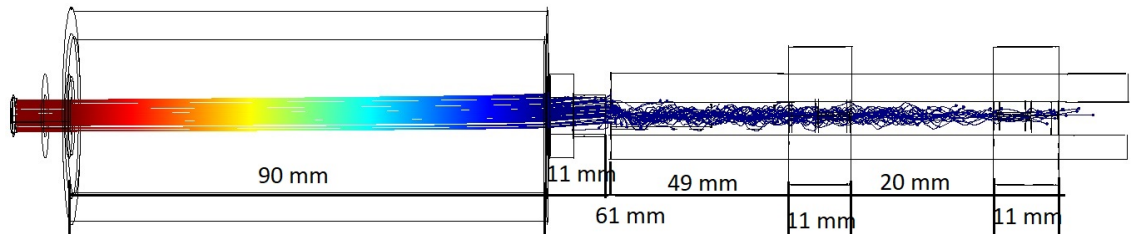

Figure 5.3: This simulation shows the second iteration of the Paul trap and how a particle beam with an axial kinetic energy of 1800 eV and a radial kinetic energy of 15 eV, that points upwards in the picture, is reduced to ~5 eV and enters the Paul trap. Here the active RF electrodes guide the particles towards the center of the trap between the two 10 mm broad endcaps.

5.2 Paul trap simulations

Several simulations were performed with COMSOL 5.3a for a better understanding of the Paul trap behavior. The most important fact that was learned

80

is that the deceleration stage injects the anions not into the radial center of the Trap but more to the side. Because of the Paul trap's rather slow RF drive of 3 MHz the anions move further away from the radial center of the trap at the beginning of the trapping process. Because of this, a considerable amount of anions is lost on the electrodes as seen in Figure 5.4. After
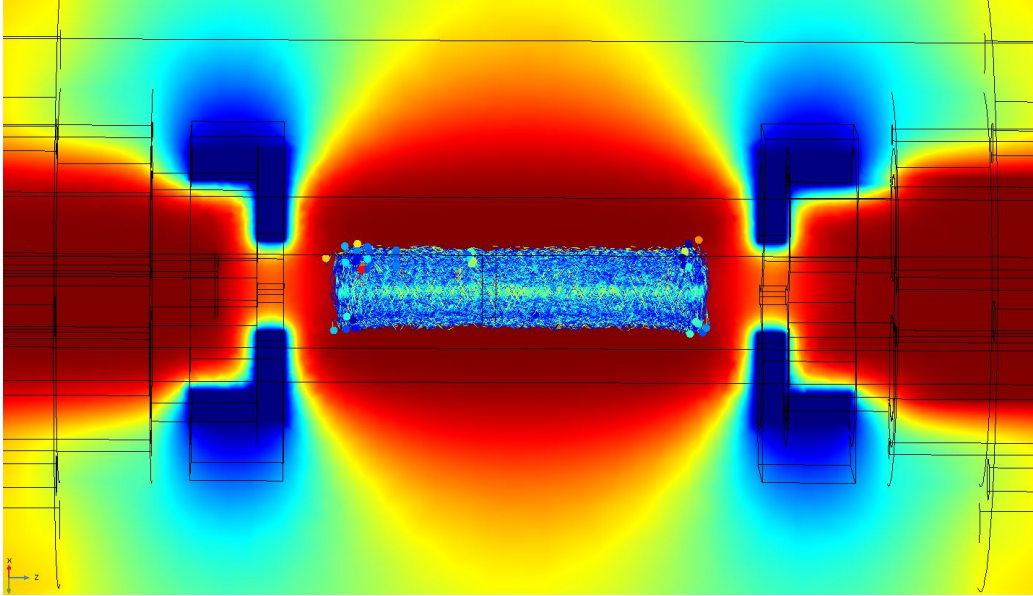

Figure 5.4: This simulation shows the trapping of the C_2^- molecules for 1 s in the second iteration Paul trap. The bright dots around the center of the Paul trap show anions that touch the RF electrodes and are lost. For this simulations 100 anions with mass 24 were simulated that have a starting position at $z = 0$ and $r \in 0->r_0$. One can see that the lost particles accumulate around the ends of the Paul trap. It is not entirely clear if this is due to an insufficient simulation or the explanation of the visible particle loss over different trapping periods. For simplicity in this simulation a harmonic drive was simulated. According to literature [21] the trapping effect of a digital Paul trap should be stronger than the one of a harmonic Paul trap for the same parameter values

the RF drive of the Paul trap the kickout function was simulated as well. The original idea was to set the two neighboring lower electrodes on negative $V_{float} - V_{rf}$ and the two upper electrodes near the radial MCP on the floating ground V_{float} instead of $V_{float} + V_{rf}$ as described in 2.0.3. According to the Manual of the **AMX250-4E** switch both options are available but the "to ground" version was slower as seen in Figure 5.5. 5.5 shows that, despite the loss of some particles on the two upper electrodes, enough anions for a
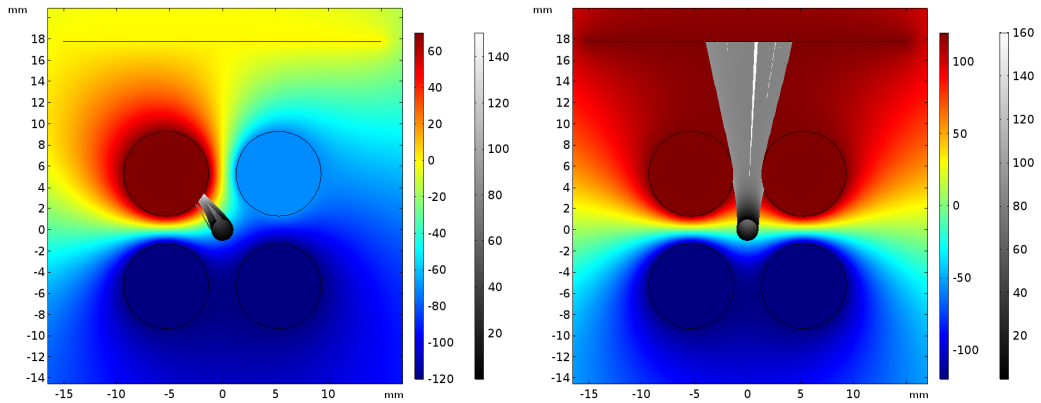
Figure 5.5: These Pictures show show the electric potential $600\,\text{ns}$ after the FPGA signal for the kickout was given. The view is here from the front of the Paul trap.

Left picture: This picture shows the trap when the switch ramps the two upper electrodes from $+/-120V_{rf} + V_{float}$ to V_{float} within $5\,\mu s$ after the last $\sim$330 ns RF cycle (at 3 MHz). For this option the anion plasma in the trap hits the positive electrode after the last 300 ns RF cycle within $\sim$500 ns. It is obvious that when the two lower electrodes are both already on there negative voltage after $\sim$15 ns and the two upper electrodes are almost $3.5\mu s$ away from reaching V_{float} a straight particle ejection is not possible. The black line, in the upper area of the picture, that depicts the gold mesh in front of the MCP is on ground in this configuration.

Right picture: The second picture shows the kickout when a jumper-contact is set and two upper electrodes are ramped to +120 V after one RF cycle of up to $330\,ns$. In this configuration the ramp itself takes only $\sim 15ns$ and the kickout of the Paul trap is performed a lot faster and therefore a lot cleaner. In this configuration the gold mesh in front of the MCP is on the same voltage as the upper electrodes so that the anions are not accelerated further before reaching the mesh.

In both pictures the colored scale depicts the voltage of the electrodes and the mesh, while the gray scale is the particle energy in electron volt that starts at 0.1 eV. The electrode voltage starts at -120 V at dark blue and goes to +70 V on the left picture and to +120 V on the right picture.

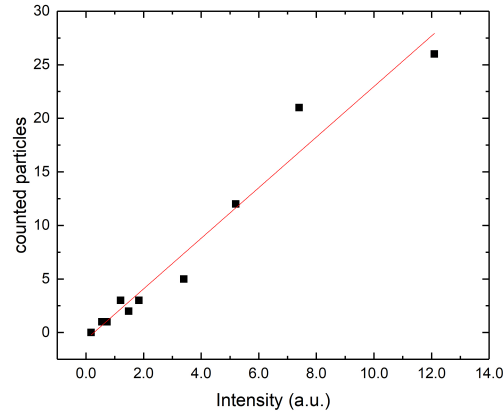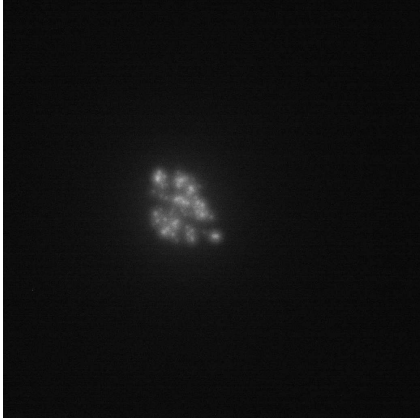measurement reach the MCP in the right configuration.

82

Figure 5.6:
Left picture: This is a typical measurement. The brightness of the overall picture is used to count the particles and the mean width of the bunch will be used for future temperature measurements.
Right picture: Particles counted by hand over the measured intensity (Brightness of the picture). The MCPs that were used in this experiment were not specifically designed to detect anions. To be sure that the measured intensity of the measurement aligns with the counted particles, a calibration measurement was done were all hits on the phosphor screen were counted by hand to see if the intensity correlates with the pixel count.

5.3 Measurements of the deceleration stage

All made measurements on the Paul trap and the deceleration stage were performed by analyzing images made by the high speed cameras of the MCP screens.

To understand the influence of the space charge on the particle bunch, and the lumping of the bunch, a measurement was performed to determine the width of the gauss curve that represents the intensity over the ejection voltage $V_{ejection}$. A wider gauss curve would mean that the kinetic energy of the anions is distributed widely because an anion can only reach the MCP if the ejection voltage accelerates the anions towards the MCP with the right kinetic energy. By comparing different deceleration Voltages (V_{float}) one can see the energy distribution in the old trap (first iteration). Though an intensity drop at higher ejection voltages is visible in the 120 V ejection range of the 40 eV curve in figure 5.7. This is likely due to the higher kinetic energy of the anions when passing the outer area of the mesh so they do not reach
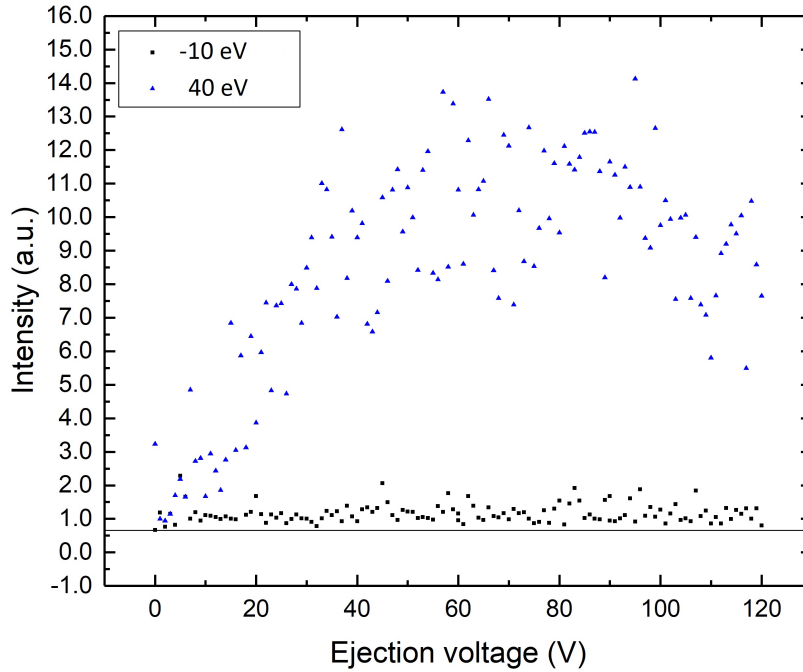
83

Figure 5.7: Anions with a kinetic energy of $\sim 1740\,\mathrm{eV}$ were transferred into the deactivated first iteration trap, at $V_{float} = 1700\,\mathrm{V}$ (blue triangles) and at $1750\,\mathrm{V}$ (black squares). The lower rods of the Paul trap were kept on a negative kickout voltage $-V_{ejection}$ and the upper rods on a positive $+V_{ejection}$. One can see that the anions that are decelerated to $\sim 40\,\mathrm{eV}$ show a hill over their kickout voltage at an ejection voltage of around $60\,\mathrm{V}$ (+/- $20\,\mathrm{V}$), which means that the majority of the anions have a kinetic energy of $\sim 40\,\mathrm{eV}$ +/- $20\,\mathrm{eV}$. The other curve that represents a voltage that is higher than the acceleration voltage should actually deflect the anions, but still shows a complete flat, but visible intensity curve. So there is still a significant amount of anions with a kinetic energy that is higher than their acceleration voltage V_{acc}. This additional energy comes most likely from the spacecharge that accurs when the bunch lumps together in the deceleration stage.

the MCP inlet very well.
Figure 5.7 is not accurate enough for explicit details of the kickout mode but it is accurate enough to see that the energy distribution is a lot higher for low energy particles reaching the trap. For $40\,\mathrm{eV}$ anions the curve shows a broad

84

but visible energy distribution while for a floating voltage that is higher than the acceleration voltage the distribution is completely flat as expected. The anions are not deflected due to their high space charge when the whole $100\,\mu s$ anion bunch is lumped together and a part of the anions is re accelerated enough to get over this $10\,\mathrm{V}$ barrier. The flat curve indicates that the energy distribution is a lot wider than the possible ejection voltage of the Paul trap. This measurement was not repeated for the second Paul trap iteration due to a lack of time.

5.4 Measurements in the Paul trap

After the first successful trapping attempts the whole Paul trap was characterized to find possible inaccuracies in the mechanical design or the electronics. Further it was begun to find the best trapping conditions to trap and keep as many low energy anions of the C_2^- species as possible in the Paul trap for as long as possible.

Figure 5.6 shows that the counted particles align with the intensity so the measured intensity is a usable value for all measurements. However the graph 5.6 goes up to around 30 particles and not higher. It is not possible to count more particles by hand, because hits that are too close to each other merge and are brighter, but cannot be separated. For the planned laser cooling measurements a small amount of particles is sufficient as the time of flight measurement will require only the mean diameter of the whole bunch.

5.4.1 a-q-space-measurement

In this section the first stability region [1] of the a-q-space of a digital linear Paul trap was measured by trapping anions in it. This was necessary to find the region that traps most anions, and to gather data for a mass spectrum in the Paul trap. Using

$$a_x = -a_y = \frac{8Qd(V_1 + (1-d)V_2)}{m\Omega^2 r_0^2}, \quad q_x = -q_y = \frac{4Q2(V_1 - V_2)(1-d)d)}{m\Omega^2 r_0^2},$$
(5.1)

one can see that it is possible to scan various points on the a-q-space by varying Ω, $V_{rf} = V_1 - V_2$ and d. Because of technical limitations it was not possible to use frequencies of $\Omega > 3\,\mathrm{MHz}$ or voltages of $V_{rf}/2 > 125\,\mathrm{V}$. So the measurement had to be performed in two steps.

At first Ω was set on $3\,\mathrm{MHz}$ and the voltage was ramped from $V_{rf}/2 = 0$ to $V_{rf}/2 = 124\,\mathrm{V}$. This was done for 29 different dutycycles from $d = 0.36$ up to $d = 0.64$. Then the same measurement was performed with a fixed

voltage $V_{rf}/2 = 124\,\mathrm{V}$ and the frequency Ω was ramped from $3\,\mathrm{MHz}$ down to $2.35\,\mathrm{MHz}$. This produced the measurement in Figure 5.8. Each measurement included a $200\mu s$ trapping to see if the Paul trap holds anions with the said configuration and for each measurement the trapping started $273\mu s$ after the supersonic expansion valve inlet. To improve the intelligibility of the
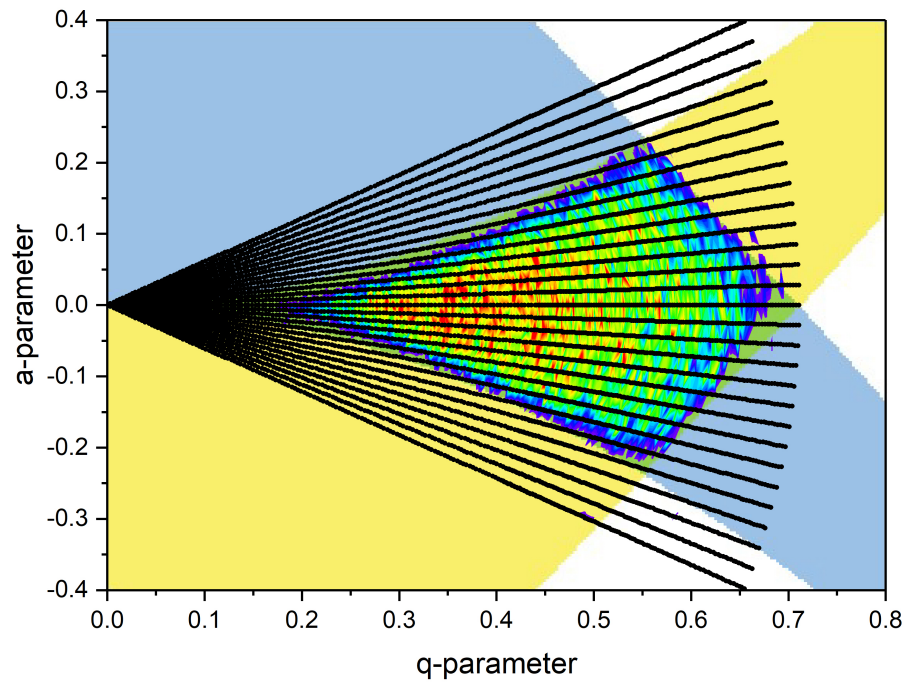

Figure 5.8: Complete measurement of a-q-parameter space with measurement points (Black). The vertical scan-direction was performed by varying the duty-cycle. The horizontal scan-direction was performed by varying the voltage V_{rf} and the frequency Ω_{rf}. Each measurement point consists of $200\,\mu s$ trapping duration. The simulated stability regions (light blue for y-direction and yellow for x-direction) were calculated by a spreadsheet file from [6]. The color code goes from violet (no intensity) to dark red (highest intensity) in arbitrary units. The black lines indicate the individual measurement points (each point taken 5 times, ~ 30000 measurements in total

a-q-measurement a smoothing function from Origin 17 was used on the measurement and a self programmed function of the matrix transform method [21] was calculated by Emanuel Oswald to compare the measurements with

the theoretical a-q-space. One can see that the measured values for the a-q-space do not align perfectly with the simulated boundary conditions. This can have several reasons: When the radial MCP started to malfunction it
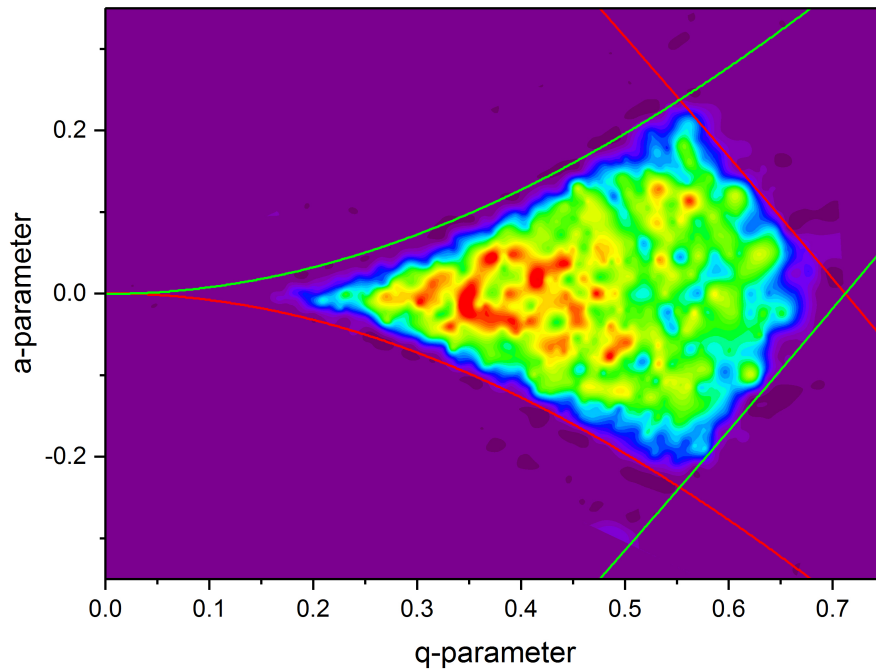

Figure 5.9: The complete a-q-characterization as in 5.8 but smoothed by an Origin 17 function. The color code goes in arbitrary units from dark violet for no intensity to dark red for a high intensity signal. The simulated stability functions for x-axis (red) and y-axis(green) were written by Emanuel Oswald in a python script.

was necessary to set the mesh in front of it on the same voltage of as the MCP inlet, which is ground, to prevent field induced signals on the MCP. Because of this there is now a potential difference of about 1740 V between the Paul trap and a gold mesh that is $\sim$3 cm away from the trap center. According to a COMSOL 5.3 simulation this potential difference creates a voltage drop of about 1.4 V within r_0 of the Paul trap.

Further the rods of the Paul trap are not perfectly aligned because the holding mechanisms of the trap electrodes have been partially removed during the upgrade to the second Paul trap iteration.

The third reason is described in [6]. Using the duty cycle to scan the a-

87

q-space also changes the form of the stability regions itself. This could be especially the reason for the measured hits outside of the boundary conditions on the rear end of Figure 5.9
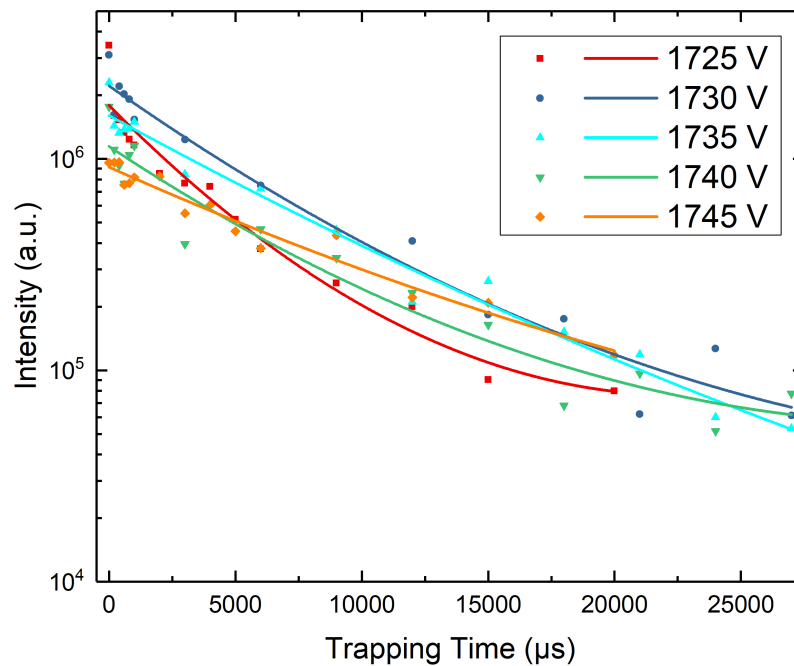
5.4.2 Trapping duration

Figure 5.10: This graph shows the trapping durations over various trap floating voltages. For the considered kinetic energy of $sim1740\,\mathrm{eV}$ 5 measurements have been performed. The Particles reach the trap with $\sim15\,\mathrm{eV}$ for 1725 V to $\sim$-5 eV for 1745 V which means that here where the particles should be deflected only the small part with a kinetic energy over 1745 eV can be found.

In Figure 5.10 one can see that the best trapping results are for a trap floating voltage of $\sim$1730 V to $\sim$1735 V. However the trapping here is still in the ms range. This is likely due to two reasons. At first the particles reach the Paul trap on the brink of r_0 so the potential drop in the Paul trap described above could move them even further to the outside, where they

Die approbierte gedruckte Originalversion dieser Dissertation ist an der TU Wien Bibliothek verfügbar.
The approved original version of this doctoral thesis is available in print at TU Wien Bibliothek.

TU Bibliothek
WIEN
Your knowledge hub

touch the electrodes.

Furthermore the Vacuum in the Paul trap chamber was under the 10^{-8} mBar range. So neutral gas particles have probably affected the anions in the Trap. At last the inaccurate Paul trap might heat particles over time and therefore eject them .
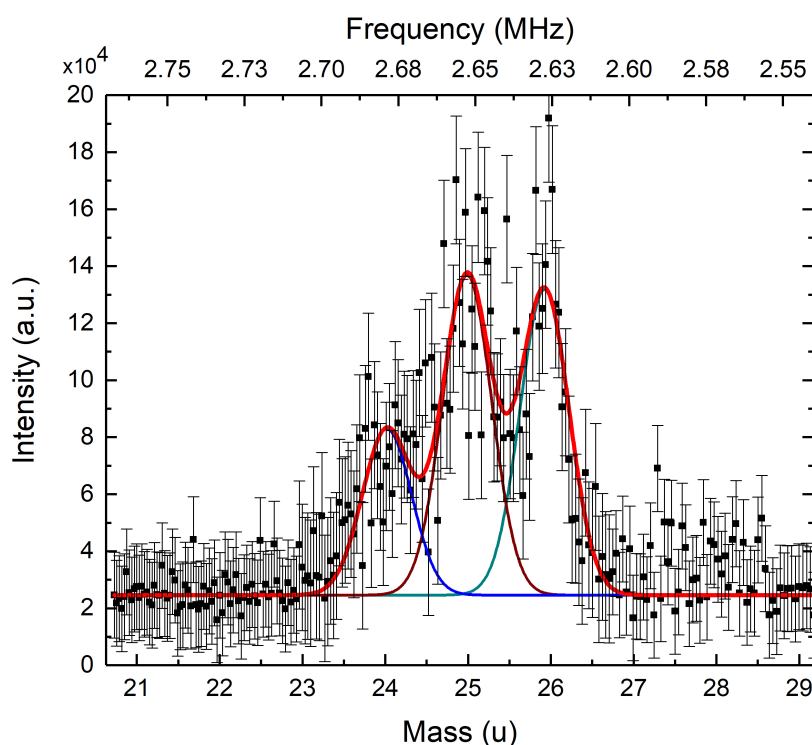
5.4.3   Mass spectrum in Paul trap

Figure 5.11: According to [4] the mass spectrum for the 3 anion species C_2^- ,C_2H^- and H_2CC^- with the masses 24, 25 and 26 was measured by setting the duty cycle d on $d = 0.6$ and then varying the frequency Ω. Each measurement consisted of a trapping duration of $200\,\mu s$ and for mass 23 to mass 27 each measurement point is the mean value of 60 measurements. Outside of this range each measurement point is the mean value of 20 measurements.

The Mass spectrum in the Paul trap was done to verify the results from [14] and to further test the Paul trap. The mass spectrum was taken with a duty cycle of 0.6 and the frequency range from $\Omega \sim 2.7\,\mathrm{MHz}$ to $\Omega \sim 2.55\,\mathrm{MHz}$

to scan the upper apex of Figure 5.8. The Mass scale was calculated from 5.1 as well.

$$a_x = -a_y = \frac{8Qd(V_1 + (1-d)V_2)}{m\Omega^2 r_0^2}, \quad q_x = -q_y = \frac{4Q2(V_1 - V_2)(1-d)d)}{m\Omega^2 r_0^2},$$
(5.2)

Knowing that only three masses are in the Paul trap one can either assume that the peak in the middle is Mass 25 and then see out of the calculation with the Frequency at the middle peak if the other masses are just one u away,

$$m = \frac{2.64^2}{\Omega^2} * 25 \ with \ \Omega_{m=25} \sim 2.64MHz$$
(5.3)

or one can take the measured a-parameter from the apex of Figure 5.9.

$$m = \frac{8Qd(V_1 + (1-d)V_2)}{a\Omega^2 r_0^2} \ with \ a \sim 0.21$$
(5.4)

The first way was more intuitive so it was used. One can see that the masses are slightly shifted towards lower frequencies. This is likely because of the distorted a-q-diagram, described above. The distance between the peaks however matches almost perfectly the expected mass differences of 1 u. A publication has been written as part of this thesis over the Borealis setup with focus on the Paul trap and its characterisation: [18]

5.4.4 Bunch form

Of great interest is also the bunch form that reaches the Paul trap. It is important to know what anion-species come first, or last and especially at which point is the highest amount of C_2^-. To look into this topic several measurements have been performed but unfortunately because of a lack of time it was not possible to finish said measurements to a satisfying degree. Because of this it is recommended to repeat the following measurements. Using this information, Figure 5.13 was created. In this Plot 4 mass spectra,
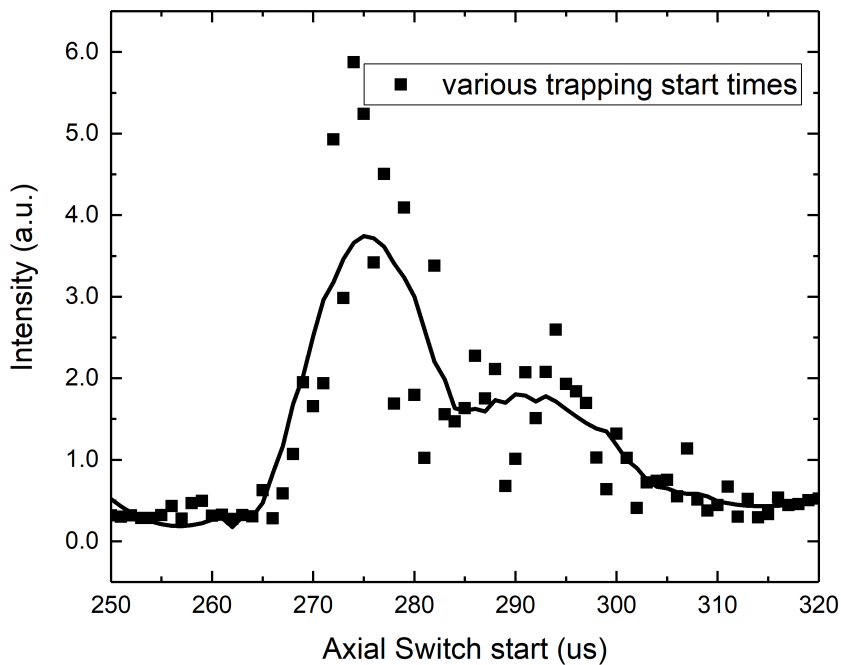

Figure 5.12: This Figure shows the measured intensity of the Bunch over different trap starting times. The Bunch is here $\sim 40\mu s$ long after the mass filter was used. One can see that the highest intensity is at a trap-start-time of around $273\,\mu s$ after the start of the Even-Lavie-valve 4.2 .

like in 5.11, were measured each at another trap starting point to measure the masses of different regions of the anion bunch. The focus here was laid on the highest peak at $273\,\mu s$ as it was done with 5.11. Despite the small amount of data points one can already see that C_2^- (2.69 MHz) seems to be present in the high peak of Figure 5.12 but not at the beginning of the peak
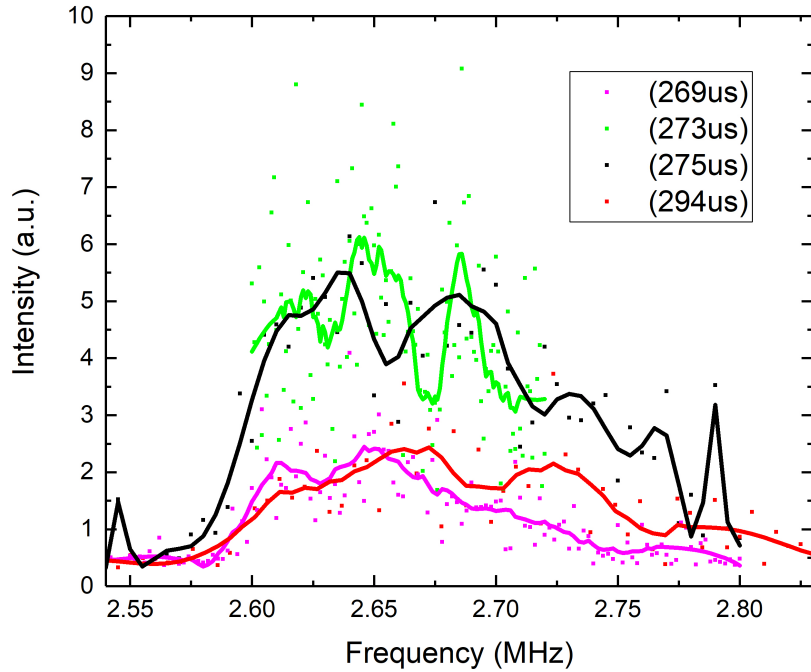
91

Figure 5.13: This graph shows 4 different Mass spectra measured like in 5.11. Each spectrum was measured at a different trap starting point from Figure 5.12. Like in 5.11 one can see at the $273\,\mu s$ plot that three masses are present. One has to be careful as in this graph the frequency scale goes from low to high.

at $269\,\mu s$. This is counter intuitive as one would expect the lighter mass 24 to arrive before the heavier masses 25 and 26. To investigate this more mass spectra at more starting points and with more measurement points should be created.

Chapter 6

Penning Trap

The Borealis experiment was originally founded to demonstrate laser cooling of C_2^- in a Penning trap [1], because in the future the laser cooling process shall be used in the Penning trap of the AEGIS experiment. Therefore, as part of this thesis a Penning trap was designed with multiple optical access points to provide the possibility for various types of laser cooling. The Magnetic field for the Penning trap would have been provided by a 1 T permanent magnet, build as a solenoid. The production of this magnet that should have a very small magnetic field gradient near its center, was done by the magnet department of CERN and is not part of this thesis. A superconducting solenoid was not possible to use due to cost reasons and the required infrastructure that was not available in the Borealis laboratory.

6.1 Borealis Penning trap

The Penning trap for Borealis should fulfill several requirements. First of all the electrode stack should be cooled by liquid nitrogen to enable a possible electron cooling before the laser cooling and to improve the vacuum in the Penning trap. The second requirement was to have 3 various laser access points including enhancement cavity mirrors. And at last the trap should contain an MCP to detect the anions trapped by it. To fulfill all these needs a trap design was constructed that was partially cryogenic. This was necessary because cryogenic electrodes were required to improve the trap vacuum while the mirrors for the laser access should not be cryogenic so they do not loose their enhancement ability when the cryogenic parts shrink. The electrodes are cooled by their electrical copper wires that are 3 mm thick to have a higher thermal conductivity. These wires are connected via barrel connectors to a CF 200 flange that uses 16 electrical connectors made from
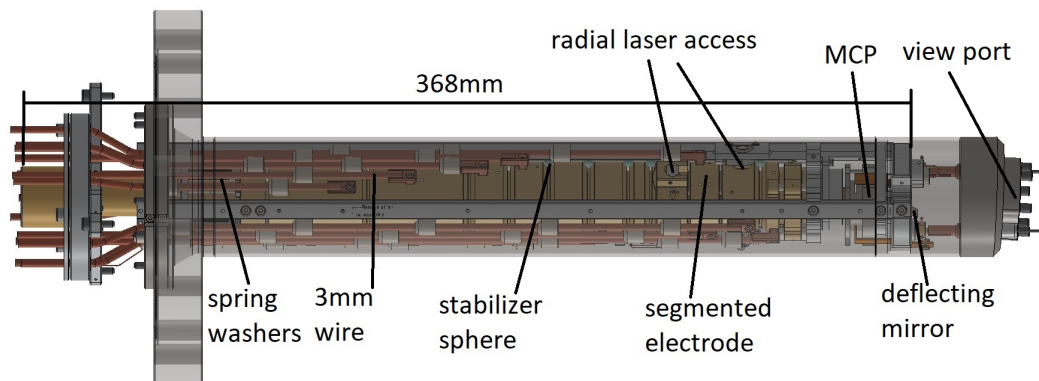
Figure 6.1: The Borealis Penning trap in its final design state. The trap has an overall length of 368mm and 3 laser access points into the trap stack in total. In this figure the 2 radial access points are visible. Multiple deflection mirrors are used to reach the access points from the optical view port on the right side of the picture. To stabilize the trap during the shrinking process caused by the liquid nitrogen cooling, spring washers press the trap together and stabilizer spheres should keep the electrodes in position.
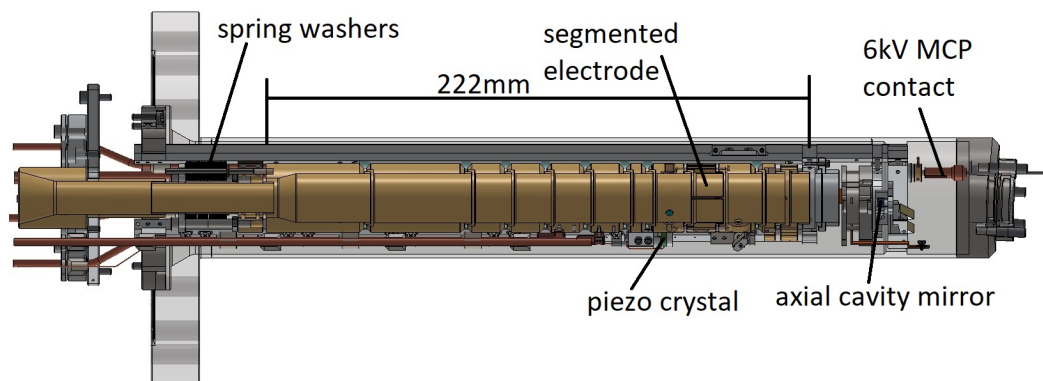

Figure 6.2: The trap stack that is under negative voltage is in total $222\,\mathrm{mm}$ long and contains one segmented electrode to have an option for plasma manipulation. The MCP that is visible here has a $6\,\mathrm{mm}$ hole in the center that is used for an axial laser access. As the plasma will be in the center of the Penning trap the MCP is mounted off axis so that the plasma will hit the MCP detector and not its hole. because of this the Laser does not go on the same axis as the trap stack through the trap but under an angle of 10.45^0.

$4\,\mathrm{mm}$ thick copper rods. These rods reach into a liquid nitrogen vessel made out of glas fibre ceramic (G10) where they are cooled. To reduce the icing the

area between the CF200 flange and the liquid nitrogen vessel is evacuated as well. COMSOL simulations that included thermal flow and thermal radiation
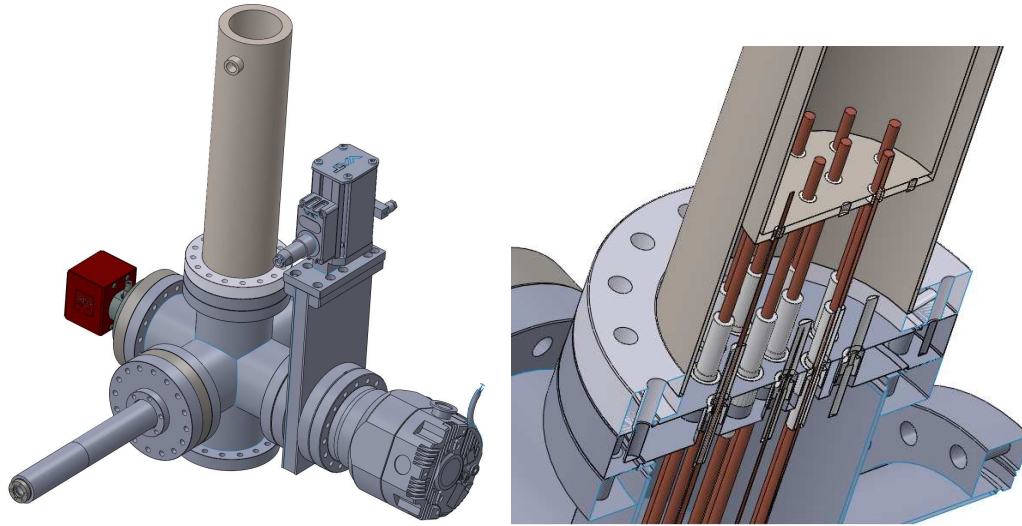

Figure 6.3:
left picture: The complete Penning trap chamber without the magnet. The Penning trap is in the lower left corner. On the lower right corner is a CF 200 Turbo pump and opposite of it a Getter-Ion-Pump. The large tower on top is an open vessel for liquid nitrogen that needs to be refilled every few hours. The rear side that is not visible here is for the connection to the Borealis setup.
right picture: The lower section of the cryogenic tower that is used to cool the copper connectors used in the feed through flange.

have shown that all electrodes should be able to reach temperatures under 100 K if the ends of the copper wires are in a cryogenic liquid nitrogen bath. According to the companie **Hositrad** it is possible to have cryogenic feed throughs without having vacuum issues in this configuration as long as the liquid nitrogen does not touch the ceramic- or steel- parts of the flange. A glue that can withstand cryogenic temperatures will be used to stick the copper connectors into the G-10 tower to seal it.

To have a trap stack that stays stable under the thermal contraction of almost 1 mm a shifting mechanism has been created. This mechanism consists of 30 Si_3N_4 spheres from **Sceram** that hold the electrodes between the long stack rods in figure 6.1. It was decided to use spheres as they provide a minimal contact surface between neighboring parts and so have less air enclosures and less thermal contact. However this stacking mechanism did not work out as expected and the electrodes were unstable, which would have caused shorts
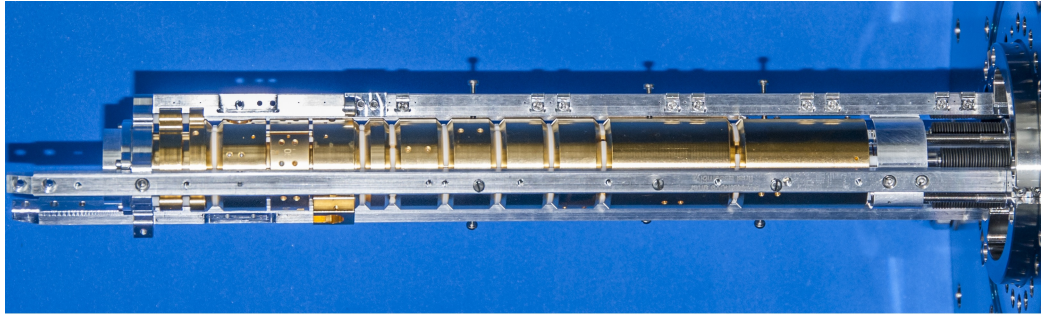
95

Figure 6.4: Picture of the finished Borealis Penning trap. The MCP, cables, optical devices and the front part are not mounted. The spheres have been exchanged to macor discs as they were problematic

and homogeneous fields. Because of this the spheres have been replaced with macor plates, seen in figure 6.4.

Because of the magnet the trap had to be closed and be under vacuum when the magnet is moved onto the Penning trap stack. Otherwise the fine corrections for the laser access could not be done properly. Because of this the laser access could only be done trough a small CF16 flange with an optical view port. This optical view port was used to create the laser access to all three cavities.
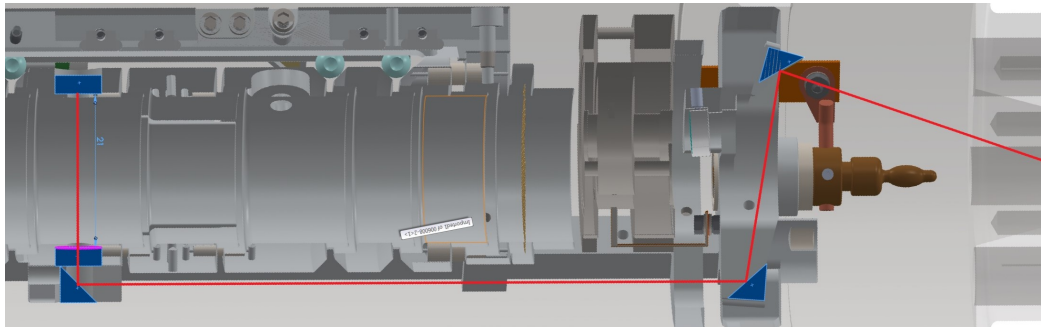

Figure 6.5: The deflection mirrors (Blue triangles) are used to bring the laser (red lines) from the CF16 viewport, on the right side of the picture, radially to the cavity in one of the electrodes (blue rectangles symbolize the 6 mm-diameter mirrors).

It was decided to use gold plated deflection mirrors with 5 mm side length, and ∼6 mm diameter mirrors that are reflective from one side and permeable from the other. Both were ordered from **thorlabs**.
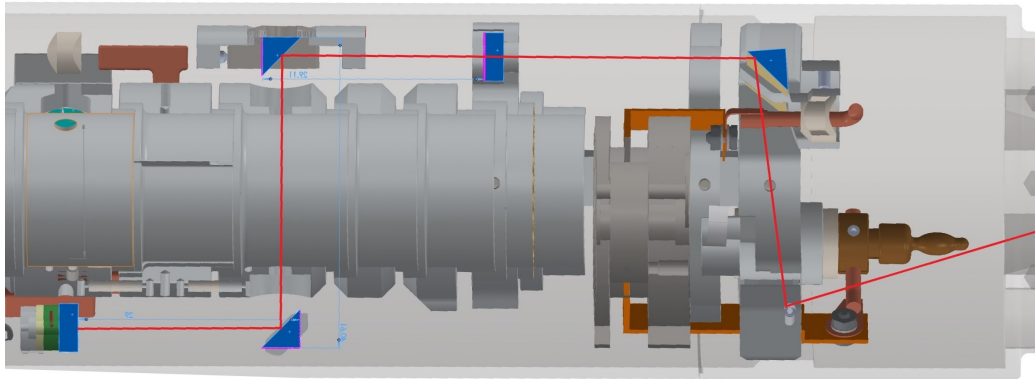
Figure 6.6: Like in figure 6.5 the laser access is radially, but here a longer cavity was required so the beam is deflected two times by 90^0 by a deflection mirror. This reduces the quality of the cavity but besides the longer beam path inside of it, it is possibility to use a piezo crystal to increase or decrease the length of the cavity by moving one of the 6 mm cavity mirrors, to create a standing wave.
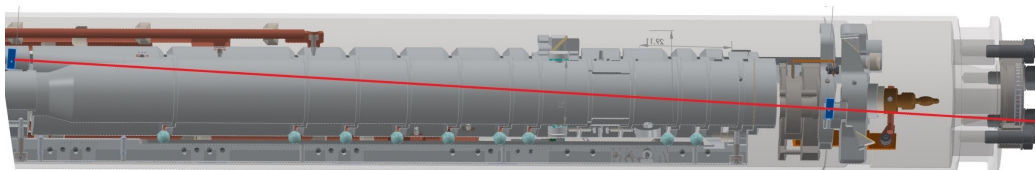

Figure 6.7: This figure shows the axial laser access. The cavity mirrors (blue rectangles) send the laser beam over the whole trap length. The MCP and the gold mesh between trap center and MCP have holes in the center for the laser beam.

6.2 Penning trap for transport of antiprotons

After several simulations of C_2^--laser cooling in Penning traps made by Julian Fesel in [14] it turned out that the Penning trap would have several problems for a first laser cooling attempt. First of all the ordered magnet would likely not reach the requirements needed for the Penning trap and it is still not manufactured to this date. Further the fact that the Penning trap does not separate masses means that eventual hot electrons could heat the C_2^- plasma and make laser cooling even more difficult. Because of this it was decided to use a Paul trap and modify the Penning trap to use it for another purpose: The A train project (Antiproton Transportation) that consists of the trapping of antiprotons directly from the AD in a portable trap. According to the magnet department the Solenoid would still be able to reach 0.84 T over

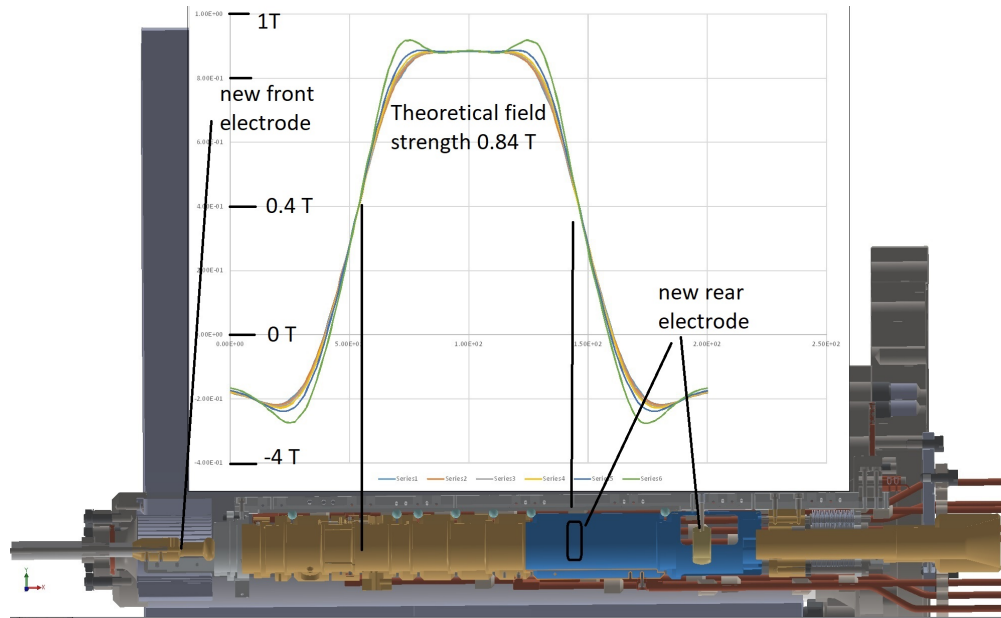a length distance of ~60 mm in its center. This would be sufficient to trap

Figure 6.8: The A Train Penning trap has no more laser access and no MCP. Therefore it has two additional electrodes that can be ramped up to 8 kV. The rear electrode is drawn on 2 positions. The inner position has to be manufactured in the future

antiprotons when their energy is low enough. The antiprotons from the AD however reach the trap with 5.3 MeV. To overcome this problem the AD outlet is covered by a 50 μm thick titanium foil that is used to decrease the energy of the particles. The same titanium foil will be used at the entrance of the Penning trap apparatus 6.3. Though most antiprotons will be lost on this way through titanium, 5 cm air, and again titanium foil, a small number of antiprotons in the >8 kV range should arrive in the Penning trap. The detection would simply be a detection of their annihilation products, when the Penning trap electrodes are turned off.

The modification in the penning trap consists of 2 additional electrodes. One electrode at the front section that is an electrical feedthrough on a CF 16 flange with a widening at the end, and a smaller electrode in the rear section. The new front electrode is capable of 10 kV and the rear electrode is capable of 8 kV without producing a short.

The special design of the magnet gives the magnetic field a turn at the end points. If the penning trap was mounted directly to the AD it would be necessary to upgrade the A Train version of the Penning trap and mount

the weaker rear electrode to the inner position shown in 6.8, to exclude the turning point of the magnetic field from the trapping area. If the A Train Penning trap would be connected to the Elena ring [3] it might be even possible to use it without the two additional electrodes as the other electrodes are still capable of voltage differences of up to 2.5 kV towards the holding rods. With these it would be easier to store the Antiprotons exactly in the 6 cm long center of the magnetic field and therefore reduce the antiproton loss at the ends of the penning trap.

Unfortunately both penning trap versions could not be used within this thesis because only the traps but not the magnet were finished by the workshop to this date.

Chapter 7

Conclusio and outlook

This thesis covers the ongoing efforts towards laser cooling of C_2^- for a sympathetic cooling of antiprotons, that are first described in [14] and are handled in chapter 2.0.3 and 2.0.3. Further, this thesis describes a part of the ongoing efforts of the gravity measurement of a pulsed antihydrogen beam in the Aegis experiment at CERN that is described in chapter 2.0.3. And at last this thesis covers the development of a transportable antiproton storage device.

After the construction of a source for C_2^- production, described in [14], the ongoing work of storing C_2^- is described in this thesis. During the design process of a Penning trap, the simulations shown in [14] have shown that laser cooling in a Penning trap has some unexpected difficulties and so for a proof of principle it was decided to use a digital linear Paul trap instead as this seemed to be easier for the beginning. The design, build and commissioning of said Paul trap and its pre-stages, that were part of this thesis are described in chapter four.

The experimental tests with all these devices have shown the behavior of said devices and their weaknesses described in 2.0.3. On this topic one can conclude that the deceleration stage causes a significant loss of anions when decelerating them to low kinetic energies. This is caused by inaccuracies of the machined parts, voltage ripples of the beam steering parts and the gold mesh, between the deceleration stage and the Paul trap. Further the deceleration stage injects the remaining anions into the outer radial area of the Paul trap which causes a further anion loss in the beginning of the trapping cycle as described in 2.0.3. Aside from this it was possible to measure a mass spectrum in the Paul trap that shows three different masses m24, m25, m26 as expected for C_2^-, C_2H^- and H_2CC^-, which proves that C_2^- is actually in the Paul trap. On this topic an article has been published [18]. With the completion of the Paul trap a big milestone for the Borealis experiment has

been reached and first attempts of evaporative cooling could start when the Laser setup is ready. Though it is suggested to further improve the Paul trap to increase the number of anions and the trapping duration. To do this the first steps would be to exchange the MCP that is used to measure the anions in the Paul trap as it is very likely partially damaged and detects only a small fraction of the anions that are actually in the trap. Further by doing this one can reduce the field gradients in the Paul trap to almost zero as the gold mesh between Paul trap and MCP can be set on other voltages than the entrance voltage of the MCP which is zero. In addition it is necessary to do a long heating to reduce the out gassing and so reduce the number of neutral particles that are in the Paul trap. Further it is necessary to remove all kapton insulated cables as they do not allow a vacuum that is better than 10^{-9} mBar according to their specifications. To get better trapping conditions the Mass spectrum measurement 5.13 should be finished in detail.

On the topic of the gravity measurement a superconducting shield has been simulated and a small version of it experimentally tested as described in [17]. The purpose of this shield is to create a field free zone where a gravity measurement can take place without the magnetic field influencing it via the Zeeman force. Further improvements of said shield are round edges to reduce the compressed fields on the edges that could rise over B_c1 and therefore bring the superconductor into a normal conducting or a Shubnikov phase [17]. For the Aegis apparatus a 2 m long and 20 cm diameter tube made of pure R.R.R(residual resistivity ratio)=300 [17] niobium would be sufficient in the area of the now mounted 1 T trap. But the tube that would hold a moiré deflectometer [11] could as well be mounted after the 1 T trap in a separate chamber if this would be required. This project was finished so here no outlook is necessary.

The last topic of this thesis includes the Penning trap, that is described in 2.0.3 and that was originally designed to work as a trap for C_2^- in the Borealis setup but is now redesigned to trap antiprotons from the AD or the ELENA ring. It is impossible to make an outlook here because the magnet for said Penning trap is still under construction and the trap itself has therefore not been tested yet.

In general one can say that The Borealis experiment is on track and all attempts can now focus on the work with the laser system, besides the new MCP for the Paul trap and the replacement of the kapton cables. On the antiproton storage project there is currently no work that could be done without knowing more about the system in operation. The superconducting shielding project has been finished and there is no further work that could be done, before the actual 2 m niobium tube for the AEGIS experiment is ordered.

Chapter 8

Curriculum vitae

Alexander Hinterberger
Brunellengasse 17, 1220 Wien
+068181615387, alexander.hinterberger@cern.ch
CV

<u>Personal Profile</u>

Name:	Alexander Hinterberger
Titel:	Dipl.-Ing. / Msc.
Nationality:	Austria
Date of Birth:	06.04.1987
Driving License:	Category B

<u>Professional Experience</u>

2016 - 2019   **CERN:** I worked on my PhD at the Aegis experiment: That included design, construction and commissioning of a digital rf-ion trap and microchannel plate detectors with phosphor screen readouts for trapping and laser-cooling of C_2^- anions.

During my time at CERN I gathered profound knowledge of the systems integrated in the Aegis apparatus, including Vacuum techniques, cryogenics, low- and high voltage systems, electronics, software, detectors and radioactive sources, as well as the safety procedures for these systems.

Another project I worked on was the calculation and measurement of magnetic fields with self-build hall sensors in superconducting tubes for a Moiré deflectometer in a cryogenic setup at the CERN cryogenics group.

2013   **Tel Aviv:** I attended an internship organized by the IAESTE organization at the University of Tel Aviv. The goal of the project was to create flow-models for tiny glass spheres in water and measure their movement by laser reflection.

<u>Education</u>

2016 - 2019   **CERN:**
PhD in applied physics.

2011 – 2015   **Technical University of Vienna:**
Master-Studies Physical Energy and Measurement Engineering

2007 – 2011   **Technical University of Vienna**
Bachelor-Studies Technical Physics

<u>Conference Presentations</u>

2017   Joint Annual Meeting of SPS and ÖPG, Geneva, *Shielding of magnetic field gradients*

<u>Publications</u>

2019   A. Hinterberger, S. Gerber, E. Oswald, C. Zimmer, J. Fesel, M. Doser, *Trapping of C2- in a digital ion trap*, Physical review B

2017   A. Hinterberger, S. Gerber, M. Doser, *Superconducting shielding with Pb and Nb tubes for momentum sensitive measurements of neutral antimatter*, JINST

<u>Scholarships</u>

Austrian doctoral student program at CERN

Alexander Hinterberger
Brunellengasse 17, 1220 Wien
+068181615387, alexander.hinterberger@cern.ch

Personal skills

Languages: German (first language), English (very good), French (basic)
Computer: MS Office, Origin, Latex, Comsol, Labview, Mathematica, Solidworks

Personal interests and hobbies:

Geopolitics, science (various fields), sport (volleyball, cycling, swimming), parlor games, books

Bibliography

[1] *Charged Particle Traps.* 2005.

[2] M. Amoretti, C. Amsler, G. Bonomi, A. Bouchta, P. Bowe, C. Carraro, C. L. Cesar, M. Chaliton, M. J.T. Collier, M. Doser, V. Filippini, F. S. Fine, A. Fontana, M. C. Fujiwara, R. Funakoshi, P. Genova, J. S. Hangst, R. S. Hayano, M. H. Holzscheiter, L. V. Jørgensen, V. Lagomarsino, R. Landua, D. Lindelöf, E. Lodi Rizzini, M. Macrì, N. Madsen, G. Manuzio, M. Marchesotti, P. Montagna, H. Pruys, C. Regenfus, P. Riedler, J. Rochet, A. Rotondi, G. Rouleau, G. Testera, A. Variola, T. L. Watson, and D. P. Van Der Werf. Production and detection of cold antihydrogen atoms. *Nature*, 2002.

[3] Wolfgang Bartmann, Pavel Belochitskii, Horst Breuker, Francois Butin, Christian Carli, Tommy Eriksson, Walter Oelert, Ranko Ostojic, and Sergio Pasinelli. The ELENA facility. In *Philosophical Transactions of the Royal Society A: Mathematical, Physical and Engineering Sciences*, volume 376, 2018.

[4] Alberto Berton, Pietro Traldi, Li Ding, and Francesco L. Brancia. Mapping the Stability Diagram of a Digital Ion Trap (DIT) Mass Spectrometer Varying the Duty Cycle of the Trapping Rectangular Waveform. *Journal of the American Society for Mass Spectrometry*, 2008.

[5] W. A. Bertsche. Prospects for comparison of matter and antimatter gravitation with ALPHA-g. In *Philosophical Transactions of the Royal Society A: Mathematical, Physical and Engineering Sciences*, 2018.

[6] Gregory F. Brabeck and Peter T A Reilly. Mapping ion stability in digitally driven ion traps and guides. *International Journal of Mass Spectrometry*, 2014.

[7] Laurent Canetti, Marco Drewes, and Mikhail Shaposhnikov. Matter and antimatter in the universe New Journal of Physics Matter and antimatter in the universe. *New Journal of Physics*, 2012.

[8] G. Cerchiari, P. Yzombard, and A. Kellerbauer. Laser-Assisted Evaporative Cooling of Anions. *Physical Review Letters*, 2019.

[9] Nabanita Deb, Laura L. Pollum, Alexander D. Smith, Matthias Keller, Christopher J. Rennick, Brianna R. Heazlewood, and Timothy P. Softley. Coulomb crystal mass spectrometry in a digital ion trap. *Physical Review A - Atomic, Molecular, and Optical Physics*, 2015.

[10] M. Doser, S. Aghion, C. Amsler, G. Bonomi, R. S. Brusa, M. Caccia, R. Caravita, F. Castelli, G. Cerchiari, D. Comparat, G. Consolati, A. Demetrio, L. Di Noto, C. Evans, M. Fanì, R. Ferragut, J. Fesel, A. Fontana, S. Gerber, M. Giammarchi, A. Gligorova, F. Guatieri, S. Haider, A. Hinterberger, H. Holmestad, A. Kellerbauer, O. Khalidova, D. Krasnický, V. Lagomarsino, P. Lansonneur, P. Lebrun, C. Malbrunot, S. Mariazzi, J. Marton, V. Matveev, Z. Mazzotta, S. R. Müller, G. Nebbia, P. Nedelec, M. Oberthaler, N. Pacifico, D. Pagano, L. Penasa, V. Petracek, F. Prelz, M. Prevedelli, B. Rienaecker, J. Robert, O. M. Røhne, A. Rotondi, H. Sandaker, R. Santoro, L. Smestad, F. Sorrentino, G. Testera, I. C. Tietje, E. Widmann, P. Yzombard, C. Zimmer, J. Zmeskal, and N. Zurlo. AEgIS at ELENA: Outlook for physics with a pulsed cold antihydrogen beam. *Philosophical Transactions of the Royal Society A: Mathematical, Physical and Engineering Sciences*, 2018.

[11] M. Doser, C. Amsler, A. Belov, G. Bonomi, P. Bräunig, J. Bremer, R. Brusa, G. Burkhart, L. Cabaret, C. Canali, F. Castelli, K. Chlouba, S. Cialdi, D. Comparat, G. Consolati, L. Di Noto, A. Donzella, A. Dudarev, T. Eisel, R. Ferragut, G. Ferrari, A. Fontana, P. Genova, M. Giammarchi, A. Gligorova, S. Gninenko, S. Haider, J. P. Hansen, S. Hogan, L. Jorgensen, T. Kaltenbacher, A. Kellerbauer, D. Krasnicky, V. Lagomarsino, S. Mariazzi, V. Matveev, F. Merkt, F. Moia, G. Nebbia, P. Nedelec, M. Oberthaler, D. Perini, V. Petracek, F. Prelz, M. Prevedelli, C. Regenfus, C. Riccardi, O. Rohne, A. Rotondi, M. Sacerdoti, H. Sandaker, M. Spacek, J. Storey, G. Testera, A. Tokareva, D. Trezzi, R. Vaccarone, F. Villa, Z. Zavatarelli, and A. Zenoni. Exploring the WEP with a pulsed cold beam of antihydrogen. *Classical and Quantum Gravity*, 2012.

[12] Lyndon Evans and Philip Bryant. LHC Machine. *Journal of Instrumentation*, 2008.

[13] U. Even. "The Even-Lavie valve as a source for high intensity supersonic beam". *EPJ Techniques and Instrumentation*, 2015.

[14] Julian Valentin Fesel. Molecular anions as a coolant for antimatter experiments. 2019.

[15] G. Gabrielse, N. S. Bowden, P. Oxley, A. Speck, C. H. Storry, J. N. Tan, M. Wessels, D. Grzonka, W. Oelert, G. Schepers, T. Sefzick, J. Walz, H. Pittner, T. W. Hänsch, and E. A. Hessels. Background-Free Observation of Cold Antihydrogen with Field-Ionization Analysis of Its States. *Physical Review Letters*, 2002.

[16] Nasa Goddard. Design of An Improved Miniature Ion Neutral Mass Spectrometer for NASA Applications. 1997.

[17] A. Hinterberger, S. Gerber, and M. Doser. Superconducting shielding with Pb and Nb tubes for momentum sensitive measurements of neutral antimatter. *Journal of Instrumentation*, 2017.

[18] Alexander Hinterberger, Sebastian Gerber, Emanuel Oswald, Christian Zimmer, Julian Fesel, and Michael Doser. Trapping of C2- in a digital ion trap. *Journal of Physics B: Atomic, Molecular and Optical Physics*, 2019.

[19] Alban Kellerbauer and Jochen Walz. A novel cooling scheme for antiprotons. *New Journal of Physics*, 2006.

[20] Niels Kjærgaard and Michael Drewsen. Crystalline beam emulations in a pulse-excited linear Paul trap. *Physics of Plasmas*, 2001.

[21] Raymond E. March and John F.J. Todd. *Practical aspects of trapped ion mass spectrometry: Volume IV: Theory and instrumentation.* 2010.

[22] W. Neuhauser, M. Hohenstatt, P. Toschek, and H. Dehmelt. Optical-sideband cooling of visible atom cloud confined in parabolic well. *Physical Review Letters*, 1978.

[23] Markus K. Oberthaler, Stefan Bernet, Ernst M. Rasel, Jörg Schmiedmayer, and Anton Zeilinger. Inertial sensing with classical atomic beams. *Physical Review A - Atomic, Molecular, and Optical Physics*, 1996.

[24] P. Pérez, D. Banerjee, F. Biraben, D. Brook-Roberge, M. Charlton, P. Cladé, P. Comini, P. Crivelli, O. Dalkarov, P. Debu, A. Douillet, G. Dufour, P. Dupré, S. Eriksson, P. Froelich, P. Grandemange, S. Guellati, R. Guérout, J. M. Heinrich, P. A. Hervieux, L. Hilico,

A. Husson, P. Indelicato, S. Jonsell, J. P. Karr, K. Khabarova, N. Kolachevsky, N. Kuroda, A. Lambrecht, A. M.M. Leite, L. Liszkay, D. Lunney, N. Madsen, G. Manfredi, B. Mansoulié, Y. Matsuda, A. Mohri, T. Mortensen, Y. Nagashima, V. Nesvizhevsky, F. Nez, C. Regenfus, J. M. Rey, J. M. Reymond, S. Reynaud, A. Rubbia, Y. Sacquin, F. Schmidt-Kaler, N. Sillitoe, M. Staszczak, C. I. Szabo-Foster, H. Torii, B. Vallage, M. Valdes, D. P. Van der Werf, A. Voronin, J. Walz, S. Wolf, S. Wronka, and Y. Yamazaki. The GBAR antimatter gravity experiment. *Hyperfine Interactions*, 2015.

[25] A. Speck, C. H. Storry, E. A. Hessels, and G. Gabrielse. Laser-controlled production of Rydberg positronium via charge exchange collisions. *Physics Letters, Section B: Nuclear, Elementary Particle and High-Energy Physics*, 2004.

[26] Pauline Yzombard, Mehdi Hamamda, Sebastian Gerber, Michael Doser, and Daniel Comparat. Laser cooling of molecular anions. *Physical Review Letters*, 2015.